Pion induced coherent strangeness production on light and medium-heavy nuclei

Dissertation
zur Erlangung des akademischen Grades
Doktor der Naturwissenschaften
der Justus–Liebig–Universität Gießen
Fachbereich 07 – Mathematik, Physik,
Geographie

vorgelegt von
Stefan Bender
aus Ilmenau

Gießen, 2009

D 26
Dekan: Prof. Dr. Bernd Baumann
1. Gutachter: Prof. Dr. Horst Lenske
2. Gutachter: Prof. Dr. Werner Scheid

Tag der mündlichen Prüfung: 22. 07. 2009

Contents

1 Introduction

Rutherford more or less purposefully discovered 1911 that atoms are not evenly distributed charge balls but consist of a very small positively charged core and an electron "shell" [1], carrying an equal negative charge. Physicists then got interested in a more detailed knowledge of both parts, the electron distribution in atoms and the inner structure of the nuclear core. Following work by Bohr [2–4] and Sommerfeld [5] dealt with the electrons and their orbits in atoms. And last but not least, the emergence of quantum mechanics helped to shed some light onto the, by then, mysteries of atomic physics. Nowadays we have a very accurate understanding of the electrons and their behaviour in atoms deduced mostly from electromagnetic scattering experiments. Our current models in terms of quantum mechanics and, in particular, quantum electrodynamics (QED) describe experiments to a very high precision.

However, it is still a challenge to give an accurate description of the inner core of an atom, the nucleus. This nucleus is, in contrast to the electrons of an atom, held together by additional interactions to the Coulomb force, since it seemed be an accumulation of positively charged particles which, as such, would repel each other. Furthermore, the relation between the charge and the mass of an atom was already determined for a number of elements and it was known that an element of charge Z has a mass number A which is approximately twice the charge number. It was postulated by Lord Ernest Rutherford that a neutral particle with the approximate mass of the proton is responsible for this charge/mass ratio of atoms. This *neutron* dubbed particle was discovered by Sir James Chadwick in 1932 [6] and completed the picture of the nucleus at that time. The nature of the *strong force* which holds the nucleus together, however, was still waiting for an explanation, qualitatively as well as quantitatively.

Already early models used the exchange of virtual particles, comparable to photon exchange in quantum electrodynamics, to describe the bonding force in nuclei [7–9]. In QED, the massless exchange particle, the photon, leads to an infinite range of the interaction. To describe the limited range of the nuclear force, these first models introduced massive exchange particles. On the other hand, they had to be light enough to fill the range between the nucleons. Based on this consideration, the mass range of these particles was determined to be different from any mass of the known particles at that time, namely electrons, and the nucleons themselves. Hence, they were named *mesons*, to indicate the "intermediate" nature of their mass. These exchange mesons were later experimentally found. However, not only them, but a whole zoo of new particles was detected and needed to be classified and understood. For example there were so-called "strange" particles

showing up in detectors of bubble chamber experiments on cosmic rays performed by Rochester and Butler in 1947 [10]. Those particles were unexpectedly slowly decaying reaction products, hence the name *strange*.

Classification attempts by Ne'emann [11], Gell-Mann [12, 13] and Zweig [14, 15] resulted in the so-called *quark model*. In this model, the strongly interacting particles, called *hadrons*, like the proton and neutron as the constituents of the atomic nucleus (which are called *baryons*) and the exchange mesons, have an additional intrinsic structure and their constituents are called *quarks*. The modern, quantum field theoretical, approach is called quantum chromodynamics (QCD) and describes these quarks as fractionally charged particles carrying an additional *colour* charge. Three of them can be combined in such a way that they form a colourless object namely the above mentioned baryons. Besides this description of the baryons, the mesons are bound states of a quark and an antiquark, which has the same mass as a quark but the opposite electric and colour charge. In this way both, baryons and mesons, are *colourless* objects.

The underlying principle of QCD is that of a non-abelian gauge theory, in contrast to the abelian theory of electrodynamics. The fundamental degrees of freedom are quarks and antiquarks and the force mediating particles are called *gluons*, which can also interact with themselves due to the non-abelian nature of the theory. Besides colour, the quarks have another degree of freedom, the so-called *flavour*. It was introduced first on the meson level, when the "strange" particles mentioned above were detected [10]. In terms of the quark model [11–15], these particles required the introduction of a new, heavier quark with a different flavour from that of the ones building up protons and neutrons. Today we know six quark flavours grouped into three families. Together with the three fermions, the three neutrinos, and the force mediating gauge bosons, they are part of the Standard Model. Since three of the quarks are very heavy compared to the rest, particle models are often reduced to the lightest ones which are the *up*, *down*, and *strange* quarks, or shortly u, d, and s, respectively.

Since quarks are fermions, and according to the spin-statistics-theorem, the wavefunctions must be antisymmetric with respect to the exchange of any two of them. This can be achieved, for example, by anti-symmetrising the colour part of the wavefunction and keeping it symmetric in all other parts such as flavour, spin, angular dependence, etc., either combined or separately. The above mentioned approaches to the strong force are based on group theoretical considerations and give the possibility of viewing these particles as representations of the underlying gauge group. This results in a systematic approach to the classification of the particle zoo. The convincing description of how these particles are made up, works even if the symmetry on which this model hinges is not an exact symmetry but an approximate one. This is the case of the flavour symmetry which would be exact, if all the quarks had the same mass.

In a more mathematical language, the quarks are given by the fundamental representation of SU(3), denoted in a group theoretical notation as **3** [16]. The anti-quarks are given by the complex conjugate representation which is denoted

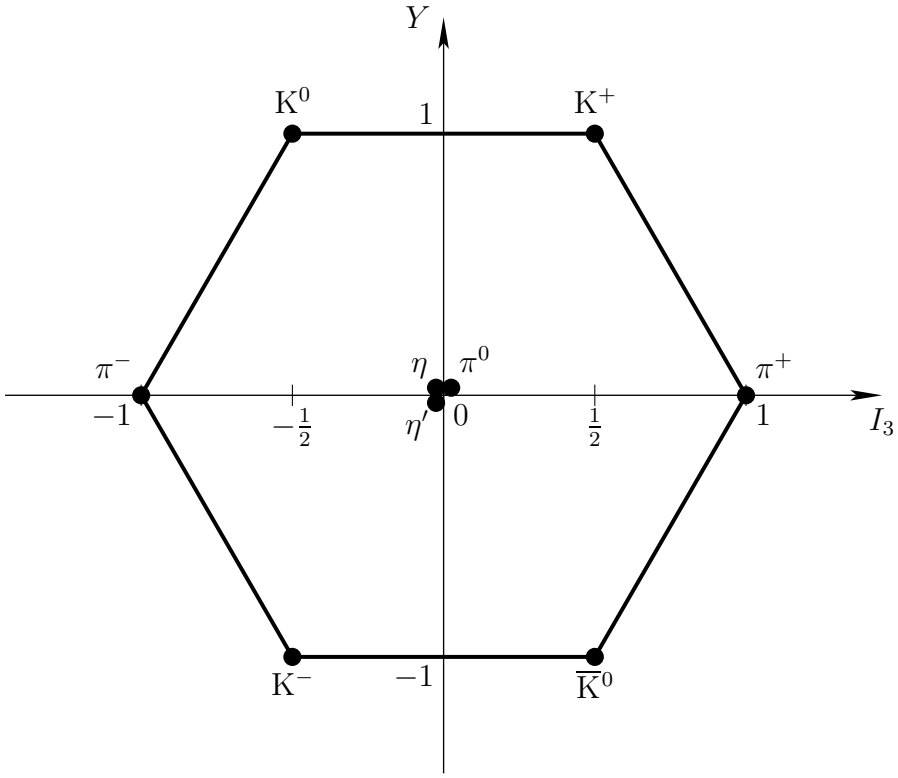

Figure 1.1: The particles of the meson octet as they depend on the third component of the isospin I_3 and the hypercharge Y.

by $\bar{\mathbf{3}}$. As mesons consist of a quark and an anti-quark, the respective states are given by the tensor product of the representations and the nine states can be decomposed as $\mathbf{3} \otimes \bar{\mathbf{3}} = \mathbf{8} \oplus \mathbf{1}$. The connection to the real particles is established by identifying the corners and the centre of the hexagon in figure 1.1 according to their experimentally found isospin, strangeness, and charge quantum numbers.

For the baryons this approach is a bit more complicated, since they consist of three quarks. The connection to real particles is established by taking into account not only the flavour SU(3), rather than, together with each quark's spin, the so-called spin-flavour SU(6). Decomposing these SU(6) multiplets into SU(3) multiplets according to the total spin of the quarks, one finds an octet of spin-1/2 baryons which can be identified with real particles according to figure 1.2.

In both diagrams, the particles are shown according to their third component of the isospin I_3 and their *strangeness* quantum number S. Together with the electric charge Q and baryon number B, this is combined into a new quantum number, the *hypercharge* Y, which is defined as $Y = S + B = 2(Q - I_3)$. The inclusion of particles with more than one strange quark leads to higher multiplets, as does the inclusion of particles containing the heavier quarks, the *charm*, *bottom*, or *top* quark, c, b, and t, respectively. Together, they extend the symmetry group further, but those details are beyond the scope of this introduction and we refer the interested reader to the literature, for example to [16, 17], for more details about

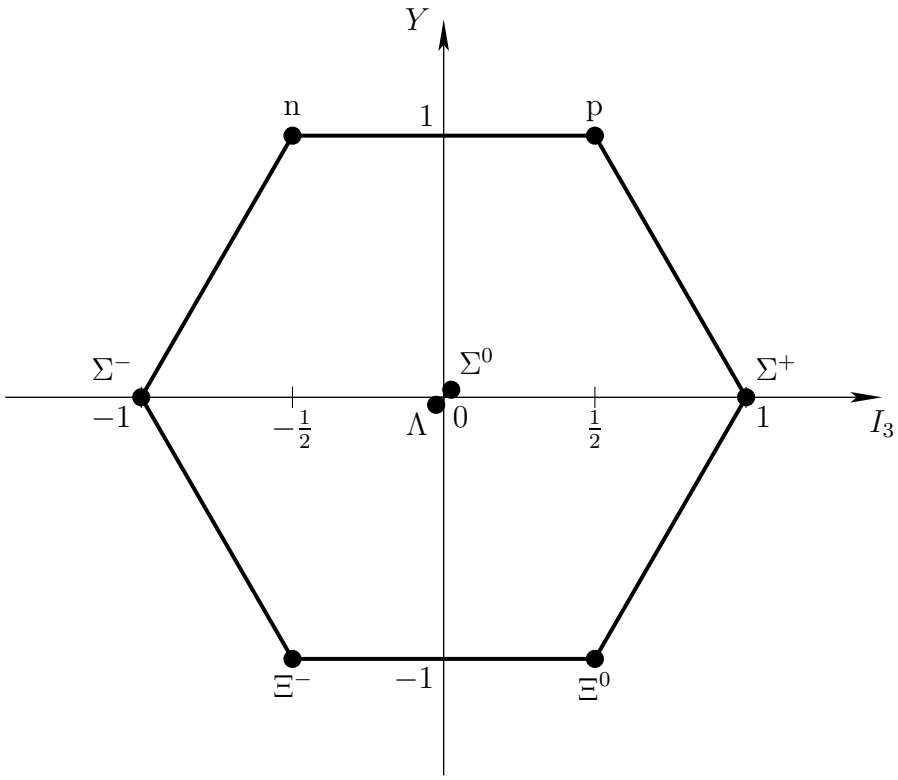

Figure 1.2: The particles of the baryon octet as they depend on the third component of the isospin I_3 and the hypercharge Y.

this group theoretical classification.

The degrees of freedom we have to take into account for the description of an interaction are determined by the available centre-of-mass energy. First descriptions of the interaction between nucleons in a nucleus go back to Yukawa and involved meson exchange via a Yukawa-potential [7]. Since the interaction energies are too low to probe the inner structure of the hadrons, this meson exchange model proved quite successful for the description of nuclei with respect to, for example, the binding energies or the charge form factors. We use some results of this approach in our calculations and for the energy range considered in this work, quarks are in fact not the relevant degrees of freedom. The quark picture is, however, important and helpful to understand the intrinsic properties of the particles involved in the interactions we consider.

In this thesis we investigate scattering processes between mesons and nuclei. In particular, we are interested in the production of baryons containing one strange quark in pion-nucleus reactions. There exist four such baryons, called *hyperons* and we can find them in figure 1.2, in particular they are the Σ^-, Σ^0, Σ^+, and the neutral Λ. They all lie on the axis $Y = 0$, since for these particles we have $S = -1$ for the strangeness content[1] and $B = 1$ for baryons. The Σ's form an isospin triplet

[1]This is $S = -1$ instead of $S = +1$ for historical reasons.

and the Λ an isospin singlet.

For our investigations, we assume that the incoming pion interacts with a bound nucleon and produces a pair of strange particles, a K-meson[2] and a Λ-baryon (see figure 1.2), of which the Λ is assumed to replace the struck nucleon forming a hypernucleus. Since the Λ carries the additional strangeness quantum number, it is not subject to the Pauli principle as all the other nucleons in the nucleus. It can, instead, occupy *any* orbit in the residual nucleus' potential. It is therefore an excellent probe for our understanding of the nucleonic potentials and the resulting bound states.

Therefore, we gain access to the spectroscopy of hypernuclei, which helps to understand the interaction between hyperons and nucleons in bound systems such as atomic nuclei. This topic is subject to active research since these interactions are also interesting for the understanding of neutron stars and their equation of state [18–23]. A schematic picture of the structure of a neutron star is shown in figure 1.3 [24, 25] and, as the big question mark indicates, the composition of the innermost core is still unknown. The presence of hyperons in neutron stars would change the degrees of freedom and therefore the equation of state which, in turn, is related to the so-called stiffness or softness [19]. It can therefore alter the maximum mass of neutron stars [26] and the search for such an upper bound on the mass of neutron stars in observational data could provide a clue on the number of the relevant degrees of freedom. So could, for example, the transition to a quark-gluon plasma in the innermost core lead to a further increase of the degrees of freedom and change the maximum mass as well to something different from that expected from pure hadronic matter [27–29]. The observation of neutron stars with the respective mass could then provide a verification of the existence of such a plasma independent from laboratory experiments [30, 31]. The understanding of these production processes at the small scale at the single nucleus level helps to extend current models to include the right fraction of each contributor to the equation of state.

Aside from the application to neutron stars and their equation of state, hypernuclei were produced in a variety of ways in the laboratory. The first discovery of a hypernucleus goes back to the observation of cosmic rays in emulsion chambers in 1952. A historical review of the physics of strange particles can be found, for example, in [32]. Later experiments with hypernuclei were performed at CERN and at the Brookhaven National Laboratory (BNL). Other experiments were performed in Japan at KEK and even more are planned for the future [33], for example at MAMI-C and PANDA-GSI [34].

Furhtermore, hypernulcei can be produced in secondary reactions in heavy-ion collisions [35–37]. In that processes, particles from the fireball from the primary interaction reach the—up to then—spectator core and produce strange particles, by the same process that we consider in this thesis. This process, induced by heavy-ion reactions, is subject to active research, theoretically for example within

[2]It is commonly called "kaon" for short. See figure 1.1 for the respective quantum numbers.

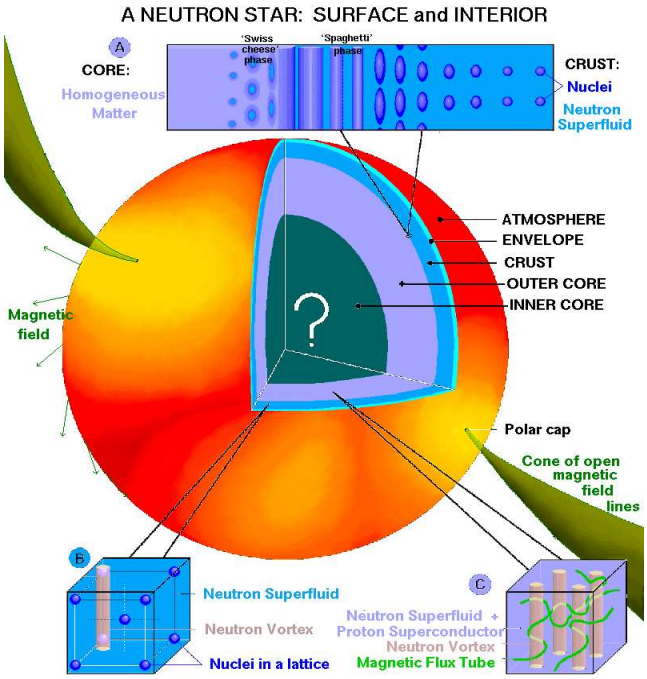

Figure 1.3: The structure of a neutron star to our current understanding [24, 25].

the semiclassical transport model approaches [38, 39], as well as experimentally by the HypHI collaboration [40]. Since the theoretical calculations thus far are either semiclassical [38, 39] or non-relativistic [41, 42], the work in this thesis will help to further improve the understanding of the underlying elementary process by being a fully relativistic quantum mechanical approach.

An extensive review on the production and decay of hypernuclei by Bandō et al. can be found in [43], where also different production mechanisms are discussed. The theoretical approaches to the experimental data deal with the production [44] or the polarisation of hypernuclei [41, 45] in (π^+, K^+) reactions. The experiments were mostly done in Japan at the KEK facility [42, 46–49]. A recent review on the available spectroscopic data using the various reactions can be found in [50].

The theoretical models used for the comparison with the data for example in [41, 42, 45] are successful in describing these data quite well. However, the nuclear model therein is not very sophisticated as it uses a non-relativistic Hamiltonian approach which is questionable. On the other hand, the mesons are treated within a so-called distorted wave model, that is, they are treated with their in-medium modifications taken into account and thus should be realistic. In this thesis, we try to combine the in-medium treatment of the mesons with a fully relativistic model of the nucleon and hyperon bound states.

We use an effective Lagrangian model which was already used to describe strangeness production in elementary reactions, for example in nucleon-nucleon scattering [51, 52], in proton-nucleus collisions [53, 54], and recently in photon induced

reactions [55]. We closely follow this approach and extend it to pion-nucleus reactions, in particular to (π^+, K^+) reactions on light (^{12}C) to medium-heavy (^{40}Ca) nuclei. Furthermore, we can use the experimental input to fit some of the parameters in these model calculations, which can then be used to predict the outcome of future experiments. Also, the experiments mentioned above provide us with spectroscopic data which helps to improve on the description of hypernuclei. Having access to these data enables us to calculate the differential cross sections in pion induced reactions with the model that is described in this work.

This thesis is organised as follows: Chapter 2 is devoted to the description of the nucleon and hyperon bound states used in our calculations. We give a brief overview of the general method before discussing the Fourier transform of the bound states needed for our calculations in momentum space. In chapter 3 we introduce our model for the elementary process of strangeness production via the excitation of nucleon resonances. We go into detail about the Lagrangians involved and how to calculate the scattering matrices in the case of pion-nucleus interactions. After discussing these ingredients for the calculations, we then give a short overview over general reaction theory in chapter 4, including relativistic kinematics and the calculation of differential cross sections.

Then, in chapter 5 we deal with the in-medium modifications which arise from the fact that the scattering happens inside a nucleus and not on a free nucleon. Unlike free particles, the mesons traverse some part of the nucleus before they interact which has to be dealt with. Elastic scattering, for example, leads to a change of the energy and momentum of the incoming pion as well as the outgoing kaon. We discuss the details of common approaches and present the approach we use. Since we are performing all the calculations in momentum space, we also lay down the details about the Fourier transformation and it's caveats.

Eventually, we present our results in chapter 6, wherein we start by presenting the results within the plane wave approximation, where the interactions of the meson with the (hyper)nucleus are neglected. We compare our calculation with experimental data on light nuclei such as ^{12}C. Within that approach, we can describe the experimental data for two different orbital transitions on this nucleus. Furthermore, we present our results for the pion induced process on ^{40}Ca on the example of one particular transition. However, there is yet no experimental data available that we could compare to. In chapter 7 we present the results of the extension of the model by taking the initial and final state interactions into account using the eikonal approximation.

2 Nuclear Theory

The aim of this thesis is to describe pion induced production of hypernuclei in coherent reactions. In particular, this reaction takes place inside the nucleus: the pion scatters on a nucleon which is bound inside the nucleus, the thereby produced Λ baryon ends up in a bound state and forms, together with the remaining nucleons, a hypernucleus. Therefore, we need a realistic description for these bound states. Fortunately, there are already many models and calculations as well as experimental data available. These models are of phenomenological [8, 9, 56] or microscopic nature [57–59]. Both are aimed at the description of the nuclear properties of a wide range of nuclei with a minimal set of parameters. In this chapter, we will give a short introduction of both concepts and discuss their relevance for describing pion induced strangeness production on nuclei.

2.1 General models

As noted above, there are basically two types of models available which deal with the description of the bound states inside a nucleus. On one hand there are the phenomenological models which are based on the work of Walecka and Serot [8, 9, 56], and which are also known as *quantum hadrodynamics* (QHD). Based on relativistic mean-field theories, these models include the interaction of nucleons based on σ-meson and ω-meson exchange, where the scalar meson (σ) is responsible for the long-range (attractive) part of the interaction and the vector meson (ω) creates the short-range (repulsive) part. With their empirically derived couplings, these models can be applied to infinite nuclear matter and charge symmetric nuclei [8, 9, 56]. Extensions of these models with additional mesons, for example including the ρ-meson, electromagnetic interactions, and meson self-interactions have been studied [60], as well as extensions to hypernuclei [61].

The success of these Walecka-type models lead to the question if these empirically adjusted couplings could be derived from first principles, that is from quantum chromodynamics (QCD), directly. This leads to microscopic approaches aiming at an *ab-initio* description of nuclei and hypernuclei by a consequent application of nuclear many-body theory. In particular, these are the "Dirac–Brueckner" (DB) or, more completely, "Dirac–Brueckner–Hartree–Fock" (DBHF) frameworks. Within these approaches, starting from a nucleon-nucleon (NN) interaction, an effective interaction is derived which describes the nuclear matter properties. The important advantage of those sophisticated models is, that they can describe a wide range of nuclear properties of a wide range of nuclei at the same time with only few

parameters. They can be further improved by including the density dependence of the couplings which leads to the density dependent relativistic hadron field theory (DDRH) [57–59]. We will go more into the details of this approach in the next section.

Since the full treatment of these microscopic models leads to involved calculations due to non-linearity and other complications, one still has to rely on approximations. Even ab-initio calculations at the hadronic level in nuclear medium are very involved. Therefore, here none of these rather involved calculations are performed, but we want to outline the problems and possibilities of these approaches in the following sections. For the present purpose, we use a purely phenomenological approach which, however, is justified by microscopic principles.

2.2 Dirac–Brueckner theory and extensions

In Dirac–Brueckner calculations, one takes a free NN-interaction and calculates from that the saturation properties of nuclear matter by solving the Bethe–Salpeter equation in the ladder approximation.

The starting point is a Lagrangian with baryon fields ψ and a number of scalar, pseudoscalar, and vector meson fields, decomposed into free parts and an interaction part: $\mathcal{L} = \mathcal{L}_\mathrm{B} + \mathcal{L}_\mathrm{M} + \mathcal{L}_\mathrm{int}$. We denote by $\mathcal{L}_\mathrm{B}$ and $\mathcal{L}_\mathrm{M}$ the usual Dirac and Klein–Gordon type Lagrangians for non-interacting baryons and mesons, respectively [62, 63],

$$\mathcal{L}_\mathrm{B} = \sum_b \bar{\psi}_b \left(\mathrm{i}\not{\partial} - m_b\right) \psi_b \;, \tag{2.1}$$

$$\mathcal{L}_\mathrm{M} = \frac{1}{2}\sum_m \left(\partial_\mu \phi_m \partial^\mu \phi_m - m_m^2 \phi_m^2\right) - \frac{1}{2}\sum_n \left[\frac{1}{2} F_{\mu\nu}^{(n)} F^{(n)\mu\nu} - m_n^2 V_\mu^{(n)} V^{(n)\mu}\right] . \tag{2.2}$$

In (2.1), ψ_b denotes the different baryon fields such as the nucleons (proton and neutron), their resonant excitations. And in (2.2), ϕ and the index m denote the scalar meson fields such as the π-, σ-, and δ-mesons. V_μ and the index n label the different vector meson fields, for example the ρ- and ω-meson. As usual, the vector meson field strength is given by $F_{\mu\nu} = \partial_\mu V_\nu - \partial_\nu V_\mu$.

The interaction Lagrangian $\mathcal{L}_\mathrm{int}$ is model dependent and can be used for the calculation of the bound state wave functions as well as for the explicit pion-nucleon interaction. In the scope of Dirac–Brueckner theory, a frequently used Lagrangian (see for example [64]) is

$$\begin{aligned}\mathcal{L}_\mathrm{int} = {} & g_\sigma \bar{\psi}\phi_\sigma\psi + g_\delta \bar{\psi}(\boldsymbol{\tau}\cdot\boldsymbol{\phi}_\delta)\psi - \mathrm{i}\frac{g_\pi}{2m}\bar{\psi}\gamma^5\gamma^\mu\partial_\mu(\boldsymbol{\tau}\cdot\boldsymbol{\phi}_\pi)\psi \\ & - \mathrm{i}\frac{g_\eta}{2m}\bar{\psi}\gamma^5\gamma^\mu\partial_\mu\phi_\eta\psi - g_\omega\bar{\psi}\gamma^\mu A_\mu^{(\omega)}\psi - \mathrm{i}\frac{f_\omega}{2m}\bar{\psi}\sigma^{\mu\nu}\partial_\mu A_\nu^{(\omega)}\psi \\ & - g_\rho\bar{\psi}\gamma^\mu(\boldsymbol{\tau}\cdot\boldsymbol{A}_\mu^{(\rho)})\psi - \mathrm{i}\frac{f_\rho}{2m}\bar{\psi}\sigma^{\mu\nu}\partial_\mu(\boldsymbol{\tau}\cdot\boldsymbol{A}_\nu^{(\rho)})\psi \;. \end{aligned} \tag{2.3}$$

In this form it contains the interaction of the nucleon with six mesons: π, ρ, σ, ω, η, and δ, representing the meson spectrum below 1 GeV. The long-range part is taken care of by the π-meson, whereas the heavier ρ- and ω-mesons are responsible for the short-range part. Table 2.1 shows a summary of the various mesons' properties from [17].

meson	I^G	J^{PC}	mass [MeV]
π^0	1^-	0^{-+}	134.98
$\pi^\pm$	1^-	$0^{-\pm}$	139.57
η	0^+	0^{-+}	547.85
ρ	1^+	1^{--}	775.49
ω	0^-	1^{--}	782.65
σ (f_0)	0^+	0^{++}	$(400 \ldots 1200)$
δ (a_0)	1^-	0^{++}	984.7

Table 2.1: Details of the various meson properties present in the NN-Lagrangian (2.3), data taken from [17].

The σ-meson has a large uncertainty in its mass which stems from the fact that it is observed as a broad resonance-like structure in $\pi\pi$-scattering. Here, however, only the t-channel is of importance which implies to integrate over the spectral functions of the mesons. For a more detailed discussion see [17] and the references therein.

The Lagrangian (2.3) has free parameters that need to be fixed, at least there are the meson masses and their respective coupling constants. As noted in [60], slightly different sets of parameters are used for actual calculations. Typically, the meson masses are fixed to the peak values of the corresponding spectral function (the values given in table 2.1). This leaves the meson-nucleon coupling parameters for fitting.

Once completely determined, the DB-Lagrangian can be used to model the relativistic NN-interaction in the nuclear medium, from which the self-energy is obtained that a nucleon acquires when moving through the nuclear medium. In a fully relativistic model, the self-energy has the Lorentz structure [64, 65]

$$\Sigma(k) = \Sigma^{\mathrm{s}}(k) - \gamma^0\Sigma^0(k) + \boldsymbol{\gamma}\cdot\boldsymbol{k}\,\Sigma^{\mathrm{v}}(k) \; .$$

By introducing effective masses and momenta,

$$\widetilde{m}(k) = m + \Sigma^{\mathrm{s}}(k) \; , \quad \widetilde{k}^0 = k^0 + \Sigma^0(k) \; , \quad \widetilde{\boldsymbol{k}} = \boldsymbol{k} + \boldsymbol{k}\,\Sigma^{\mathrm{v}}(k) \; ,$$

we can recover the usual form of the Dirac equation

$$(\widetilde{\not{k}} - \widetilde{m})\widetilde{\psi} = 0 \; .$$

Most of the nuclear models are simplified for actual calculations by using the mean-field approximation, which we introduce in the next section. Furthermore, we not only have to deal with nucleon-nucleon interactions, but also with nucleon-hyperon interactions to describe the bound states of the hypernucleus in the final state. Walecka-type models were successfully used for hypernuclear matter [61]. Within the scope of density-dependent relativistic hadron-dynamics, an application to hypernuclei was described in [59], where also a connection to experimental spectroscopic data is established.

2.3 Relativistic mean-field theory

The Dirac–Brueckner approach to the description of nuclear matter is feasible only for infinite nuclear matter and even then it is numerically very involved. Extending this approach to finite nuclei has not yet been done extensively and here the Walecka-type models are still the best way to describe a broad range of nuclear properties such as binding energies and spin-orbit splitting for a large number of nuclei. For finite nuclei, relativistic mean-field theory [9, 60] is still the model of choice and widely used.

For the treatment of finite nuclei, the local density approximation (LDA) [66] can be used, which includes the many-body correlations in effective two-body couplings rather than treating them explicitly. The modified QHD interaction Lagrangian reads [64]

$$\begin{aligned}\mathcal{L}_{\text{int}} = {}& \bar{\psi}\Gamma_\sigma(\hat{\varrho})\phi_\sigma\psi + \bar{\psi}\Gamma_\delta(\hat{\varrho})(\boldsymbol{\tau}\cdot\boldsymbol{\phi}_\delta)\psi - \bar{\psi}\Gamma_\omega(\hat{\varrho})\gamma^\mu A_\mu^{(\omega)}\psi \\ & - \bar{\psi}\Gamma_\rho(\hat{\varrho})\gamma^\mu(\boldsymbol{\tau}\cdot\boldsymbol{A}_\mu^{(\rho)})\psi - e\bar{\psi}Q\gamma^\mu A_\mu^{(\gamma)}\psi \ .\end{aligned}$$

This way, the coupling constants g were replaced by the density-dependent quantities $\Gamma(\hat{\varrho})$ [57, 58]. These vertex functionals are constrained to be Lorentz-scalars as well as scalars in spin, isospin, and flavour space. They depend on the density operator $\hat{\varrho}$ which, in turn, depends on the baryon fields itself: $\hat{\varrho} = \hat{\varrho}(\bar{\psi}, \psi)$ [57, 58]. This modifies the equations of motions for all the involved fields, giving in-medium corrections to the vertices. The resulting equations of motion for the meson fields [57, 59] read

$$(\Box + m_\sigma^2)\phi_\sigma = \Gamma_\sigma(\hat{\varrho})\bar{\psi}\psi \ , \tag{2.4a}$$

$$(\Box + m_\delta^2)\boldsymbol{\phi}_\delta = \Gamma_\delta(\hat{\varrho})\bar{\psi}\boldsymbol{\tau}\psi \ , \tag{2.4b}$$

$$\partial_\nu F^{(\omega)\mu\nu} + m_\omega^2 A^{(\omega)\mu} = \Gamma_\omega(\hat{\varrho})\bar{\psi}\gamma^\mu\psi \ , \tag{2.4c}$$

$$\partial_\nu \boldsymbol{F}^{(\rho)\mu\nu} + m_\rho^2 \boldsymbol{A}^{(\rho)\mu} = \Gamma_\rho(\hat{\varrho})\bar{\psi}\boldsymbol{\tau}\gamma^\mu\psi \ , \tag{2.4d}$$

$$\partial_\nu F^{(\gamma)\mu\nu} = e\bar{\psi}Q\gamma^\mu\psi \ . \tag{2.4e}$$

They have the standard structure except for the important difference of the field-theoretical vertex functionals which account for the resummation of the baryon-baryon interactions via the density operator $\hat{\varrho}$. Applying the chain rule to the

Euler–Lagrange equation of the baryon spinor wave functions ψ and $\bar{\psi}$, we get an additional term

$$\frac{\delta \mathcal{L}_{\text{int}}}{\delta \bar{\psi}} = \frac{\partial \mathcal{L}_{\text{int}}}{\partial \bar{\psi}} + \frac{\partial \mathcal{L}_{\text{int}}}{\partial \hat{\varrho}} \frac{\delta \hat{\varrho}}{\delta \bar{\psi}} ,$$

where δ denotes the functional derivative, since $\mathcal{L}_{\text{int}}$ is a functional of the density operator via the vertex functional $\Gamma(\hat{\varrho})$. The density-dependence of these self-energies leads to the additional so-called re-arrangement terms [58, 59, 64]:

$$\Sigma^{\text{s}} = \Sigma^{\text{s}(0)} + \Sigma^{\text{s}(r)} , \quad \Sigma^{\mu} = \Sigma^{(0)\mu} + \Sigma^{(r)\mu} .$$

They enter the equations of motion for the nucleons, which is given by a modified Dirac equation

$$\left[\gamma_{\mu} \left(\mathrm{i}\partial^{\mu} - \Sigma^{\mu}\right) - \left(m - \Sigma^{\text{s}}\right)\right] \psi = 0 . \tag{2.5}$$

Furthermore, one distinguishes between vector density dependence (VDD) and scalar density dependence (SDD) [64]. In the first case, all mesons contribute to the vector re-arrangement term, such that

$$\begin{aligned}
\Sigma^{\text{s}(r)} &= 0 , \\
\Sigma^{(r)\mu} &= \left(\frac{\partial \Gamma_{\omega}}{\partial \hat{\varrho}} \bar{\psi} \gamma^{\nu} A^{(\omega)}_{\nu} \psi + \frac{\partial \Gamma_{\rho}}{\partial \hat{\varrho}} \bar{\psi} \gamma^{\nu} (\boldsymbol{\tau} \cdot \boldsymbol{A}^{(\rho)}_{\nu}) \psi \right. \\
&\qquad \left. - \frac{\partial \Gamma_{\sigma}}{\partial \hat{\varrho}} \bar{\psi} \phi_{\sigma} \psi - \frac{\partial \Gamma_{\delta}}{\partial \hat{\varrho}} \bar{\psi} (\boldsymbol{\tau} \cdot \boldsymbol{\phi}_{\delta}) \psi \right) u^{\mu} ,
\end{aligned}$$

where u^{μ} is the four-velocity. In the case of scalar density dependence, the (pseudo)-scalar mesons contribute to the scalar re-arrangement term via their vertex functionals Γ_{σ} and Γ_{δ}. The (pseudo)vector mesons contribute to the vector re-arrangement term, and the self-energy modifications are then given by

$$\begin{aligned}
\Sigma^{\text{s}(r)} &= \frac{\partial \Gamma_{\sigma}}{\partial \hat{\varrho}} \bar{\psi} \phi_{\sigma} \psi - \frac{\partial \Gamma_{\delta}}{\partial \hat{\varrho}} \bar{\psi} (\boldsymbol{\tau} \cdot \boldsymbol{\phi}_{\delta}) \psi , \\
\Sigma^{(r)\mu} &= \left(\frac{\partial \Gamma_{\omega}}{\partial \hat{\varrho}} \bar{\psi} \gamma^{\nu} A^{(\omega)}_{\nu} \psi + \frac{\partial \Gamma_{\rho}}{\partial \hat{\varrho}} \bar{\psi} \gamma^{\nu} (\boldsymbol{\tau} \cdot \boldsymbol{A}^{(\rho)}_{\nu}) \psi \right) u^{\mu} .
\end{aligned}$$

The equations of motions (2.4) and (2.5) are highly non-linear. A self-consistent solution for the wave-functions is impossible, since the source terms and the baryon self-energies depend on the baryon operators. In the mean-field or Hartree approximation, this problem is circumvented by substituting the fields by their expectation values

$$\begin{aligned}
\phi_{\sigma} &\mapsto \langle \phi_{\sigma} \rangle , \\
\boldsymbol{\phi}_{\delta} &\mapsto \langle \boldsymbol{\phi}_{\delta} \rangle \, \delta_{i3} , \\
A^{(\omega)}_{\mu} &\mapsto \langle A^{(\omega)}_{\mu} \rangle \, \delta_{\mu 0} , \\
\boldsymbol{A}^{(\rho)}_{\mu} &\mapsto \langle \boldsymbol{A}^{(\rho)}_{\mu} \rangle \, \delta_{i3} \delta_{\mu 0} .
\end{aligned}$$

The baryon bilinear expressions in the equations of motion (2.4) are substituted by the densities as

$$\bar{\psi}\psi \mapsto \langle\bar{\psi}\psi\rangle = \varrho^{\mathrm{s}} \,, \tag{2.6a}$$
$$\bar{\psi}\tau_i\psi \mapsto \langle\bar{\psi}\tau_i\psi\rangle\,\delta_{i3} = \langle\bar{\psi}\tau_3\psi\rangle = \varrho^{\mathrm{s}}_3 \,, \tag{2.6b}$$
$$\bar{\psi}\gamma^\mu\psi \mapsto \langle\bar{\psi}\gamma^\mu\psi\rangle\,\delta_{\mu0} = \langle\bar{\psi}\gamma^0\psi\rangle = \varrho \,, \tag{2.6c}$$
$$\bar{\psi}\tau_i\gamma^\mu\psi \mapsto \langle\bar{\psi}\tau_i\gamma^\mu\psi\rangle\,\delta_{i3}\delta_{\mu0} = \langle\bar{\psi}\tau_3\gamma^0\psi\rangle = \varrho_3 \,. \tag{2.6d}$$

Note that in (2.6), ψ denotes the nucleon isospin doublet containing both the proton and the neutron

$$\psi = \begin{pmatrix}\psi_{\mathrm{p}}\\ \psi_{\mathrm{n}}\end{pmatrix} \,.$$

The densities in (2.6) can therefore be expressed in terms of the proton and neutron densities, ϱ_{p} and ϱ_{n} respectively, as follows:

$$\varrho^{\mathrm{s}} = \varrho^{\mathrm{s}}_{\mathrm{n}} + \varrho^{\mathrm{s}}_{\mathrm{p}} \,, \qquad \varrho^{\mathrm{s}}_3 = \varrho^{\mathrm{s}}_{\mathrm{n}} - \varrho^{\mathrm{s}}_{\mathrm{p}} \,,$$
$$\varrho = \varrho_{\mathrm{n}} + \varrho_{\mathrm{p}} \,, \qquad \varrho_3 = \varrho_{\mathrm{n}} - \varrho_{\mathrm{p}} \,.$$

2.4 Nucleon wave functions

Once the origin and structure of the self-energies is understood we may introduce approximations simplifying the numerical calculations. For our purpose, we use an empirical approach to describe the effective self-energies in terms of single-particle scalar and vector potentials. The substitution looks like

$$\Sigma^\mu \mapsto V^\mu \,, \qquad \Sigma^{\mathrm{s}} \mapsto -V_{\mathrm{s}} \,,$$

where the vector potential can be taken to be time-like only, $V^\mu = (V_{\mathrm{v}}, \mathbf{0})$ for spherically symmetric nuclei [8]. The Dirac equation (2.5) then reads

$$\left(\mathrm{i}\partial\!\!\!/ - m - \gamma^0 V_{\mathrm{v}} - V_{\mathrm{s}}\right)\psi = 0 \,. \tag{2.7}$$

Rather than deriving the self-energies, and hence the potentials in (2.7), self-consistently, we use, as a realistic approximation, a Woods–Saxon parametrisation for the nuclear short-range potentials V_{v} and V_{s}

$$V_\alpha(r) = \frac{V_{0\alpha}}{1 + \exp\{\frac{r_\alpha - R_\alpha}{a_\alpha}\}} \,. \tag{2.8}$$

Furthermore, the Coulomb potential is included for the protons. In (2.8), $V_{0\alpha}$, R_α, and a_α are adjustable parameters and the Greek letter $\alpha \in \{\mathrm{s}, \mathrm{v}\}$ labels the scalar and vector potential, respectively. The radial parameters R_α are further parametrised according to $R_\alpha = r_{0\alpha}A^{1/3}$. The free parameters are extracted from

experimental data for the charge radius, the nucleon separation energy, and the first diffraction minimum of the charge form factor. This procedure was discussed in detail in [67] and the fit parameters and the resulting potential parameters for ^{12}C and ^{40}Ca are shown in tables 2.2 and 2.3. The resulting charge form factor of ^{12}C is compared to experimental data from [68] in figure 2.1.

nucleus	orbital	separation energy [MeV] proton exp.	proton theory	neutron exp.	neutron theory	charge radius [fm] exp.	charge radius [fm] theory
^{12}C	$1p_{3/2}$	15.957	15.653	18.722	18.562	2.472	2.470
^{40}Ca	$1d_{3/2}$	8.328	8.265	15.641	15.797	3.450	3.465

Table 2.2: Nuclear variables used to fit the potential parameters for ^{12}C and ^{40}Ca in comparison to experimental data. Values taken from [67, 69].

nucleus	V_v [MeV]	$r_{0\mathrm{v}}$ [fm]	a_v [fm]	V_s [MeV]	$r_{0\mathrm{s}}$ [fm]	a_s [fm]
^{12}C	385.7	1.056	0.427	−470.4	1.056	0.447
^{40}Ca	348.1	1.149	0.476	−424.5	1.149	0.506

Table 2.3: Potential parameters for the vector and scalar potentials from the fit to the experimental values from table 2.2.

The differential equation (2.7) is solved with the ansatz

$$\psi(\boldsymbol{x}) = \begin{pmatrix} f_{n,j}(r)\, \mathcal{Y}_{\ell s}^{j m_j}(\hat{x}) \\ -\mathrm{i} g_{n,j}(r)\, \mathcal{Y}_{\ell' s}^{j m_j}(\hat{x}) \end{pmatrix} . \tag{2.9}$$

The spin-spherical harmonics $\mathcal{Y}_{\ell s}^{j m_j}$ are given by [70]

$$\mathcal{Y}_{\ell s}^{j m_j}(\hat{x}) = \sum_{m_\ell, m_s} \langle \ell, m_\ell, s, m_s \,|\, j, m_j \rangle\, Y_{\ell m_\ell}(\hat{x}) \chi_{s,m_s} , \tag{2.10}$$

where χ is the usual two-dimensional Pauli-spinor and $Y_{\ell m}$ are the spherical harmonics of the first kind, $\ell' = 2j - \ell$, and $m_\ell + m_s \stackrel{!}{=} m_j$. $\hat{x}$ denotes the angular variables θ and ϕ of the three-vector $\boldsymbol{x}$. The Dirac conjugate spinor is, as usual, given by $\bar{\psi} = \psi^\dagger \gamma^0$.

Using the ansatz (2.9) for (2.7), one can eliminate the lower components and arrives at a differential equation for the upper component $f(r)$. We go into more details about this equation and their solution in appendix D. We present some explicit results for these radial functions for ^{12}C below, and for the hypernucleus $^{12}_{\Lambda}$C in the next section.

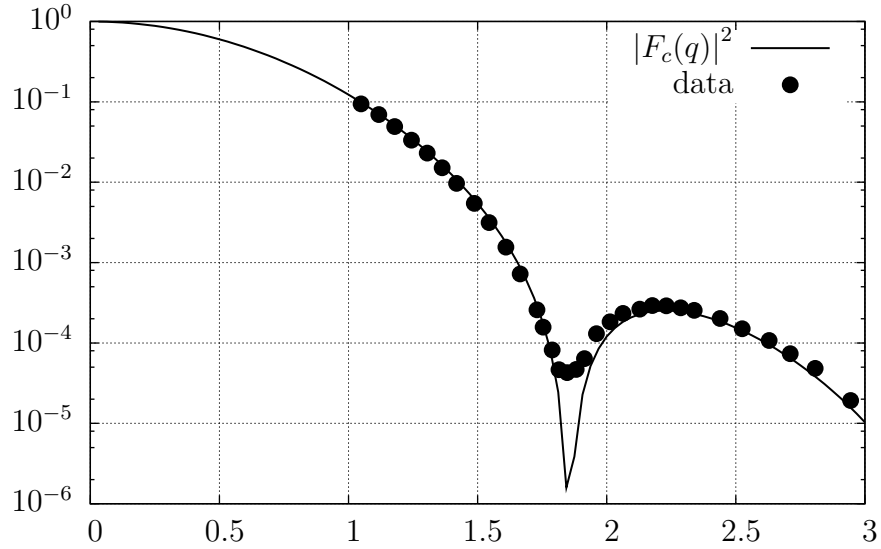

Figure 2.1: The charge form factor of ^{12}C compared to experimental data from [68].

The densities are given by the absolute magnitude of the radial functions f and g by

$$\varrho = \frac{1}{4\pi}\sum_\alpha (2j_\alpha + 1)\left(|f_\alpha|^2 + |g_\alpha|^2\right) , \tag{2.11}$$
$$\varrho_s = \frac{1}{4\pi}\sum_\alpha (2j_\alpha + 1)\left(|f_\alpha|^2 - |g_\alpha|^2\right) ,$$

where ϱ denotes the usual (vector) density and ϱ_s is the scalar density. The label α combines all the quantum numbers of the respective wave function, such as n, j (as used in (2.9)) and possibly others. These densities are calculated for both the neutrons and the protons, and for ^{12}C the vector densities are shown in figure 2.2. In contrast to ^{12}C, ^{40}Ca is a heavier, and thus larger, nucleus. This can clearly be seen in figure 2.3, where the respective neutron and proton densities are shown. They reach out much further than in the Carbon case and also the inner structure changes. The differences between the neutron and proton densities in both cases are due to the Coulomb repulsion.

For the description of the initial and final state interactions of mesons (see also chapter 5), it is useful to parametrise these densities. Common parametrisations include a modified Gaussian form or a Woods–Saxon form. With a fit to the calculated densities from the bound states above, we can determine the parameters. These fit parameters and how they compare to the densities calculated from the solution of the Dirac equation (2.5) are discussed in more detail in section 5.4, where we use them especially for the eikonal approximation.

Next we turn to the radial parts of the wave functions itself. Our coherent model

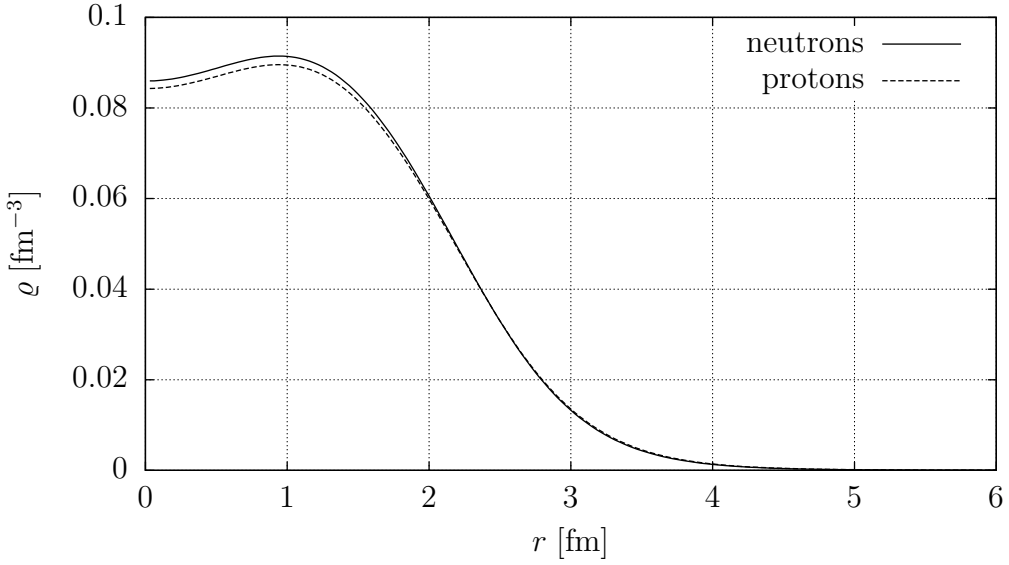

Figure 2.2: The neutron and proton density profiles of ^{12}C as calculated from the radial parts of the wave function. The slight difference stems from the Coulomb repulsion of the protons.

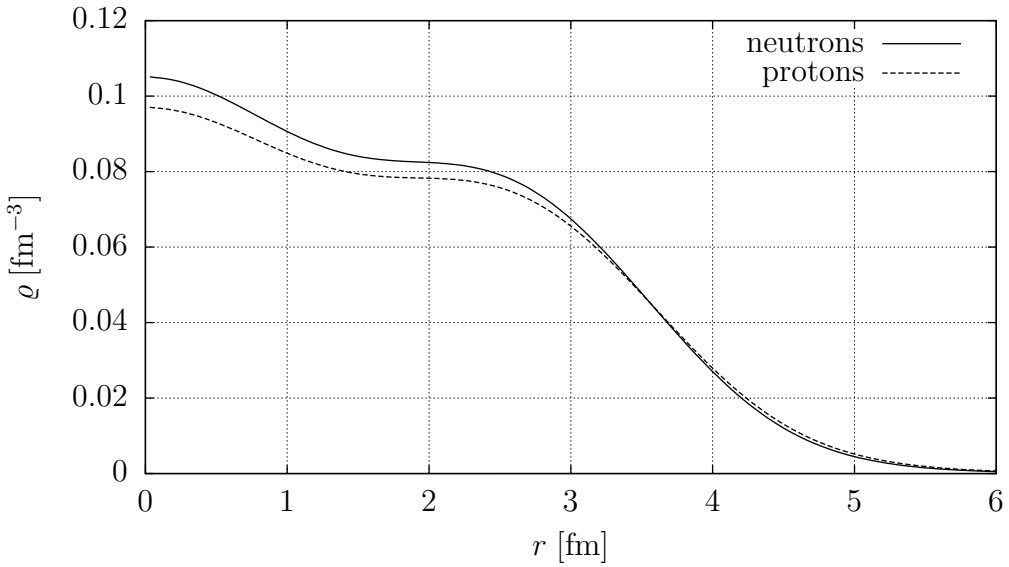

Figure 2.3: The neutron and proton density profiles of ^{40}Ca as calculated from the radial parts of the wave function. Here, again, the difference is due to the Coulomb repulsion between the protons.

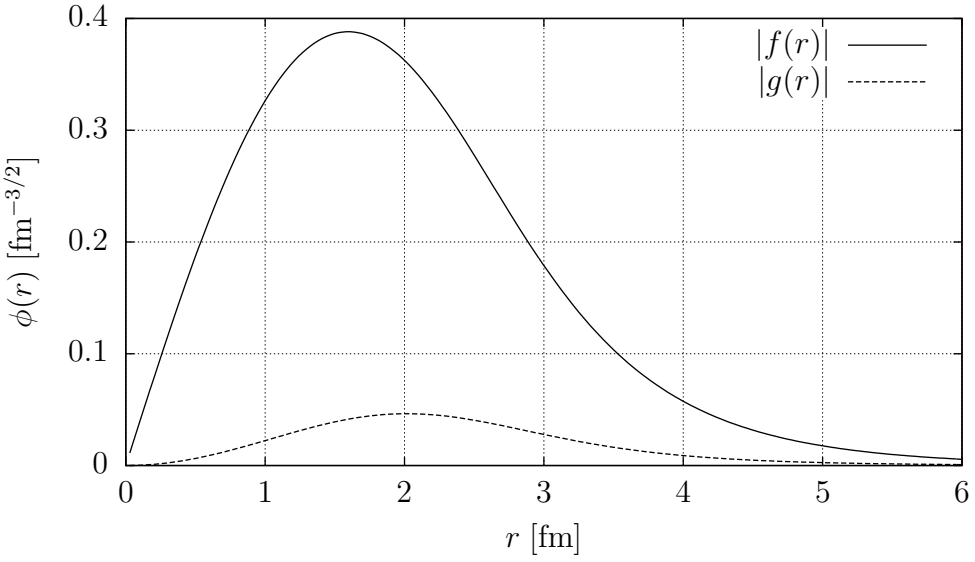

Figure 2.4: The $p_{3/2}$ orbital of ^{12}C in coordinate space, the magnitude of the upper and lower components, f (solid line) and g (dashed line), respectively, as a function of the radial distance r.

requires that the nucleus remains in its ground state, and since the struck nucleon is "transformed" into a hyperon, we have to look at the least bound nucleon. If the process takes place at a nucleon in a different orbit, the resulting hypernucleus ends up in an excited state. It would then be detectable by an additional photon from the transition to the non-excited ground state. This additional photon, however, is not yet measured in the experiments, so that we assume that the nucleus and the remaining nuclear core in the hypernucleus, that is, the core without the struck nucleon, are in their respective ground states.

In ^{12}C the least bound state is the $p_{3/2}$ orbital for both, the neutron and the proton, for which the radial components are shown in figure 2.4. In that figure, the upper component f (solid line) and the lower component g (dashed line) are shown as functions of the radial distance r. The magnitude of g is much smaller than that of f, which justifies the name "small" component for it. Non-relativistic calculations neglect this component but as we will see, in momentum space they may become comparable in magnitude for some momentum transfers.

2.5 Λ bound states

The Λ, in contrast to an additional nucleon, can occupy any bound state since it is not subject to the Pauli exclusion principle with respect to the nucleons and it is the only fermion of its kind in the final hypernucleus. This property makes it an excellent probe for single bound states in a nuclear potential.

For the actual calculation we use the well-depth search method, where the depth

of the vector and scalar potentials are fitted to reproduce the experimental binding energies of the bound states. The theoretical models involved are for example [59], which is an extension of [58] to hypernuclei and reproduces the experimental binding energies quite well. We have summarised these together with the potential parameters for our simple potential model in table 2.4.

state	E_{bind} [MeV]	V_{v} [MeV]	$r_{0\text{v}}$ [fm]	a_{v} [fm]	V_{s} [MeV]	$r_{0\text{s}}$ [fm]	a_{s} [fm]
$s_{1/2}$	10.79 ± 0.11	171.5230	1.1486	0.3960	−211.7654	1.1207	0.4764
$p_{3/2}$	0.10 ± 0.04	171.5230	1.1486	0.3960	−211.7654	1.1207	0.4764
$p_{1/2}$	0.10 ± 0.20	200.6974	0.983	0.5779	−247.7746	0.9825	0.6064

Table 2.4: Potential parameters for the vector and scalar potentials of the ${}^{12}_{\Lambda}\text{C}$ hypernucleus.

There are data available from the late 1980's and early 1990's [44, 71], and more recent data [42]. All those seem to agree on a binding energy of around (10.79 ± 0.11) MeV for the $s_{1/2}$ orbit in ${}^{12}_{\Lambda}\text{C}$ [50, 72–74]. According to these data, the $p_{3/2}$ orbital has a binding energy of (0.10 ± 0.04) MeV [42]. The $p_{1/2}$ state is most likely unbound and we omitted it when fitting the potential parameters shown in table 2.4.

The lowest lying bound state for the Λ hyperon is $s_{1/2}$, which is plotted in figure 2.5. The other possible bound states for the Λ are $p_{1/2}$ and $p_{3/2}$, which are shown in figures 2.6, and 2.7, respectively. Again, the magnitude of the lower component g (dashed line) is smaller than that of the upper component f (solid line). This difference is more pronounced in the $s_{1/2}$ and $p_{3/2}$ states and less so in the case of the $p_{1/2}$ orbital.

Since the neutron and Λ are both neutral particles, they are supposed to behave similarly in the nucleus. The Λ, however, has a much lower binding energy, which is still not fully understood and subject to active research in nuclear structure theory. An often quoted idea is that only the u- and d-quarks are interacting with the surrounding nuclear medium, reducing the effective potential by 30 %. However, this simple idea is excluded by experimental data which have shown that this reduction is more likely to be 50 %. A more quantitative measure of this difference is the volume integral of the potential, given by

$$I := \frac{1}{A} \int_{\mathbb{R}^3} V(\boldsymbol{x}) \, \mathrm{d}^3 x \ ,$$

which evaluates to

$$I = \frac{4\pi R^3 V_0}{3} \left[1 + \left(\frac{\pi a}{R} \right)^2 \right] \ .$$

We can then build the ratio of these integrals for both, the scalar and the vector

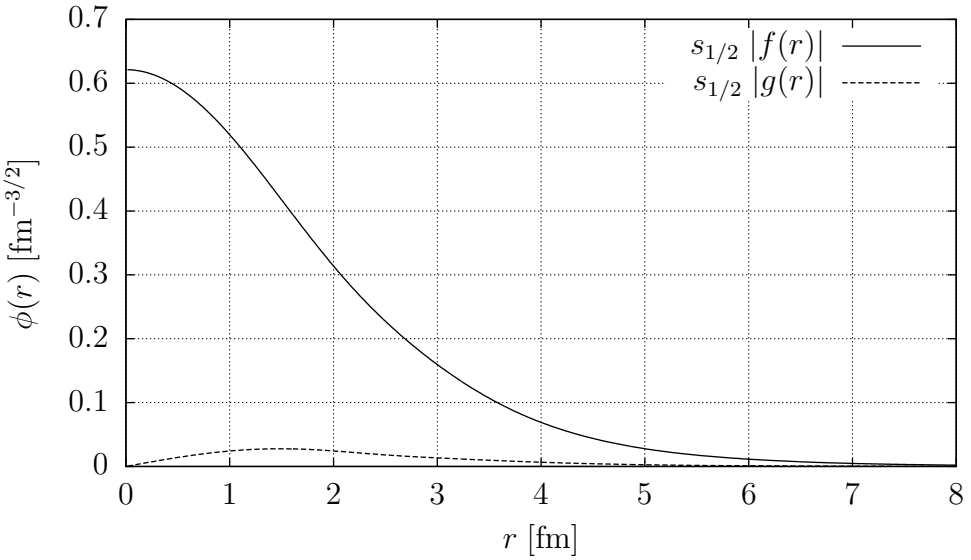

Figure 2.5: ${}^{12}_{\Lambda}$C hypernucleus Λ wave function for the $s_{1/2}$ orbital in coordinate space, where the solid line is the upper component, and the dashed line the lower component.

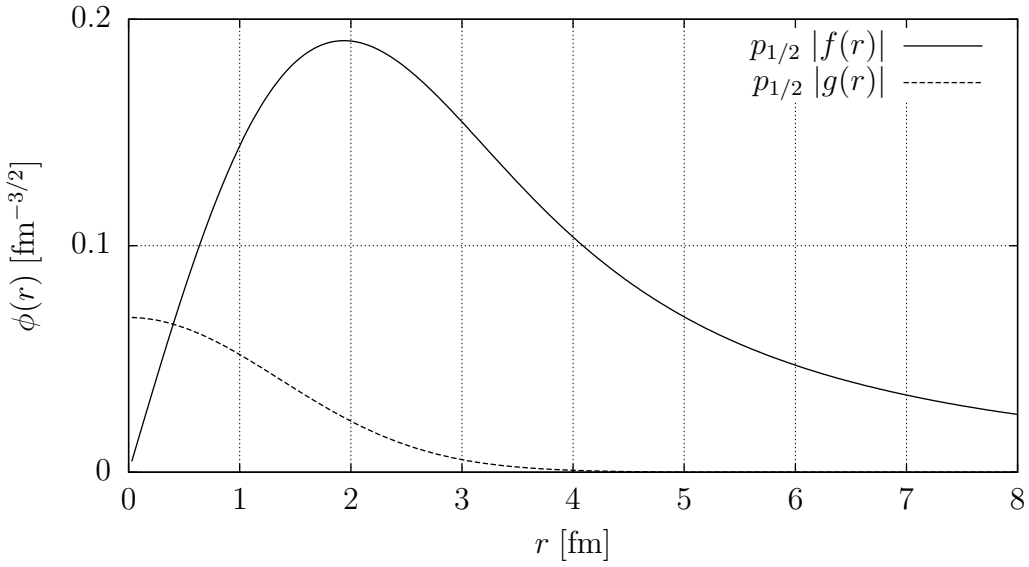

Figure 2.6: ${}^{12}_{\Lambda}$C hypernucleus Λ wave function for the $p_{1/2}$ orbital in coordinate space, where the solid line is the upper component, and the dashed line the lower component.

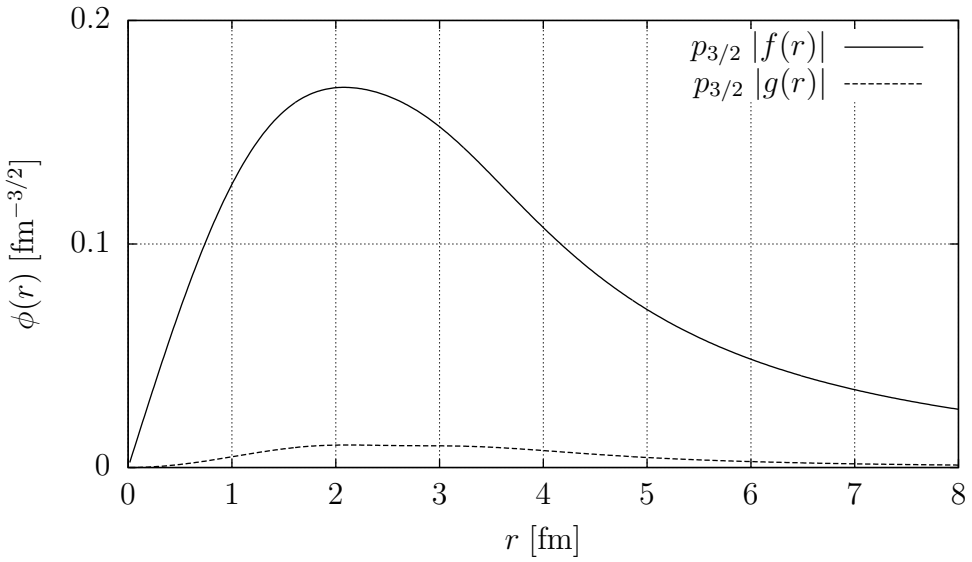

Figure 2.7: ${}^{12}_{\Lambda}$C hypernucleus Λ wave function for the $p_{3/2}$ orbital in coordinate space, where the solid line is the upper component, and the dashed line the lower component.

potential,

$$R_{\Lambda}^{(\mathrm{s,v})} := \frac{I_{\Lambda}^{(\mathrm{s,v})}}{I_{\mathrm{N}}^{(\mathrm{s,v})}} \, .$$

Plugging in the numbers from table 2.3 and table 2.4, we get for the ratios

$$R_{\Lambda}^{\mathrm{s}} = 0.539 \, , \quad R_{\Lambda}^{\mathrm{v}} = 0.536 \, .$$

Another quantitative measure of the bound state's spatial extension is the root-mean-square (rms) radius. The rms-radii for the neutron and Λ bound states are shown in table 2.5, where the relation to the different binding energies of the particles is evident. The Λ states have much larger radii than the corresponding neutron orbitals, reflecting their smaller binding energies.

	rms radius [fm]	
bound state	neutron	Λ
$s_{1/2}$	1.89	2.43
$p_{3/2}$	2.50	7.18

Table 2.5: Root-mean-square radii in fm of the nuclear and hypernuclear orbits in ^{12}C and ${}^{12}_{\Lambda}$C.

For a visual comparison, we show the wave functions for the neutron and the Λ for the same orbital, the $p_{3/2}$ state, in figure 2.8. As discussed above, the magnitudes

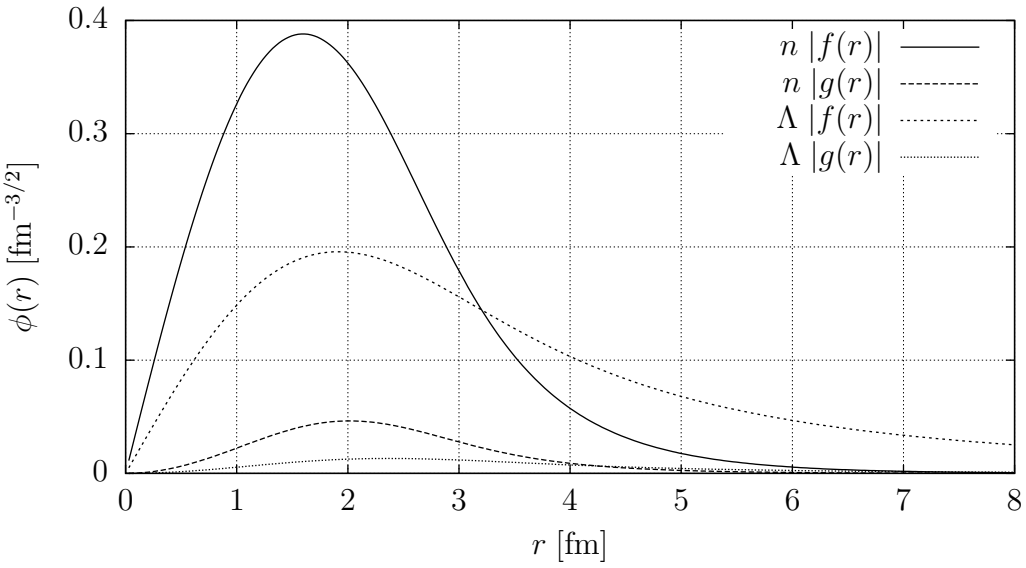

Figure 2.8: ^{12}C and $^{12}_{\Lambda}$C neutron and Λ wave functions for the $p_{3/2}$ orbital in coordinate space.

of the radial functions of the Λ are approximately half as large as the nucleon components but reach out much further.

2.6 Momentum space wave functions

In section 2.4, we described how we obtain a realistic model of the nucleon and hyperon wave functions needed for our calculations. These functions are calculated in coordinate space. But to be useful for our calculations of the reaction amplitudes, we need to transform them to momentum space by a Fourier transformation

$$\widehat{\psi}(\boldsymbol{k}) = \int_{\mathbb{R}^3} \mathrm{e}^{-\mathrm{i}\boldsymbol{k}\,\cdot\,\boldsymbol{x}}\, \psi(\boldsymbol{x})\, \mathrm{d}^3x \ .$$

Using the partial wave decomposition for plane waves

$$\mathrm{e}^{-\mathrm{i}\boldsymbol{k}\,\cdot\,\boldsymbol{x}} = 4\pi \sum_{\ell=0}^{\infty} \sum_{m=-\ell}^{\ell} (-\mathrm{i})^{\ell} j_{\ell}(kr) Y_{\ell m}(\hat{k}) Y^{*}_{\ell m}(\hat{x}) \ , \tag{2.12}$$

we can split the Fourier transformed wave function $\widehat{\psi}$ again into a part depending on the magnitude of the three-momentum and an angular part [75]. In analogy to (2.9), we write

$$\widehat{\psi}(\boldsymbol{k}) = \begin{pmatrix} \hat{f}_{n,j}(k)\, \mathcal{Y}^{jm_j}_{\ell s}(\hat{k}) \\ -\mathrm{i}\hat{g}_{n,j}(k)\, \mathcal{Y}^{jm_j}_{\ell' s}(\hat{k}) \end{pmatrix} \ ,$$

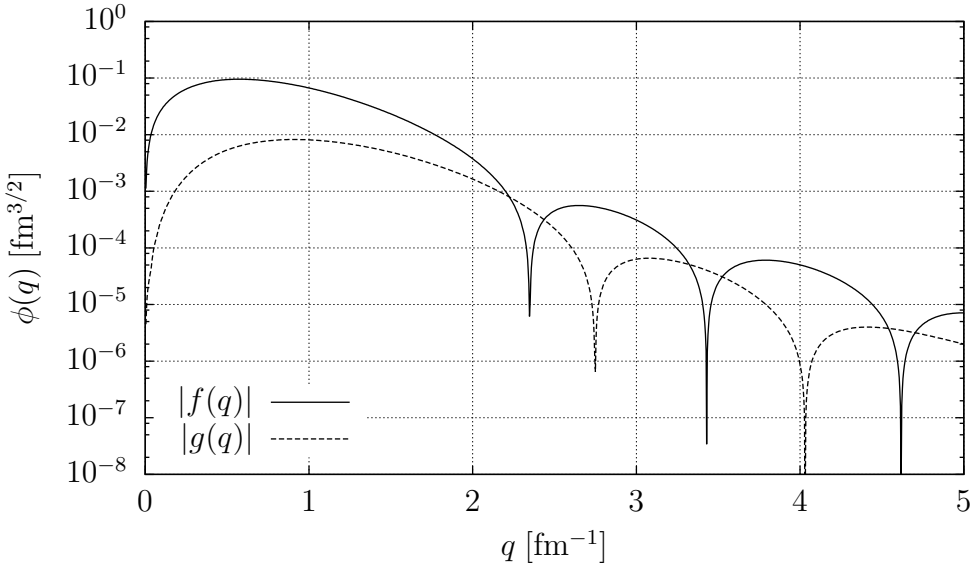

Figure 2.9: ^{12}C $p_{3/2}$ orbital in momentum space.

and the coupled spherical harmonics $\mathcal{Y}$ are given by (2.10), which translates to

$$\mathcal{Y}^{jm_j}_{\ell\frac{1}{2}}(\hat{k}) = \begin{pmatrix} \langle \ell, m_\ell - \frac{1}{2}, \frac{1}{2}, +\frac{1}{2} | j, m_j \rangle \, Y_{\ell, m_\ell - \frac{1}{2}}(\hat{k}) \\ \langle \ell, m_\ell + \frac{1}{2}, \frac{1}{2}, -\frac{1}{2} | j, m_j \rangle \, Y_{\ell, m_\ell + \frac{1}{2}}(\hat{k}) \end{pmatrix} .$$

The radial parts of the momentum space wave functions are given by [75]

$$\widehat{f}(k) = \frac{1}{2\pi^2} \int_0^\infty j_\ell(kr) f(r) \, r^2 \mathrm{d}r \ ,$$

$$\widehat{g}(k) = \frac{1}{2\pi^2} \int_0^\infty j_\ell(kr) g(r) \, r^2 \mathrm{d}r \ .$$

The functions f and g, and therefore $\widehat{f}$ and $\widehat{g}$, are real valued functions. An additional δ-function fixes the zeroth component of the momentum to the on-shell energy of the particle.

For the illustrations, we start again with the nucleon bound states in momentum space. Figure 2.9 shows the $p_{3/2}$ orbital of a neutron in ^{12}C. The Λ bound states of $^{12}_{\Lambda}$C in momentum space are shown in figure 2.10 ($s_{1/2}$), figure 2.11 ($p_{3/2}$), and the questionable $p_{1/2}$ bound state is shown in figure 2.12.

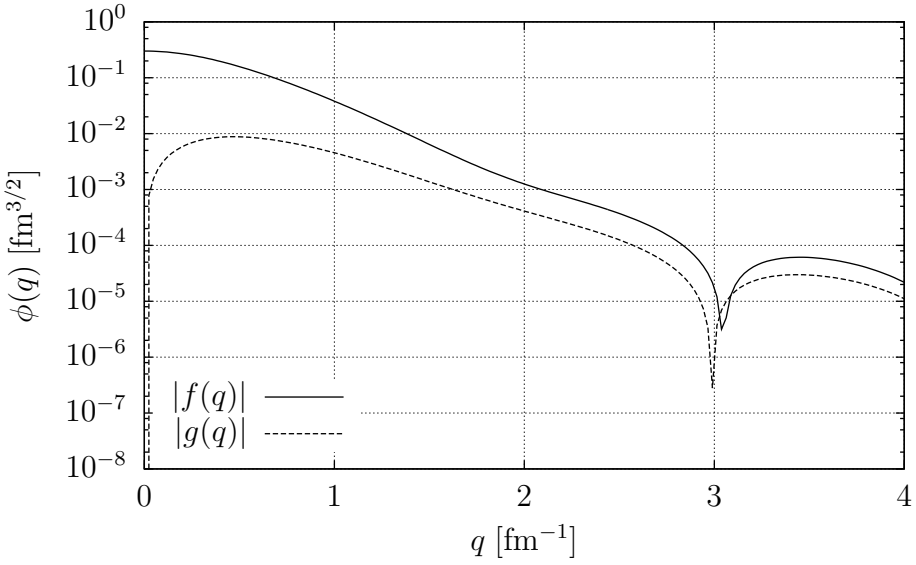

Figure 2.10: ${}^{12}_{\Lambda}$C $s_{1/2}$ orbital in momentum space.

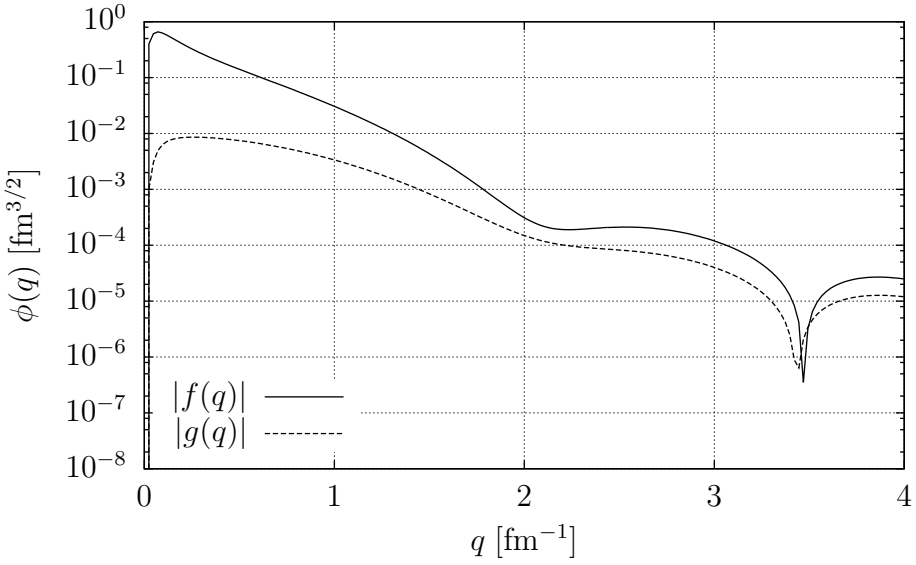

Figure 2.11: ${}^{12}_{\Lambda}$C $p_{3/2}$ orbital in momentum space.

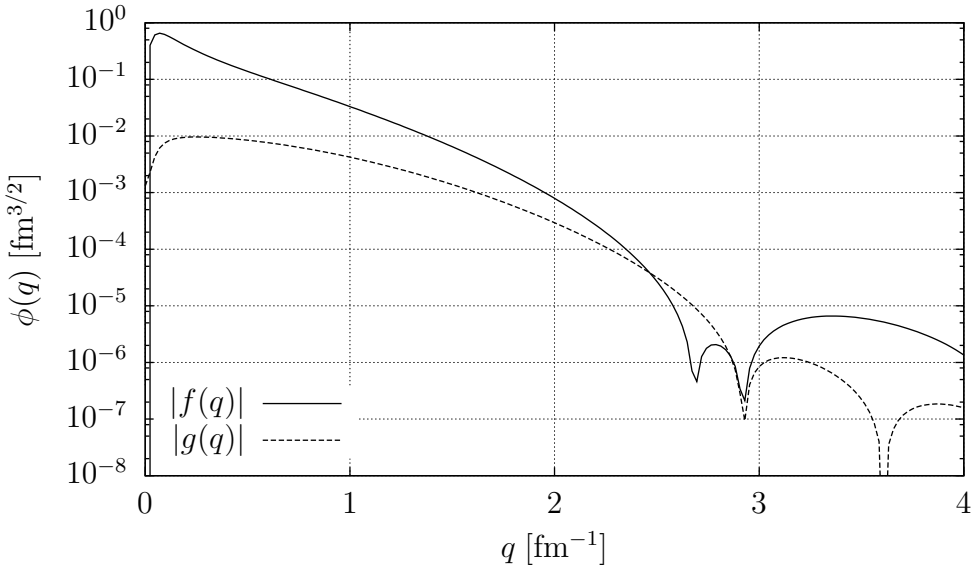

Figure 2.12: ${}^{12}_{\Lambda}\mathrm{C}$ $p_{1/2}$ orbital in momentum space.

3 Resonance Model for Strangeness Production on a Nucleus

The central issue of this thesis is to model the production of hypernuclei in pion-nucleus reactions. Therefore we have, among other things, to describe the complicated interaction of a pion with a nucleus. In this chapter we are going into the details of our model, disentangling the main reaction process from the nuclear corrections.

3.1 General features of pion-nucleus interactions

A simplified view of the regarded process is depicted in figure 3.1 and it involves, in principle, the simultaneous interaction of the meson with all the nucleons. Hereby, the pion interacts with the nucleus A producing a K-meson and a Λ-baryon. In the following, the kaon is measured in the detector and the Λ is captured into an orbit of the residual nucleus, forming a hypernucleus ${}_{\Lambda}\mathrm{B}$.

At projectile energies T_{lab} larger than the nuclear Fermi energy ε_{F}, $T_{\mathrm{lab}} \gg \varepsilon_{\mathrm{F}}$, the reaction mechanism is dominated by one-step processes where the pion interacts with only one of the target nucleons. Under such conditions, we are allowed to use the *impulse approximation*, which is depicted schematically in figure 3.2. The details of the pion-nucleon interaction, indicated therein by the grey box, are laid down in the following sections.

The elastic interactions with the remaining nucleons are taken into account as initial and final state interactions and are treated separately. In the left panel of figure 3.3, the impulse approximation is improved by including the initial state interactions of the pion which are indicated by the additional vertical box. The right panel of the same figure shows the inclusion of the final state interactions of the kaon in a similar way.

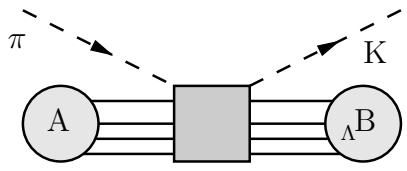

Figure 3.1: Schematic picture of the $\pi + \mathrm{A} \rightarrow \mathrm{K} + {}_{\Lambda}\mathrm{B}$ invloving all the nucleons in the process.

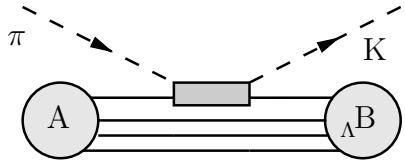

Figure 3.2: Schematic picture of the process $\pi + \mathrm{A} \rightarrow \mathrm{K} + {}_{\Lambda}\mathrm{B}$ in the impulse approximation, excluding initial and final state interactions.

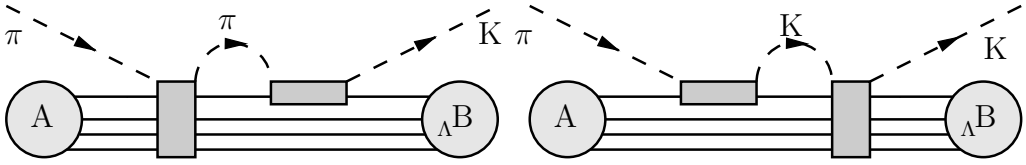

Figure 3.3: Pion scattering indicating the interaction with one nucleon and the initial state interactions of the pion (left) and the final state interactions of the kaon (right).

The next step is to combine these effects and an even more complete picture arises if we take both, initial and final state interactions into account. This is shown in figure 3.4 and it is the most complete description we can get in the framework of the impulse approximation and should give the most accurate results. In both pictures, the horizontal box stands for the explicitly treated interaction, while the vertical boxes include the effective model for the elastic interactions. The advantage of disentangling the production process from the in-medium interactions in this way is that the latter can be dealt with by means of effective models.

3.2 Resonance model for strangeness production

We first turn to the production vertex depicted in figure 3.2. Our model for this production process is based on the excitation and decay of nucleon resonances. In this chapter, we will describe this model in detail, including the involved resonances and Lagrangians, as well as their evaluation to scattering matrix elements and amplitudes. This approach was already successfully applied to strangeness production in proton-proton [51] and proton-nucleus [54] reactions, as well as to

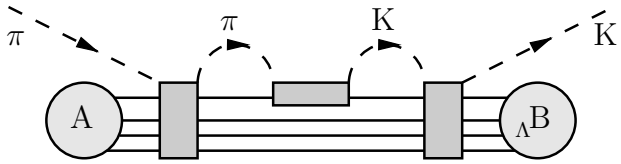

Figure 3.4: Pion scattering indicating the interaction with one nucleon and both, the initial and final state interactions of the mesons.

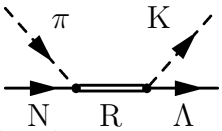

Figure 3.5: Tree diagram for the elementary process of pion-induced strangeness production via resonance excitation and decay on a single nucleon.

the photoproduction of hypernuclei [55].

The key idea of this approach is that the pion interacts with a nucleon, producing an intermediate resonance which subsequently decays into a kaon and a Λ. This process is illustrated in figure 3.5 in terms of a Feynman-diagram, where time goes from left to right. We then use the usual Feynman rules to calculate the scattering amplitudes and cross sections for different resonances. Since we are interested in strangeness production, we take only these resonances into account that have a significant branching ratio into the KΛ-channel and which have a mass that can be reached with the available centre-of-mass energy. There are three major resonances which play an important role and which are listed in table 3.1.

resonance	width [MeV]	decay channel	branching ratio	g
$\mathrm{N}(1650)\,\mathrm{S}_{11}$	150	$\mathrm{N}\pi$	0.700	0.8096
		$\mathrm{N}\rho$	0.080	2.6163
$\frac{1}{2}\left(\frac{1}{2}^-\right)$		$\mathrm{N}\omega$		1.8013
		$\mathrm{N}\sigma$	0.025	2.5032
		$\mathrm{K}\Lambda$	0.070	0.7658
$\mathrm{N}(1710)\,\mathrm{P}_{11}$	100	$\mathrm{N}\pi$	0.150	1.0414
		$\mathrm{N}\rho$	0.150	4.1421
$\frac{1}{2}\left(\frac{1}{2}^+\right)$		$\mathrm{N}\omega$	0.130	1.2224
		$\mathrm{N}\sigma$	0.170	0.6737
		$\mathrm{K}\Lambda$	0.150	6.1155
$\mathrm{N}(1720)\,\mathrm{P}_{13}$	150	$\mathrm{N}\pi$	0.150	0.1469
		$\mathrm{N}\rho$	0.700	19.483
$\frac{1}{2}\left(\frac{3}{2}^+\right)$		$\mathrm{N}\omega$		16.766
		$\mathrm{N}\sigma$	0.120	1.5557
		$\mathrm{K}\Lambda$	0.080	1.0132

Table 3.1: Coupling constants and branching fractions into various decay channels of the resonances included in our calculations, taken from [76], which are derived from [51, 77–80].

3.3 Lagrangian approach to the resonance model

The general Lagrangian $\mathcal{L}$ used in our nuclear model (see chapter 2) consists of a free part ($\mathcal{L}_{\mathrm{B}}$ from (2.1) and $\mathcal{L}_{\mathrm{M}}$ from (2.2)) and an interaction part $\mathcal{L}_{\mathrm{int}}$ given by (2.3). It can, in principle, also be used to calculate the elementary reaction process as shown in figure 3.5. However, since our aim is to describe the production of particles containing a strange quark, we need additional interaction terms which couple also the Λ-baryons and the strange mesons to the other fields. These additional terms connect the pion to a nucleon and a nucleon resonance, as well as the nucleon resonance to a kaon and a Λ-baryon. Thus, the full Lagrangian is composed of the free terms and the interaction terms as

$$\mathcal{L} = \mathcal{L}_{\mathrm{B}} + \mathcal{L}_{\mathrm{M}} + \mathcal{L}_{\mathrm{int}} + \mathcal{L}_{\mathrm{int}}^{\mathrm{mR}} \ .$$

In this section, the particulars of the construction of these additional interaction terms, denoted by $\mathcal{L}_{\mathrm{int}}^{\mathrm{mR}}$ above, are discussed. Nowadays, there are many nucleon resonances known but their properties are determined with high accuracy [17] only for a part of them. For tractability, however, we have to restrict ourselves to the ones with a sizeable branching fraction into the channels we are interested in. This leads to the inclusion of the spin-1/2 and spin-3/2 resonances as shown in table 3.1. The notation in the first column of this table is as follows: the number in parenthesis is the pole mass and S and P are indicating the orbital angular momenta $L = 0$ and $L = 1$, respectively. In the line below, the quantum numbers are listed as $I(J^P)$ [17], with the isospin I, the total angular momentum J, and the parity P.

Besides coupling the particles with their correct spin, the interaction Lagrangians have to respect the symmetries of strong interactions. This implies, besides being a Lorentz-scalar and hermitean, invariance under parity exchange, charge conjugation, and time reversal. While invariance under parity exchange differentiates between even and odd parity resonances, invariance under charge conjugation distinguishes between real and imaginary coupling constants. Explicit details about these symmetries are given in appendix C.

3.3.1 Spin-1/2 resonances

A spin-1/2 resonance behaves in principle like an ordinary nucleon but with a larger mass. For the interaction terms of the spin-1/2 resonances there are two choices, called *pseudoscalar* (PS) and *pseudovector* (PV). In pion-nucleon scattering processes the cross section vanishes as the pion momentum approaches zero. This is called the *chiral limit* and the pseudovector type ensures the right behaviour of the interaction cross section when one approaches this limit. In contrast to that, the pseudoscalar one does not respect the chiral limit but is easier to evaluate. The couplings in both cases are fixed in such a way that they are equal on-shell, and far off-shell, the difference is suppressed due to the denominator of the resonance

propagator. It is therefore arguable which Lagrangian to use in our case, and the best approach would be to introduce a mixing parameter as was investigated in [81].

To avoid the introduction of additional parameters in our model due to a PS-PV mixing for the interaction Lagrangians [81], we use the convention used in [79, 82]. This is in line with former analyses [83] and the discussion in [84], thus, we use the pseudovector Lagrangians (3.2) for the $1/2^+$ resonance and the pseudoscalar ones (3.1) for the $1/2^-$ resonance.

The pseudoscalar interaction Lagrangians for the spin-1/2 resonances are given by

$$\mathcal{L}^{\mathrm{PS}}_{\pi\mathrm{NR}} = -g_{\pi\mathrm{NR}}\bar{\psi}_{\mathrm{R}}\Gamma(\boldsymbol{\tau}\cdot\boldsymbol{\phi}_\pi)\psi_{\mathrm{N}} + \text{h. c.}\,, \tag{3.1a}$$

$$\mathcal{L}^{\mathrm{PS}}_{\mathrm{RK}\Lambda} = -g_{\mathrm{R}\Lambda\mathrm{K}}\bar{\psi}_{\mathrm{R}}\Gamma\phi_{\mathrm{K}}\psi_\Lambda + \text{h. c.}\,, \tag{3.1b}$$

where the Γ takes care of parity conservation. We use

$$\Gamma = \begin{cases} \mathbb{1} & \text{for odd parity} \\ \mathrm{i}\gamma^5 & \text{for even parity} \end{cases}$$

and h. c. in (3.1) denotes the *hermitean conjugate*.

The pseudovector Lagrangians respect the chiral limit by coupling to the derivative of the pion wave function rather than to the wave function itself. This introduces an additional mass dimension, which is taken care of by a "rescaling" of the coupling constant. It also ensures the matching of the on-shell behaviour of both Lagrangians, PS and PV.

$$\mathcal{L}^{\mathrm{PV}}_{\pi\mathrm{NR}} = -\frac{g_{\pi\mathrm{NR}}}{m_{\mathrm{R}} \pm m_{\mathrm{N}}}\bar{\psi}_{\mathrm{R}}\gamma^\mu\Gamma\partial_\mu(\boldsymbol{\tau}\cdot\boldsymbol{\phi}_\pi)\psi_{\mathrm{N}} + \text{h. c.}\,, \tag{3.2a}$$

$$\mathcal{L}^{\mathrm{PV}}_{\mathrm{RK}\Lambda} = -\frac{g_{\mathrm{RK}\Lambda}}{m_{\mathrm{R}} \pm m_\Lambda}\bar{\psi}_{\mathrm{R}}\gamma^\mu\Gamma\partial_\mu\phi_{\mathrm{K}}\psi_\Lambda + \text{h. c.}\,, \tag{3.2b}$$

where Γ is given by

$$\Gamma = \begin{cases} \mathrm{i} & \text{for odd parity} \\ \gamma^5 & \text{for even parity}\,, \end{cases}$$

and the upper and lower signs are used for even and odd parity resonances, respectively.

3.3.2 Spin-3/2 resonance

The treatment of spin-3/2 particles goes back to Rarita and Schwinger [85], mathematically its wave function is given by the tensor product of a spin-1/2 and a spin-1 particle. It is described by a vector spinor field ψ^μ which satisfies the Dirac-equation for each Lorentz-index μ

$$(\mathrm{i}\not{\partial} - m)\psi^\mu = 0$$

and the additional constraints

$$\gamma_\mu \psi^\mu = 0 \; .$$

These equations are called *Rarita–Schwinger* equations [85].

For the interactions of spin-3/2 particles with a nucleon and a pion there are basically two choices, one is the *conventional* coupling given by

$$\mathcal{L}_{\pi\mathrm{NR}} = \frac{g_{\pi\mathrm{NR}}}{m_\pi} \bar{\psi}_{\mathrm{R}\mu} \Theta^{\mu\nu} \partial_\nu (\boldsymbol{\tau} \cdot \boldsymbol{\phi}_\pi) \psi_{\mathrm{N}} + \mathrm{h.\ c.} \tag{3.3}$$

with

$$\Theta^{\mu\nu} = \eta^{\mu\nu} + a \gamma^\mu \gamma^\nu \; . \tag{3.4}$$

The parameter a is related to the so-called off-shell parameter z [86, 87]. The disadvantage of this conventional approach is that in the resulting propagator non-propagating terms occur which project onto the spin-1/2 degrees of freedom of the particle which can be viewed as four-point contact interactions.

Another approach to model these interactions was proposed by Pascalutsa [88] based on a gauge invariant treatment of the interaction vertex. Instead of coupling the bare spinor ψ^μ to the other fields, and in analogy to vector (spin-1) fields, the field strength is coupled to them. This gauge-invariant Lagrangian reads

$$\mathcal{L} = g \varepsilon^{\mu\nu\alpha\beta} \partial_\mu \bar{\psi}_{\mathrm{R}\nu} \gamma_5 \gamma_\alpha \partial_\beta (\boldsymbol{\tau} \cdot \boldsymbol{\phi}_\pi) \psi_{\mathrm{N}} + \mathrm{h.\ c.} \; .$$

The Pascalutsa formalism has the advantage that only physical spin-3/2 degrees of freedom are propagated. As has been shown in [89], it is related to the conventional approach by a redefinition of the fields. Thus, it makes the separation of the propagating spin-3/2 parts and the background contributions explicit.

We use the couplings fixed in other reactions, for example strangeness production in nucleon-nucleon and nucleon-nucleus reactions as described in [51, 53] which uses the conventional approach. Since these couplings are already fixed to experimental data, we do not need to disentangle the resonance interaction from the point interaction. From (3.3) and (3.4) with the choice $z = -1/2$, the spin-3/2 resonance Lagrangians are given by

$$\begin{aligned} \mathcal{L}_{\pi\mathrm{NR}} &= \frac{g_{\pi\mathrm{NR}}}{m_\pi} \bar{\psi}^\mu_{\mathrm{R}} \partial_\mu (\boldsymbol{\tau} \cdot \boldsymbol{\phi}_\pi) \psi_{\mathrm{N}} + \mathrm{h.\ c.} \; , \\ \mathcal{L}_{\mathrm{RK}\Lambda} &= \frac{g_{\mathrm{RK}\Lambda}}{m_{\mathrm{K}}} \bar{\psi}^\mu_{\mathrm{R}} \partial_\mu \phi_{\mathrm{K}} \psi_\Lambda + \mathrm{h.\ c.} \; . \end{aligned}$$

3.4 Resonance Propagators

The two interaction vertices of figure 3.5 are connected by a resonance propagator. For the spin-1/2 resonance we have the simple spin-1/2 propagator, which is given by [62, 63]

$$\mathcal{D}_{1/2} = \mathrm{i} \frac{\not{p} + m}{p^2 - m^2 + \mathrm{i}\epsilon} \; . \tag{3.5}$$

The spin-3/2 propagator is given by [90–92]

$$\mathrm{i}\mathcal{D}^{\mu\nu}_{3/2} = \frac{\not{p}+m}{p^2-m^2+\mathrm{i}\epsilon}P^{\mu\nu}_{(3/2)} - \frac{2}{3m^2}(\not{p}+m)P^{\mu\nu}_{(1/2),22} + \frac{1}{\sqrt{3}m}(P^{\mu\nu}_{(1/2),12}+P^{\mu\nu}_{(1/2),21}) \ , \quad (3.6)$$

where $P^{\mu\nu}_{(3/2)}$ is the projection operator onto the spin-3/2 degrees of freedom

$$P^{\mu\nu}_{(3/2)} = \eta^{\mu\nu} - \frac{1}{3}\gamma^\mu\gamma^\nu - \frac{1}{3p^2}(\not{p}\gamma^\mu p^\nu + p^\mu\gamma^\nu\not{p})$$

and the $P_{(1/2)}$ project onto the (non-propagating) spin-1/2 states

$$P^{\mu\nu}_{(1/2),22} = \frac{p^\mu p^\nu}{p^2} \ ,$$
$$P^{\mu\nu}_{(1/2),12} = \frac{p_\lambda p^\nu \sigma^{\mu\lambda}}{\sqrt{3}p^2} \ ,$$
$$P^{\mu\nu}_{(1/2),21} = \frac{p^\mu p_\lambda \sigma^{\lambda\nu}}{\sqrt{3}p^2} \ .$$

Inserting these projectors into the propagator (3.6), the more commonly used form for the spin-3/2 projector [86, 93] is given by

$$P^{\mu\nu} = \eta^{\mu\nu} - \frac{1}{3}\gamma^\mu\gamma^\nu - \frac{2}{3m^2}p^\mu p^\nu + \frac{1}{3m}\left(p^\mu\gamma^\nu - p^\nu\gamma^\mu\right) \ , \quad (3.7)$$

such that the propagator $\mathcal{D}$ can be written as

$$\mathcal{D}^{\mu\nu}_{3/2} = -\mathrm{i}\frac{\not{p}+m}{p^2-m^2+\mathrm{i}\epsilon}P^{\mu\nu} \ . \quad (3.8)$$

3.4.1 Resonance width

Both propagators, (3.5) and (3.6) or (3.8), exhibit a pole at the mass-shell[1] $p^2 = m^2$, as we know from general quantum field theory [62, 63]. The two-point correlation function, which is the propagator in coordinate space, is given by the Fourier transforms of (3.5) and (3.8) and the resolution to the pole problem is to shift the integration curve away from the real axis or, equivalently, to add a small imaginary term $\mathrm{i}\epsilon$ to the denominator [62]. For stable particles such as nucleons, this seems to be an arbitrary choice, but it gives the correct description of the correlation function or, in other words, the amplitude for the propagation of a free particle.

Since resonances are unstable excitations, they have finite lifetimes and the additional shift terms in the propagators arise naturally and are given by the corresponding decay widths. Besides, the resonances in our case are excited and decay inside the nucleus in which, in contrast to the vacuum, additional collision processes

[1] In the case of the spin-3/2 particle and in our (conventional) approach this only applies to the spin-3/2 degrees of freedom. The spin-1/2 parts arising in this formalism have no pole, so they are not propagating but describe contact interactions, see the discussion in [89].

may lead to a modification of their lifetimes. In general, such effects would have to be taken into account by calculating the resonance self-energies [67, 94, 95], which are conveniently expressed as

$$\Pi(\omega, \boldsymbol{q}) = \Sigma(\omega, \boldsymbol{q}) - \frac{\mathrm{i}}{2}\Gamma(\omega, \boldsymbol{q}) \ ,$$

where the real and imaginary parts are related by a dispersion relation. The resulting modifications of the propagators then give rise to the spectral functions. Here, however, we only take the imaginary parts of the self-energies into account, which are related to the decay widths Γ of the individual resonances by

$$\Gamma(\omega, \boldsymbol{q}) = -2\,\Im\,\Pi(\omega, \boldsymbol{q}) \ .$$

These, in turn, lead to a shift of the pole masses into the complex plane via $m \mapsto m^* = m - \mathrm{i}\Gamma/2$.

In the following we use a simple parametrisation for the width from decays to the Nπ-channel, which follows the assumption that $\Gamma \sim p^{2L+1}$, where L is the intrinsic angular momentum of the resonance. In particular, the Nπ-width is given by [51]

$$\Gamma_{\mathrm{N}\pi} = \frac{3}{4\pi} g_{\mathrm{N}\pi}^2 \frac{E_{\mathrm{N}} \pm m_{\mathrm{N}}}{m} p_\pi^{\mathrm{cm}} \tag{3.9}$$

for the spin-1/2 resonances[2] $\mathrm{N}(1650)\,\mathrm{S}_{11}$ and $\mathrm{N}(1710)\,\mathrm{P}_{11}$, and by

$$\Gamma_{\mathrm{N}\pi} = \frac{1}{12\pi} \left(\frac{g_{\mathrm{N}\pi}}{m_\pi}\right)^2 \frac{E_{\mathrm{N}} \mp m_{\mathrm{N}}}{m} \left(p_\pi^{\mathrm{cm}}\right)^3 \tag{3.10}$$

for the spin-3/2 resonance $\mathrm{N}(1720)\,\mathrm{P}_{13}$. The upper and lower signs correspond to odd and even parity, respectively. The Nπ centre-of-mass momentum is given by

$$\left(p_\pi^{\mathrm{cm}}\right)^2 = \frac{1}{4m_{\mathrm{R}}^2} \left[m_{\mathrm{R}}^2 - (m_{\mathrm{N}} + m_\pi)^2\right] \left[m_{\mathrm{R}}^2 - (m_{\mathrm{N}} - m_\pi)^2\right] \ . \tag{3.11}$$

Note that (3.9) and (3.10) are the decay widths at the pole-mass of the resonance. They are used to obtain the coupling constants from the branching fractions as given in table 3.1. For the actual calculation of the scattering cross sections, we need the Nπ-width as a function of the resonance momentum p. This is given by [51, 96, 97]

$$\Gamma_{\mathrm{N}\pi} = \Gamma_0 \left(\frac{p_{\pi\mathrm{R}}^{\mathrm{cm}}}{p_\pi^{\mathrm{cm}}}\right)^{2L+1} \ ,$$

where p_π^{cm} is given by (3.11), and $p_{\pi\mathrm{R}}^{\mathrm{cm}}$ is given by (3.11), but replacing m_{R} with the four-momentum p of the resonance.

[2] In the case of the even parity resonance $\mathrm{N}(1710)\,\mathrm{P}_{11}$ and in the non-relativistic limit, $p_\pi^{\mathrm{cm}} \ll m_{\mathrm{N}}$, we obtain for the factor $E_{\mathrm{N}} - m_{\mathrm{N}} \approx (p_\pi^{\mathrm{cm}})^2/2m_{\mathrm{N}}$, and therefore $\Gamma \sim p^3 = p^{2L+1}$.

In addition to the Nπ decay, we take the resonance decays to the Nρ-channel into account. The ρ-meson itself is a resonance having, in our approximation, the spectral function

$$S(m) = -\frac{1}{\pi}\,\Im\,\mathcal{D}_\rho(m)\ ,$$

where $\mathcal{D}_\rho$ is the ρ-propagator

$$\mathcal{D}_\rho(m) = \frac{1}{m^2 - m_\rho^2 + \mathrm{i}m\Gamma_{\rho\to\pi\pi}}\ ,$$

and the ρ-decay-width into two pions can be expressed as

$$\Gamma_{\rho\to\pi\pi}(m) = \Gamma^0_{\rho\to\pi\pi}\frac{m_\rho^2}{m^2}\left(\frac{p_{\rho\to\pi\pi}(m)}{p_{\rho\to\pi\pi}(m_\rho)}\right)^3\ .$$

As in [51], we use for the on-shell width of the ρ-meson the value $\Gamma^0_{\rho\to\pi\pi} = 150$ MeV, and $p_{\rho\to\pi\pi}$ is given by

$$p^2_{\rho\to\pi\pi}(m) = \frac{(m^2 - 4m_\pi^2)m^2}{4m^2}\ .$$

The decay width of the resonance into this channel is then given by integrating over the spectral function

$$\Gamma(m) = 2\int\limits_{2m_\pi}^{m-m_\mathrm{N}} m'\Gamma^*(m')S(m')\,\mathrm{d}m'\ . \tag{3.12}$$

The function $\Gamma^*(m)$ for the spin-$1/2^+$ resonance is given by

$$\Gamma^*(m) = \frac{1}{4\pi}\left(\frac{g_{\mathrm{RN}\rho}}{2m_\mathrm{N}}\right)^2\left[4(E_\mathrm{N}+E_m)(p^\mathrm{cm})^2 + 3(E_\mathrm{N}-m_\mathrm{N})m^2\right]\frac{p_\pi^\mathrm{cm}}{m}\ ,$$

for the spin-$1/2^-$ resonance by

$$\Gamma^*(m) = \frac{1}{4\pi}\left(\frac{g_{\mathrm{RN}\rho}}{2m_\mathrm{N}}\right)^2\left[-4(E_\mathrm{N}+E_m)(p^\mathrm{cm})^2 - 3(E_\mathrm{N}+m_\mathrm{N})m^2\right]\frac{p_\pi^\mathrm{cm}}{m}\ ,$$

and for the spin-$3/2^+$ resonance we use

$$\Gamma^*(m) = \frac{1}{12\pi}\left(\frac{g_{\mathrm{RN}\rho}}{m+m_\mathrm{N}}\right)^2\left[2(2E_\mathrm{N}+E_m)(p^\mathrm{cm})^2 + 3(E_\mathrm{N}-m_\mathrm{N})m^2\right]\frac{p_\pi^\mathrm{cm}}{m}\ .$$

With these prerequisites, we can evaluate the integral (3.12). Together with the decay width into the Nπ-channel, $\Gamma_{\mathrm{N}\pi}$ from (3.9) and (3.10), the total width is given by

$$\Gamma = \Gamma_{\mathrm{N}\pi} + \Gamma_{\mathrm{N}\rho}\ .$$

It modifies the propagators (3.5) and (3.8), which yields

$$\mathcal{D}_{1/2} = \mathrm{i}\frac{\not{p} + m}{p^2 - (m - \mathrm{i}\Gamma/2)^2} \ ,$$
$$\mathcal{D}^{\mu\nu}_{3/2} = -\mathrm{i}\frac{\not{p} + m}{p^2 - (m - \mathrm{i}\Gamma/2)^2} P^{\mu\nu} \ ,$$

for the spin-1/2 and spin-3/2 resonances, respectively, with $P^{\mu\nu}$ from (3.7).

4 Reaction Theory

The theory and calculation of scattering processes has been extensively discussed in textbooks, see for example [62, 63, 70]. In this chapter, we will recapitulate the most important parts and introduce the notation used in our calculations. We start by describing the kinematics of the processes and end with a formula for the differential cross section containing the transition matrix element.

4.1 Kinematics

Pion-induced production of strange particles on nuclei can be seen as a two-body process on the pion-nucleus level. However, we have to distinguish between the elementary process on the nucleon, and the overall reaction on the nucleus as discussed in chapter 3. For the kinematics, we first look at the pion-nucleus reaction: $\pi + \mathrm{A} \to \mathrm{K} + {}_{\Lambda}\mathrm{A}$. Starting from the momentum four-vectors $p = (E, \boldsymbol{p})$ of the pion and the nucleus A, the total available centre-of-mass energy is given by

$$s = (p_\pi + p_\mathrm{A})^2 = (E_\pi + E_\mathrm{A})^2 - (\boldsymbol{p}_\pi + \boldsymbol{p}_\mathrm{A})^2$$

in any inertial system because it is a Lorentz-scalar. The πA-centre-of-mass frame is defined by $\boldsymbol{p}_\pi + \boldsymbol{p}_\mathrm{A} = 0$. Hence, in that frame the Lorentz-invariant total energy s is given by [70]

$$s = (E_\pi + E_\mathrm{A})^2 = m_\pi^2 + m_\mathrm{A}^2 + 2 m_\mathrm{A} E_\pi^\mathrm{lab} \ .$$

Here, m_π is the pion rest mass, m_A is the rest mass of the target nucleus A, and we use the superscript "lab" to distinguish the quantities in the laboratory frame from the ones in the centre-of-mass frame (without superscript). The energies of the incoming particles are, as usual, given by

$$E_\pi = \sqrt{|\boldsymbol{p}_\pi|^2 + m_\pi^2} \ ,$$
$$E_\mathrm{A} = \sqrt{|\boldsymbol{p}_\pi|^2 + m_\mathrm{A}^2} \ ,$$

and in terms of the pion kinetic energy in the laboratory frame, $T_\pi^{\text{lab}} = E_\pi^{\text{lab}} - m_\pi$, the magnitude of the relative momentum is given by

$$\begin{aligned} q^2 := |\boldsymbol{p}_\pi|^2 &= \frac{(s - m_\pi^2 - m_\text{A}^2)^2 - 4m_\pi^2 m_\text{A}^2}{2s} \\ &= \frac{m_\text{A}^2 T_\pi^{\text{lab}}(T_\pi^{\text{lab}} + 2m_\pi)}{s} \,. \end{aligned}$$

On the other hand, in terms of the four-momenta of the outgoing particles, the kaon and the hypernucleus B, the square of the total energy is equal to $s = (p_\text{K} + p_\text{B})^2$. Since in the centre-of-mass frame the condition $\boldsymbol{p}_\text{K} + \boldsymbol{p}_\text{B} = 0$ holds, the respective energies are then given in terms of Lorentz-invariant quantities by

$$\begin{aligned} E_\text{K} &= \frac{s - m_\text{B}^2 + m_\text{K}^2}{2\sqrt{s}} \,, \\ E_\text{B} &= \frac{s + m_\text{B}^2 - m_\text{K}^2}{2\sqrt{s}} \,, \end{aligned}$$

where we relabled the hypernucleus ${}_\Lambda$A to B for the sake of brevity. The respective momentum is then simply given by

$$|\boldsymbol{p}_\text{K}|^2 = E_\text{K}^2 - m_\text{K}^2 \,.$$

Knowing the magnitude of the kaon momentum, the direction of the outgoing kaon is given by the scattering angle θ_K with respect to the incoming pion beam. By giving $\cos\theta_\text{K}$ it is easy to calculate the differential cross section $\mathrm{d}\sigma/\mathrm{d}\cos\theta_\text{K}$ and $\mathrm{d}\sigma/\mathrm{d}\Omega_\text{K}$.

However, since we use the impulse approximation, our elementary reaction involves only a single nucleon. In addition to that, the process does not take place on free nucleons, rather on bound ones in the nucleus. The wave functions of these bound states are calculated in the (hyper)nucleus rest frame. So we need to boost the momenta to that very frame. The velocity of the nucleus A in the πA-centre-of-mass frame is given by

$$\boldsymbol{v}_\text{A} = \frac{\boldsymbol{p}_\text{A}}{E_\text{A}} \,,$$

and the z-direction is determined by the incoming pion, setting $\boldsymbol{p}_\pi^{\text{lab}} = (0, 0, p_\pi^{\text{lab}})$.

4.2 Cross sections

Applying standard methods [62, 63], adapted to the process at hand, the differential cross section $\mathrm{d}\sigma$ is given by

$$\mathrm{d}\sigma = \frac{\mathrm{d}^3 p_\text{K}}{(2\pi)^3} \frac{1}{2E_\text{K}} \frac{\mathrm{d}^3 p_\text{B}}{(2\pi)^3} \frac{m_\text{B}}{E_\text{B}} \frac{1}{2E_\pi} \frac{m_\text{A}}{E_\text{A}} \frac{|\mathcal{M}|^2}{v_\text{i}} (2\pi)^4 \delta^{(4)} \left(p_\pi + p_\text{A} - (p_\text{K} + p_\text{B})\right) \,. \quad (4.1)$$

We evaluate (4.1) in the πA-centre-of-mass frame, where the relative incident velocity v_i is given by

$$\begin{aligned} v_\mathrm{i} &= |\boldsymbol{v}_\pi - \boldsymbol{v}_\mathrm{A}| = \left|\frac{\boldsymbol{p}_\pi}{E_\pi} - \frac{\boldsymbol{p}_\mathrm{A}}{E_\mathrm{A}}\right| = \left|\frac{\boldsymbol{p}_\pi}{E_\pi} + \frac{\boldsymbol{p}_\pi}{E_\mathrm{A}}\right| \\ &= |\boldsymbol{p}_\pi|\left|\frac{1}{E_\pi} + \frac{1}{E_\mathrm{A}}\right| = |\boldsymbol{p}_\pi|\frac{|E_\pi + E_\mathrm{A}|}{E_\pi E_\mathrm{A}} = |\boldsymbol{p}_\pi|\frac{\sqrt{s}}{E_\pi E_\mathrm{A}} \,, \end{aligned} \tag{4.2}$$

with the total centre-of-mass energy $\sqrt{s} = E_\pi + E_\mathrm{A}$. Using (4.2) in (4.1) then leads to

$$\mathrm{d}\sigma = \frac{1}{(2\pi)^2}\frac{\mathrm{d}^3p_\mathrm{K}}{2E_\mathrm{K}}\frac{\mathrm{d}^3p_\mathrm{B}}{2E_\mathrm{B}}\frac{m_\mathrm{A}m_\mathrm{B}}{|\boldsymbol{p}_\pi|}\frac{|\mathcal{M}|^2}{\sqrt{s}}\delta^{(4)}\left(p_\pi + p_\mathrm{A} - (p_\mathrm{K} + p_\mathrm{B})\right) \,.$$

The interesting quantity for us is the differential cross section with respect to the kaon solid angle $\mathrm{d}\Omega_\mathrm{K}$. For this purpose, we express the integral measure d^3p_K in spherical coordinates, using $\mathrm{d}^3p_\mathrm{K} = |\boldsymbol{p}_\mathrm{K}|^2\,\mathrm{d}|\boldsymbol{p}_\mathrm{K}|\,\mathrm{d}\Omega_\mathrm{K}$. We then obtain the differential cross section $\mathrm{d}\sigma/\mathrm{d}\Omega_\mathrm{K}$ by integrating over the kaon energy E_K and the three-momentum d^3p_B of the undetected hypernucleus B. Using spherical coordinates, the three-dimensional integral is separated in an obvious way into an energy and an angular part

$$\mathrm{d}^3p_\mathrm{K} = \boldsymbol{p}_\mathrm{K}^2\frac{\mathrm{d}|\boldsymbol{p}_\mathrm{K}|}{\mathrm{d}E_\mathrm{K}}\,\mathrm{d}E_\mathrm{K}\,\mathrm{d}\Omega_\mathrm{K} \,, \tag{4.3}$$

and by using $E_\mathrm{K} = \sqrt{\boldsymbol{p}_\mathrm{K}^2 + m_\mathrm{K}^2}$, we have

$$\frac{\mathrm{d}E_\mathrm{K}}{\mathrm{d}|\boldsymbol{p}_\mathrm{K}|} = \frac{|\boldsymbol{p}_\mathrm{K}|}{E_\mathrm{K}} \,. \tag{4.4}$$

Integrating (4.1) with the help of (4.3) and (4.4), we get

$$\frac{\mathrm{d}\sigma}{\mathrm{d}\Omega_\mathrm{K}} = \frac{1}{(2\pi)^2}\frac{m_\mathrm{A}m_\mathrm{B}}{|\boldsymbol{p}_\pi|\sqrt{s}}\int_0^\infty \mathrm{d}E_\mathrm{K}\frac{|\boldsymbol{p}_\mathrm{K}|}{2}\int_{\mathbb{R}^3}\frac{\mathrm{d}^3p_\mathrm{B}}{2E_\mathrm{B}}\,\delta^{(4)}\left(p_\pi + p_\mathrm{A} - (p_\mathrm{K} + p_\mathrm{B})\right)|\mathcal{M}|^2 \,. \tag{4.5}$$

The three-dimensional integral can be rewritten as a four-dimensional one using the identity [62]

$$\int_{\mathbb{R}^3}\frac{\mathrm{d}^3p}{2E} = \int_{\mathbb{R}^4}\mathrm{d}^4p\,\delta(p^2 - m^2)\Theta(p^0) \,. \tag{4.6}$$

Using (4.6) and the four-dimensional δ-function, which fixes the hypernucleus' momentum p_B, we can write (4.5) as

$$\frac{\mathrm{d}\sigma}{\mathrm{d}\Omega_\mathrm{K}} = \frac{1}{(2\pi)^2}\frac{m_\mathrm{A}m_\mathrm{B}}{2\sqrt{s}|\boldsymbol{p}_\pi|}\int_0^{\sqrt{s}}\mathrm{d}E_\mathrm{K}|\boldsymbol{p}_\mathrm{K}|\,\delta\left((p_\pi + p_\mathrm{A} - p_\mathrm{K})^2 - m_\mathrm{B}^2\right)|\mathcal{M}|^2 \,. \tag{4.7}$$

In the centre-of-mass frame we have

$$(p_\pi + p_\mathrm{A} - p_\mathrm{K})^2 = (p_\pi + p_\mathrm{A})^2 + p_\mathrm{K}^2 - 2p_\mathrm{K}\cdot(p_\pi + p_\mathrm{A}) = s + m_\mathrm{K}^2 - 2E_\mathrm{K}\sqrt{s}\ ,$$

and we can therefore substitute the argument of the δ-function in (4.7). This gives

$$\frac{\mathrm{d}\sigma}{\mathrm{d}\Omega_\mathrm{K}} = \frac{1}{(2\pi)^2}\frac{m_\mathrm{A}m_\mathrm{B}}{4s|\boldsymbol{p}_\pi|}\int\limits_0^{\sqrt{s}} \mathrm{d}E_\mathrm{K}|\boldsymbol{p}_\mathrm{K}|\,\delta(E_\mathrm{K} - \widetilde{E}_\mathrm{K})|\mathcal{M}|^2\ ,$$

where $\widetilde{E}_\mathrm{K}$ is the kaon centre-of-mass energy

$$\widetilde{E}_\mathrm{K} = \frac{s - m_\mathrm{B}^2 + m_\mathrm{K}^2}{2\sqrt{s}}\ .$$

Thus, the final expression for the differential cross section is[1]

$$\frac{\mathrm{d}\sigma}{\mathrm{d}\Omega_\mathrm{K}} = \frac{1}{16\pi^2}\frac{m_\mathrm{A}m_\mathrm{B}}{s}\frac{|\boldsymbol{p}_\mathrm{K}(\widetilde{E}_\mathrm{K})|}{|\boldsymbol{p}_\pi|}|\mathcal{M}(E_\mathrm{K} = \widetilde{E}_\mathrm{K})|^2\ . \tag{4.8}$$

4.3 Matrix Elements

The dynamics of the reaction is contained in the matrix element $\mathcal{M}$ which, in turn, is needed for the calculation of the cross section (4.8). For pion-induced strangeness production on a nucleon it is given in coordinate space by

$$\mathcal{M} = \int \mathrm{d}^4x\,\mathrm{d}^4y\ \bar{\psi}_\Lambda(x)\phi_\mathrm{K}^*(x)\Gamma_1 G_\mathrm{R}(x,y)\Gamma_2\phi_\pi(y)\psi_\mathrm{N}(y)\ . \tag{4.9}$$

Γ_1 and Γ_2 are the interaction vertex factors determined by the Lagrangians as described in section 3.3, and the resulting Feynman rules as described in appendix B. To continue the calculation, we first substitute the nucleon and Λ wave functions by their Fourier transforms. Then, we use the resonance propagator $G(x,y)$ in coordinate space. It is related to (3.5) and for a freely moving spin-1/2 particle it is given by [62]

$$G_\mathrm{R}(x,y) = \int\limits_{\mathbb{R}^4}\frac{\mathrm{d}^4p}{(2\pi)^4}\,\mathrm{i}\frac{\not{p} + m_\mathrm{R}}{p^2 - m_\mathrm{R}^2 + \mathrm{i}\epsilon}\,\mathrm{e}^{-\mathrm{i}p\,\cdot\,(x-y)}\ . \tag{4.10}$$

For spin-3/2 resonances, the integrand has to be multiplied by the additional spin-projection operator $P^{\mu\nu}$, which is defined by (3.7).

[1] Note that, according to [17, 62], the differential cross section for the two-body-reaction at hand would be given by

$$\frac{\mathrm{d}\sigma}{\mathrm{d}\Omega_\mathrm{K}} = \frac{1}{64\pi^2}\frac{|\boldsymbol{p}_\mathrm{K}|}{|\boldsymbol{p}_\pi|}\frac{|\mathcal{M}|^2}{s}\ .$$

The difference in the prefactor between (4.8) and this formula stems from the different normalisations used for the asymptotic states that are involved in the reaction. We go into the details of this discrepancy in appendix E.

The matrix element $\mathcal{M}$ (4.9) for the pseudoscalar case with these substitutions then reads

$$\begin{aligned}\mathcal{M} = \int \mathrm{d}^4x\, \mathrm{d}^4y\, \frac{\mathrm{d}^4k_\Lambda}{(2\pi)^4}\frac{\mathrm{d}^4k_\mathrm{N}}{(2\pi)^4}\frac{\mathrm{d}^4p}{(2\pi)^4}\, \mathrm{e}^{\mathrm{i}k_\Lambda\cdot x}\, \mathrm{e}^{-\mathrm{i}k_\mathrm{N}\cdot y}\, \mathrm{e}^{-\mathrm{i}p\cdot(x-y)} \\ \times \bar{\psi}_\Lambda(k_\Lambda)\phi^*_\mathrm{K}(x)\Gamma_1\, \mathrm{i}\frac{\not{p}+m_\mathrm{R}}{p^2-m_\mathrm{R}^2+\mathrm{i}\epsilon}\Gamma_2\phi_\pi(y)\psi_\mathrm{N}(k_\mathrm{N}) \\ = \int \frac{\mathrm{d}^4k_\Lambda}{(2\pi)^4}\frac{\mathrm{d}^4k_\mathrm{N}}{(2\pi)^4}\frac{\mathrm{d}^4p}{(2\pi)^4}\int \mathrm{d}^4x\, \mathrm{e}^{-\mathrm{i}(p-k_\Lambda)\cdot x}\, \phi^*_\mathrm{K}(x)\int \mathrm{d}^4y\, \mathrm{e}^{\mathrm{i}(p-k_\mathrm{N})\cdot y}\, \phi_\pi(y) \\ \times \bar{\psi}_\Lambda(k_\Lambda)\Gamma_1\, \mathrm{i}\frac{\not{p}+m_\mathrm{R}}{p^2-m_\mathrm{R}^2+\mathrm{i}\epsilon}\Gamma_2\psi_\mathrm{N}(k_\mathrm{N})\ . \end{aligned} \tag{4.11}$$

In the pseudovector case, we have an additional derivative acting on the meson wave functions ϕ_K and ϕ_π. The matrix element in that case is given by

$$\begin{aligned}\mathcal{M} = \int \frac{\mathrm{d}^4k_\Lambda}{(2\pi)^4}\frac{\mathrm{d}^4k_\mathrm{N}}{(2\pi)^4}\frac{\mathrm{d}^4p}{(2\pi)^4}\int \mathrm{d}^4x\, \mathrm{e}^{-\mathrm{i}(p-k_\Lambda)\cdot x}\, \partial_\mu\phi^*_\mathrm{K}(x)\int \mathrm{d}^4y\, \mathrm{e}^{\mathrm{i}(p-k_\mathrm{N})\cdot y}\, \partial_\nu\phi_\pi(y) \\ \times \bar{\psi}_\Lambda(k_\Lambda)\Gamma_1^\mu\, \mathrm{i}\frac{\not{p}+m_\mathrm{R}}{p^2-m_\mathrm{R}^2+\mathrm{i}\epsilon}\Gamma_2^\nu\psi_\mathrm{N}(k_\mathrm{N})\ . \end{aligned} \tag{4.12}$$

Here we absorbed the additional γ^μ and γ^ν into the vertex factors Γ_1^μ and Γ_2^ν, respectively. Finally, for the spin-3/2 resonance, $\mathcal{M}$ is given by

$$\begin{aligned}\mathcal{M} = \int \frac{\mathrm{d}^4k_\Lambda}{(2\pi)^4}\frac{\mathrm{d}^4k_\mathrm{N}}{(2\pi)^4}\frac{\mathrm{d}^4p}{(2\pi)^4}\int \mathrm{d}^4x\, \mathrm{e}^{-\mathrm{i}(p-k_\Lambda)\cdot x}\, \partial_\mu\phi^*_\mathrm{K}(x)\int \mathrm{d}^4y\, \mathrm{e}^{\mathrm{i}(p-k_\mathrm{N})\cdot y}\, \partial_\nu\phi_\pi(y) \\ \times \bar{\psi}_\Lambda(k_\Lambda)\widetilde{\Gamma}_1\, \mathrm{i}\frac{\not{p}+m_\mathrm{R}}{p^2-m_\mathrm{R}^2+\mathrm{i}\epsilon}P^{\mu\nu}\widetilde{\Gamma}_2\psi_\mathrm{N}(k_\mathrm{N})\ , \end{aligned} \tag{4.13}$$

with the vertex factors $\widetilde{\Gamma}_1$ and $\widetilde{\Gamma}_2$ to distinguish them from Γ_1 and Γ_2 in (4.11).

The integration over x and y in (4.11) can be carried out, yielding the Fourier transforms of the meson wave functions, $\widehat{\phi}^*_\mathrm{K}(p-k_\Lambda)$ and $\widehat{\phi}_\pi(p-k_\mathrm{N})$, respectively. When the pseudovector Lagrangians are used (as in (4.12)), and in the case of the spin-3/2 resonance (4.13), the derivatives of the kaon and pion wave function give rise to additional factors $\mathrm{i}(p-k_\Lambda)_\mu$ and $-\mathrm{i}(p-k_\mathrm{N})_\nu$, respectively. We can then evaluate the matrix elements (4.11)–(4.13) in momentum space, this procedure and the use of various approximations for the meson wave functions are detailed in section 5.6

5 Initial and final state interactions

For a fully dynamical description of the production of hypernuclei, we now consider the interactions of the incoming and outgoing particles with the nucleus. In the literature, there are several models to describe the interaction of the meson with the (hyper)nucleus. A conceptual attractive approach, which is also in agreement with our formulation of the production process (see chapter 3), is to start from a Lagrange density including all the mesons, nucleons, and if necessary hyperons, and to solve the resulting equations of motion self-consistently.

To simplify actual calculations, the most commonly used models [98–100] introduce an effective *optical potential* instead of using the self-consistently calculated self-energies. This optical potential describes the short-range interactions in the medium, in addition to the long-range Coulomb force. Thereby, the potential parameters are fitted in such a way that they describe meson-nucleus scattering data. We present further particulars about the construction of the optical potential section 5.2.

The solutions of the equations of motion, with or without an additional potential, are the meson wave functions in coordinate space. Since our calculations are carried out in momentum space, we have to Fourier transform these solutions. This has its own caveats and we deal with them in section 5.5.

5.1 Self-energies and distorted waves

The Lagrangian of a meson moving freely in space-time is the one for a non-interacting scalar field [62, 63]

$$\mathcal{L}_{\mathrm{M}}^{\mathrm{free}} = \frac{1}{2}\partial_\mu\phi\partial^\mu\phi - \frac{m^2}{2}\phi^2 \,.$$

The equation of motion (Euler–Lagrange equation) is the Klein–Gordon equation and it reads

$$(\Box + m^2)\phi(x) = 0 \,. \tag{5.1}$$

Its solutions $\phi(x)$ are the free meson wave functions. They are given by linear combinations of plane waves in $3+1$ dimensions

$$\phi(x) = A\,\mathrm{e}^{-\mathrm{i}k\,\cdot\,x} + B\,\mathrm{e}^{\mathrm{i}k\,\cdot\,x} \,, \tag{5.2}$$

where the components of the momentum four-vector $k = (E, \boldsymbol{k})$ satisfy the on-shell condition

$$E^2 = k_0^2 = |\boldsymbol{k}|^2 + m^2 \ .$$

Since for scattering processes we are only interested in stationary solutions, the time-dependence of the wave function can be separated from the space-like part as $\phi(x) = \phi(\boldsymbol{x}, t)$ [62], and (5.2) can then be written as

$$\phi(\boldsymbol{x}, t) = A\,\mathrm{e}^{-\mathrm{i}Et}\,\mathrm{e}^{\mathrm{i}\boldsymbol{k}\,\cdot\,\boldsymbol{x}} + B\,\mathrm{e}^{\mathrm{i}Et}\,\mathrm{e}^{-\mathrm{i}\boldsymbol{k}\,\cdot\,\boldsymbol{x}} \ . \tag{5.3}$$

A and B are the normalisation constants, and taking only the "forward" moving part of (5.3) for an incoming particle, we set $B = 0$ and get $\phi(\boldsymbol{x}, t) = A\,\mathrm{e}^{-\mathrm{i}Et}\,\phi(\boldsymbol{x})$.

The non-relativistic case is discussed at great length for example in [70] and our case is completely analogous, keeping in mind that the relativistic energy-momentum relation is $E^2 = |\boldsymbol{k}|^2 + m^2$ $(= \omega^2(\boldsymbol{k}))$ instead of the non-relativistic one $E = |\boldsymbol{k}|^2/2m$. Otherwise, the space-like part of the solution of the free equations of motion are in both cases given by three-dimensional plane waves $\phi(\boldsymbol{x}) \sim \mathrm{e}^{\mathrm{i}\boldsymbol{k}\,\cdot\,\boldsymbol{x}}$.

When the meson is moving in a nuclear medium such as a nucleus, the equation of motion gets modified and the solutions are no longer given by plane waves. It can be shown that this change is equal to the introduction of an additional potential into the Klein–Gordon equation (5.1)

$$\Big(\Box + m^2 + V(x)\Big)\,\phi(x) = 0 \ . \tag{5.4}$$

The respective solutions $\phi(x)$ are called *distorted waves* and we will go into the details of how to obtain a realistic potential $V(x)$ for our purpose in the next section.

5.2 The optical potential

The potential term in (5.4) includes the combined effects of the interactions of the meson with the surrounding medium. A method to relate the scattering into open and closed channels to an effective potential was introduced by Feshbach [101, 102] and was already applied to various scattering problems, for example to meson-nucleus scattering [103]. In higher energetic reactions this naming is not appropriate, and we will refer to them as the explicit and background channels, respectively. The general idea is to split the available state space of the reaction into states considered explicitly (denoted by $\mathcal{P}$ below) and states that contribute indirectly to the reaction background (denoted by $\mathcal{Q}$). In a mathematical language this is equal to the (orthogonal) decomposition of the Hilbert space $\mathcal{H}$ into two subspaces:

$$\mathcal{H} = \mathcal{P} \oplus \mathcal{Q} \ .$$

For meson-nucleus scattering [103], the explicit channels $\mathcal{P}$ are given by those states that contain one or no meson in the final state, which are related to elastic

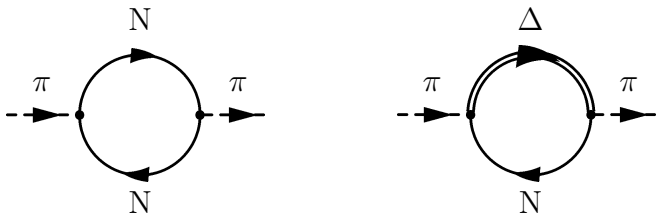

Figure 5.1: Nucleon-hole contribution (a) andΔ-hole contribution (b) to the pion self-energy.

scattering and absorption, respectively. The background channels $\mathcal{Q}$ are thereby given by all other states, for example states with more than one meson or with additional nucleons in the final state, or any kind of inelastic excitations. The equations of motion for the states of $\mathcal{P}$ and $\mathcal{Q}$ then decouple from each other and the transition matrix element for the process in question can be written as the expectation value of an effective potential [101, 102].

This, in turn, is related to the relativistic self-energy, which is calculated in the framework of multi-channel scattering theory. For the pion for example, this amounts to first order to summing up diagrams involving nucleon-hole and Δ-hole loops as shown in figure 5.1 [100, 104, 105]. The self-energy of the kaon is calculated in the same way, except that there are no suitable resonances that play the role of the Δ as in the pion case. Therefore, the main contribution in this case comes from the nucleon-hole loops 5.1a.

The resulting self-energy $\Pi(k)$ modifies the propagator as

$$\mathcal{D}_\pi = \frac{1}{k^2 - m^2 - \Pi(k)} \ . \tag{5.5}$$

On the other hand, the change in momentum of the meson in the medium with respect to the free momentum k_0 is given by, up to first order in the optical potential V,

$$k_0^2 - k^2 = 2EV \ .$$

The pion self-energy Π in (5.5) can be identified with this change, and it is therefore plausible to identify [104]

$$\Pi(k) = 2EV(k) \ .$$

Another starting point is the relativistic energy relation from the Klein–Gordon equation, minimally coupled to the electromagnetic potential,

$$(E - e\phi)^2 - (\boldsymbol{p} - e\boldsymbol{A})^2 = m^2 \ . \tag{5.6}$$

We then take the electromagnetic interaction to be purely electrostatic, $\boldsymbol{A} = 0$ (Coulomb gauge), where the scalar potential $\phi(\boldsymbol{x})$ is given by the charge distribution of the nucleus. To incorporate the additional strong interactions between the

mesons and the nucleus, we have to respect the Lorentz structure of (5.6). It is commonly assumed that the optical potential transforms like the zeroth component of a four-vector [81]. It is then included in the energy term together with the Coulomb potential by the substitution

$$E \mapsto E - V_{\text{coul}} - V_{\text{opt}} \ ,$$

where we set $V_{\text{coul}} := e\phi$. The square of this term, which appears in (5.6), is then given by

$$\begin{aligned} E^2 \mapsto (E - V_{\text{coul}} - V_{\text{opt}})^2 &= (E - V_{\text{coul}})^2 - 2\,(E - V_{\text{coul}})\,V_{\text{opt}} + V_{\text{opt}}^2 \\ &\approx (E - V_{\text{coul}})^2 - 2EV_{\text{opt}} \ , \end{aligned} \tag{5.7}$$

where the term quadratic in the optical potential and the term $V_{\text{coul}}V_{\text{opt}}$ are usually neglected and we are left with (5.7). The Klein–Gordon equation with these potentials reads

$$\left(-\triangle + m^2 + 2EV_{\text{opt}}\right)\phi = (E - V_{\text{coul}})^2\,\phi \ .$$

While the Coulomb interaction is well understood, the short-range nuclear interactions are more difficult to model, and we present some details of their description below. The point is, as in the nucleon case, to use the method outlined above to fit the parameters of a convenient parametrisation of the potential for the numerical calculations.

5.2.1 Low energy mesons

Models for low energy pions, that is of energies from 10 MeV to a few 100 MeV, and their interactions with nuclei have a long history. Their scattering on light nuclei was studied for example by Kisslinger [98] and was then together with Tabakin [99] refined, already more than 30 years ago. Computer programs for the scattering of pions from nuclei were also developed by Eisenstein and others [106–108].

The connection to the self-energies is established by calculating the scattering amplitudes and solving the Schwinger–Dyson equation for the propagator. For low energy pions, this was done for example in [100], where the general form is taken to be

$$V_{\text{opt}}(\boldsymbol{x}) = V_1^{(s)}(\boldsymbol{x}) + V_2^{(s)}(\boldsymbol{x}) + \delta V_3^{(s)}(\boldsymbol{x}) + V_{\text{opt}}^{(p)}(\boldsymbol{x}) \ .$$

The superscripts (s) and (p) denote the s-wave [109] and p-wave parts, respectively.

Relating the optical potential to the nuclear density ϱ, Kisslinger suggested the following parametrisation [99]

$$2EV_{\text{opt}} = a_1\varrho + a_2\boldsymbol{\nabla}\varrho\cdot\boldsymbol{\nabla} + a_3\triangle\varrho + a_4\triangle^2\varrho \ , \tag{5.8}$$

where a_1, a_2, a_3, and a_4 are the parameters which are in general momentum dependent complex functions.

5.2.2 High energy mesons

In the case of kaons, the complexity of the optical potential is reduced, and even more so if the incident momentum is high enough to neglect parts of the parametrisation (5.8). Thus, for higher energies of the meson, a simpler form of the optical potential proved to be sufficient [98, 110]:

$$2EV_{\mathrm{opt}}(r) = -Ak^2 b_0 \varrho(r) + Ab_1 \boldsymbol{\nabla}\varrho(r) \cdot \boldsymbol{\nabla} \ , \tag{5.9}$$

with a reduced number of parameters, which are fit to the experimental kaon-nucleus elastic scattering cross sections. Kohno et al. in [111] set $b_1 = 0$, hence keeping only the first term in (5.9) for kaon momenta $\sim 600 \ldots 800$ MeV in the laboratory frame. The only complex parameter left is then b_0, and the density of the nucleus is taken from nuclear models, for example as described in section 2.3. We are left with

$$2EV_{\mathrm{opt}}(r) = -b_0 k^2 \varrho(r) \ , \tag{5.10}$$

which is additionally motivated by the $t\varrho$-approximation, and which will be discussed in section 5.4. This optical potential works well for high energetic pions too, for incident energies of a few 100 MeV to a few GeV. In this case, b_0 can be taken to be purely imaginary and can be related to the total free-space elementary scattering cross section by setting $b_0 \sim \mathrm{i}\sigma_{\mathrm{tot}}/k$.

5.3 Numerical solutions of the Klein–Gordon equation

For spherical symmetric potentials it is convenient to expand the wave function into partial waves [70]

$$\phi(\boldsymbol{x}) = \sum_{\ell=0}^{\infty} \sum_{m=-\ell}^{\ell} c_{\ell m} R_{\ell m}(r) Y_{\ell m}(\hat{x}) \ . \tag{5.11}$$

In the case of plane waves for free particles (5.3), the radial functions are given by the regular spherical Bessel functions of the first kind, $R_\ell(r) = j_\ell(kr)$, which follows from the expansion (2.12).

Using (5.11), the modified Klein–Gordon equation (or Schrödinger equation in the case of non-relativistic particles) separates into a radial and an angular part. Its solution can be obtained by applying a standard numerical integration routine for the resulting differential equation for $u_\ell(r) := rR_\ell(r)$. For the actual evaluation, we use a program based on the usual Runge–Kutta method.

5.3.1 Distorted waves in a Coulomb potential

In the case of a Coulomb potential, the solution of (5.4), exploiting the spherical symmetry of the potential [70], is given by

$$\phi(\boldsymbol{x}) = \frac{1}{kr}\sum_{\ell=0}^{\infty}(2\ell+1)\mathrm{i}^{\ell}\,\mathrm{e}^{\mathrm{i}\sigma_\ell}\,F_\ell(k,r)P_\ell(\cos\theta)\;.$$

The $F_\ell(k,r)$ are the regular spherical Coulomb functions [112]

$$F_\ell(k,r) = C_\ell\,\mathrm{e}^{\mathrm{i}kr}(kr)^{\ell+1}\,{}_1F_1(\ell+1+\mathrm{i}\gamma;2(\ell+1);-2\mathrm{i}kr)$$

with the hypergeometric function ${}_1F_1$. The coefficients C_ℓ are given by

$$C_\ell = \frac{2^\ell\,\mathrm{e}^{-\frac{1}{2}\pi\gamma}|\Gamma(\ell+1+\mathrm{i}\gamma)|}{(2\ell+1)!}\;,$$

where $\gamma = mZ_1Z_2e^2/\hbar^2k$ is the *Sommerfeld*-parameter and $\sigma_\ell = \arg\Gamma(\ell+1+\mathrm{i}\gamma)$ are the Coulomb phase shifts.

Using the irregular Coulomb functions and the resulting $H_\ell^{(\pm)}$ as described in [70], the scattering wave function can be expanded as

$$\phi(\boldsymbol{x}) = \frac{1}{2kr}\sum_{\ell=0}^{\infty}(2\ell+1)\mathrm{i}^{\ell}\left[H_\ell^{(-)}(k,r) + \mathrm{e}^{2\mathrm{i}\sigma_\ell}\,H_\ell^{(+)}(k,r)\right]P_\ell(\cos\theta)\;.$$

In the case of an additional short-range potential one gets an additional phase shift δ_ℓ, and the overall wave function is given by

$$\phi(\boldsymbol{x}) = \frac{1}{2kr}\sum_{\ell=0}^{\infty}(2\ell+1)\mathrm{i}^{\ell}\left[H_\ell^{(-)}(k,r) + \mathrm{e}^{2\mathrm{i}(\sigma_\ell+\delta_\ell)}\,H_\ell^{(+)}(k,r)\right]P_\ell(\cos\theta)\;. \tag{5.12}$$

Using the addition theorem for the spherical harmonics,

$$(2\ell+1)P_\ell(\cos\theta) = 4\pi\sum_{m=-\ell}^{\ell}Y_{\ell m}^*(\hat{k})Y_{\ell m}(\hat{r})\;, \tag{5.13}$$

we can write (5.12) for arbitrary choices of the z-direction as

$$\phi(\boldsymbol{x}) = 4\pi\frac{1}{2kr}\sum_{\ell=0}^{\infty}\sum_{m=-\ell}^{\ell}\mathrm{i}^{\ell}\left[H_\ell^{(-)}(k,r) + \mathrm{e}^{2\mathrm{i}(\sigma_\ell+\delta_\ell)}\,H_\ell^{(+)}(k,r)\right]Y_{\ell m}^*(\hat{k})Y_{\ell m}(\hat{r})\;, \tag{5.14}$$

and from a comparison with (5.11) we can read off $c_{\ell m}$ and $R_{\ell m}$

$$\begin{aligned} c_{\ell m} &= 4\pi\mathrm{i}^{\ell}Y_{\ell m}^*(\hat{k})\;,\\ R_{\ell m}(k,r) &= \frac{1}{2kr}\left[H_\ell^{(-)}(k,r) + \mathrm{e}^{2\mathrm{i}(\sigma_\ell+\delta_\ell)}\,H_\ell^{(+)}(k,r)\right]\;. \end{aligned} \tag{5.15}$$

Note that the irregular Coulomb functions $H_\ell^{(\pm)}(k,r)$ in (5.15) have the asymptotic behaviour

$$H_\ell^{(\pm)}(k,r) \to \mp\mathrm{i}\exp\left\{\pm\mathrm{i}(kr - \ell\pi/2 - \gamma\log(2kr))\right\} \quad \text{for} \quad kr \gg \ell\;,$$

such that $R_{\ell m}$ (5.15) approach spherical waves for large values of r.

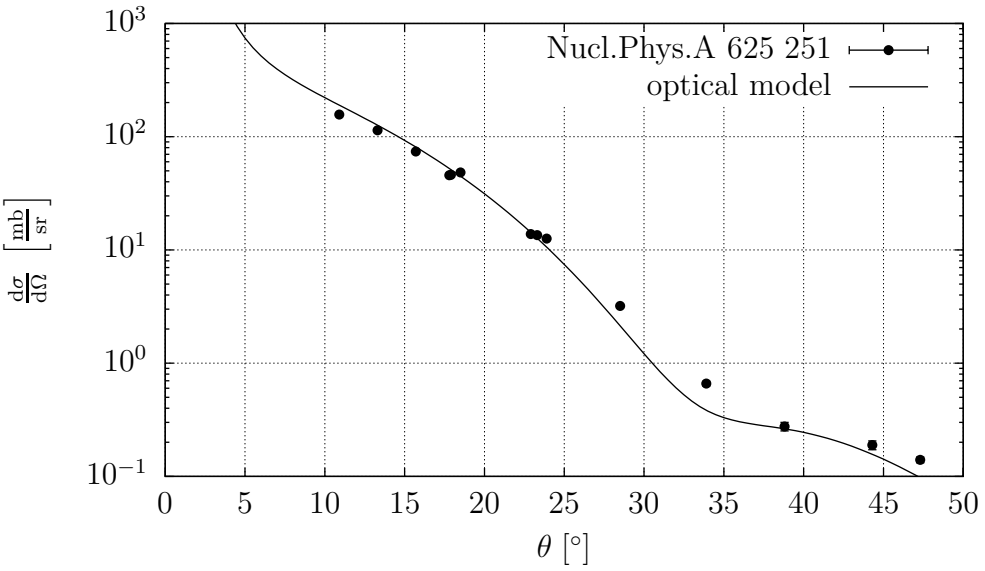

Figure 5.2: Differential cross section for K^+ elastic scattering on ^{12}C at $p_{lab} = 635$ MeV. Shown is the calculation using the optical potential (5.10) with the parameter $b_0 = -0.5937 + i\,0.4417$ fm^3. The experimental data are taken from [113].

5.3.2 Kaon elastic scattering

To verify the validity of the simple optical potential (5.10) for elastic scattering of K^+ on ^{12}C, we compare the cross sections obtained from the solution of the Klein–Gordon equation to experimental data at different energies. Figures 5.2, 5.3, and 5.4 show such comparisons with experimental data [113–115] for kaon momenta (in the laboratory frame) of $p_{lab} = 635$ MeV, 715 MeV, and 800 MeV, respectively.

The potential parameters used for the calculations are summarised in table 5.1, and the nuclear matter density is parametrised according to the results from our nuclear model presented in section 2.4. More details about this parametrisation can be found in the next section. We see that the simple optical potential (5.10) fits the data at these energies quite well, although not perfectly.

In the case of pion-induced production of the hypernucleus $^{12}_{\Lambda}C$ with a pion laboratory momentum of 1050 MeV [42], the outgoing kaon has a momentum of $p_{lab} = 691.7$ MeV, which lies in the range examined in [113]. It was shown above that we can reproduce the respective cross sections quite well within the optical model approach. Since there are no elastic scattering data available to fit the optical potential parameters to, we interpolate between the parameters in table 5.1. A quadratic fit to the data points in this table gives $b_0(691.7\text{ MeV}) = -0.3862 + i\,0.4057$ fm^3.

The kaon wave function is calculated by solving the Klein–Gordon equation in coordinate space with a standard Runge–Kutta method [106]. The resulting radial functions for a selected number of ℓ's are shown in figure 5.5. We see that only for

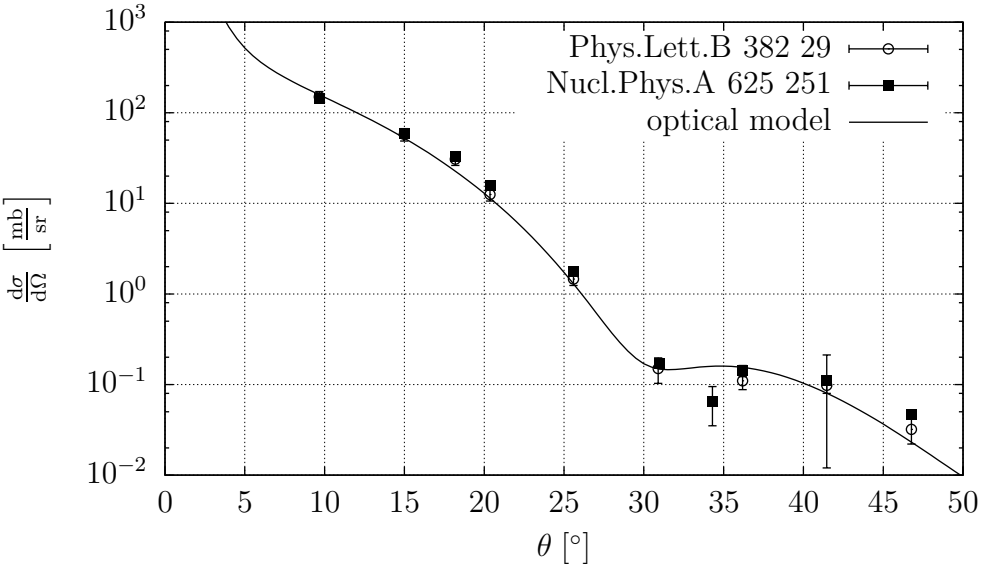

Figure 5.3: Differential cross section for K^+ elastic scattering on ^{12}C at $p_{lab} = 715$ MeV. The calculation was done with the optical potential parameter $b_0 = -0.3433 + i\,0.3923$ fm^3. The experimental data are taken from [113, 114].

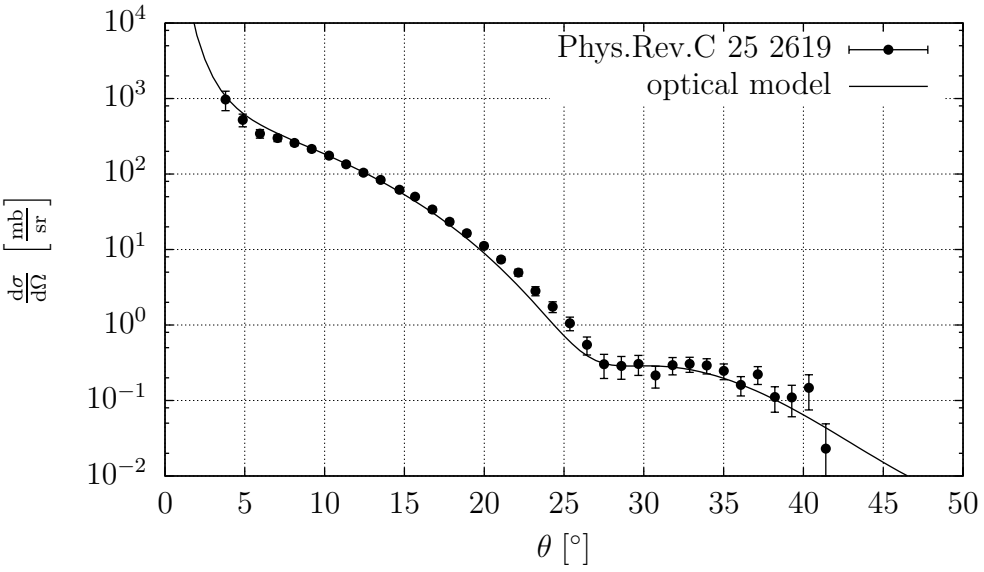

Figure 5.4: Differential cross section for K^+ elastic scattering on ^{12}C at $p_{lab} = 800$ MeV. Shown is the calculations using the optical potential with the parameter $b_0 = -0.3960 + i\,0.3506$ fm^3. The experimental data are taken from [115].

p_{lab} [MeV]	$\Re\, b_0$ [fm^3]	$\Im\, b_0$ [fm^3]
635	−0.5937	0.4417
715	−0.3433	0.3923
800	−0.396	0.3506
692	−0.3862	0.4057

Table 5.1: The optical potential parameters used for the calculation of the elastic scattering cross sections of K^+ on ^{12}C.

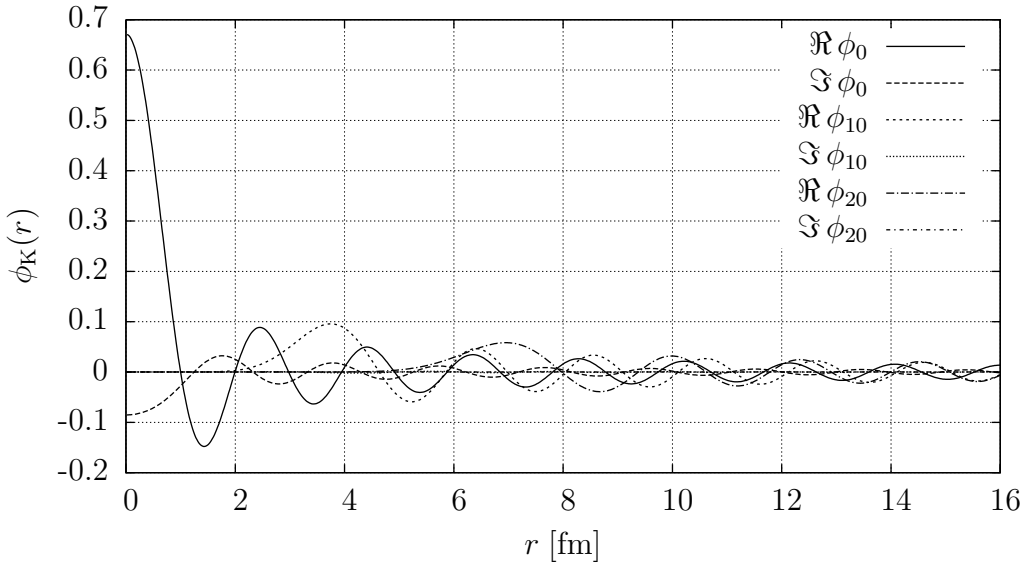

Figure 5.5: K^+ wave function in ^{12}C at $p_{\mathrm{lab}} = 691.7$ MeV for $\ell \in \{0, 10, 20\}$.

$\ell = 0$ the wave function does not vanish at $r = 0$, as it is expected. Furthermore, the first maximum of the real part of the wave function shifts to larger distances as ℓ gets larger and the imaginary part gets negligibly small. It resembles the free particle case where the radial part of the wave function is given by the spherical Bessel function $j_\ell(r)$. The asymptotic behaviour of the wave function is shown in figure 5.6, where the magnitude approaches unity at very large distances.

The same parametrisation (5.10) works also well for high energetic pions. For elastic scattering on ^{12}C at $p_{\mathrm{lab}} = 800$ MeV, we use $b_0 = -0.16 + \mathrm{i}\,0.90$ fm^3. The respective cross sections for π^+ and π^- compared to experimental data are shown in figure 5.7.

5.4 The eikonal approximation

At higher energies, the full solution of the Klein–Gordon equation with an optical potential might not be necessary and becomes also involved. One reason for this is

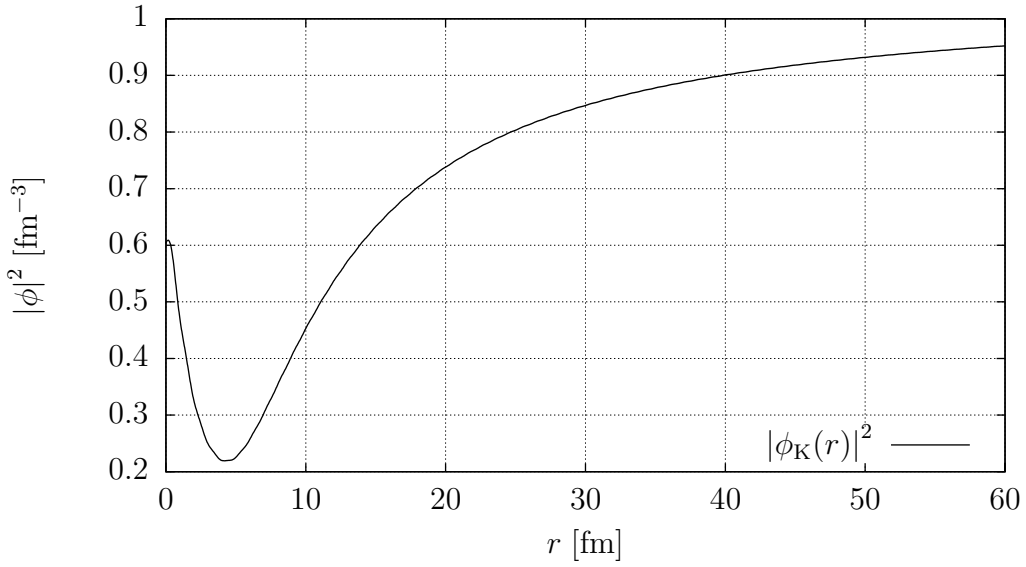

Figure 5.6: The magnitude of the K^+ wave function in ^{12}C at $p_{\mathrm{lab}} = 691.7$ MeV as a function of the radial distance r.

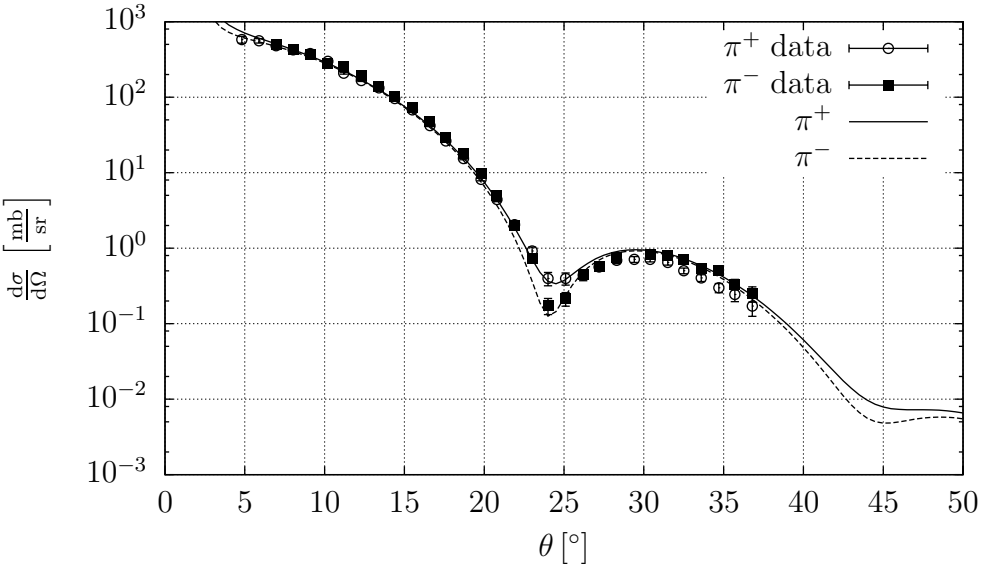

Figure 5.7: Differential cross section for π^+ and π^- elastic scattering on ^{12}C at $p_{\mathrm{lab}} = 800$ MeV. Shown are the calculations using the solution of the Klein–Gordon equation with an optical potential, with the only parameter $b_0 = -0.16 + \mathrm{i}\,0.90$ fm^3. The experimental data are taken from [116].

the partial wave expansion, which is only exact if one sums the terms for all ℓ up to infinity. Since this is beyond computational power, we have to stop at a certain (high) value and the rule of thumb is to expand at least up to $\ell_{\max} \sim k r_{\max}$, where $r_{\max}$ is of the order of a few times the nuclear radius R_A. Therefore, $\ell_{\max}$ increases with increasing incoming pion momentum and with it the numerical complexity.

Semi-classical approximations are often used and the eikonal approximation [70, 117] proved to be quite successful for the description of high energy scattering of pions on nuclei [118, 119]. It is inspired by ray optics and is similar to the WKB approximation in quantum mechanics. The wave function in the eikonal approximation is obtained by a modification of the plane wave which is given by a straight-line integral of the optical potential up to the respective point. The wave function in this approximation is given by (see for example [70])

$$\phi(\boldsymbol{x}) = \exp\left\{ \mathrm{i}\boldsymbol{k}\cdot\boldsymbol{x} - \frac{\mathrm{i}}{v}\int\limits_{-\infty}^{z} V(\boldsymbol{b}, z')\,\mathrm{d}z' \right\} , \tag{5.16}$$

where $\boldsymbol{k}$ is the incident (asymptotic) momentum of the particle, $v = |\boldsymbol{k}|/m$ is the magnitude of the incident velocity, and $\boldsymbol{b}$ is the (two-dimensional) impact vector in cylindrical coordinates. The optical potential is, in general, a complex function $V = U - \mathrm{i}W$ which results in an additional phase factor from the real part U and an amplitude reduction from the imaginary part W.

5.4.1 The tϱ-approximation for the optical potential

However, we still need a potential to describe the in-medium interactions of the meson. But since at higher energies several effects are suppressed, a simple form can be used, instead of the full self-consistent evaluation of the self-energy. For example the $t\varrho$-approximation simply relates the potential to the free-space single-particle scattering amplitudes (or to the total cross section as indicated in (5.10)) and the density. The optical potential in this case is given by

$$\begin{aligned} V_\mathrm{opt}(\boldsymbol{x}) &= -\frac{4\pi}{2E_\mathrm{lab}}\left[f_\mathrm{mp}\varrho_\mathrm{p}(\boldsymbol{x}) + f_\mathrm{mn}\varrho_\mathrm{n}(\boldsymbol{x}) \right] \\ &= -\frac{k}{2E_\mathrm{lab}}\left[\mathrm{i}\sigma_\mathrm{mp}^\mathrm{tot}(1-\mathrm{i}\gamma_\mathrm{mp})\frac{Z}{A} + \mathrm{i}\sigma_\mathrm{mn}^\mathrm{tot}(1-\mathrm{i}\gamma_\mathrm{mn})\frac{N}{A} \right] \varrho(\boldsymbol{x}) , \end{aligned} \tag{5.17}$$

where f_mp and f_mn are the elementary free-space meson-proton and meson-neutron scattering amplitudes, respectively. Applying the optical theorem, they can be substituted by the total cross sections $\sigma_\mathrm{mp}^\mathrm{tot}$ and $\sigma_\mathrm{mn}^\mathrm{tot}$, leading to the second line in (5.17). The respective ratios of the real to the imaginary part of the scattering amplitudes are denoted by $\gamma_\mathrm{mp} := \Im f_\mathrm{mp}/\Re f_\mathrm{mp}$ and $\gamma_\mathrm{mn} := \Im f_\mathrm{mn}/\Re f_\mathrm{mn}$. We have also separated the neutron and proton contributions to the potential, whereby Z is the proton number, N is the neutron number, and A is the total number of nucleons.

For spherically symmetric nuclei the density, and hence the potential, depends only on the magnitude of $\boldsymbol{x}$, $|\boldsymbol{x}| =: r$. In these cases we can integrate (5.16) by rewriting the argument of the potential as

$$V(r) = V(\boldsymbol{b}, z) = V\left(\sqrt{|\boldsymbol{b}|^2 + z^2}\right) .$$

The density $\varrho(r)$ is specific to each nucleus and can, in principle, be calculated from the nuclear wave functions as described in section 2.4, in particular by (2.11). Here, however, we approximate the density by relatively simple parametrisations which are easier and faster to compute numerically. For light nuclei, that is for $A \leq 16$, a modified Gaussian shape

$$\varrho_{\mathrm{G}}(r) = \frac{1}{(\sqrt{\pi} R_{\mathrm{G}})^3} \left[4 + \frac{2(A-4)}{3} \frac{r^2}{R_{\mathrm{G}}^2}\right] \mathrm{e}^{-\frac{r^2}{R_{\mathrm{G}}^2}}$$

with the radial parameter R_{G} works well. For heavier nuclei, $A > 16$, a Woods–Saxon shaped density

$$\varrho_{\mathrm{WS}}(r) = \frac{\varrho_0}{1 + \exp\left\{\frac{r-R}{a}\right\}} \tag{5.18}$$

with the radial parameter R and an additional *diffuseness* parameter a is more appropriate. The densities are normalised to the total nucleon number, such that

$$\int_{\mathbb{R}^3} \varrho(\boldsymbol{x}) \, \mathrm{d}^3 x = A ,$$

which is already fulfilled in the Gaussian case. In the Woods–Saxon case this determines ϱ_0, which is given by [120, 121]

$$\varrho_0 = \frac{3A}{4\pi R^3} \frac{1}{1 + (\frac{\pi a}{R})^2} .$$

In the Woods–Saxon case, the radius parameter R can be approximated by

$$R = 1.28 A^{1/3} - 0.76 + 0.8 A^{-1/3} .$$

We fit the parameters R_{G}, R and a to the radial densities given by (2.11). The fitted values for both density approximations for ^{12}C and ^{40}Ca are given in table 5.2, and the resulting densities are shown in figure 5.8 for ^{12}C and in figure 5.9 for ^{40}Ca. It can be seen, that for the light nucleus both parametrisations work quite well, whereas for the heavier nucleus the Gaussian density profile is not usable. In that case it is better to use the Woods–Saxon form (5.18).

5.4.2 The Coulomb potential

In addition to the optical potential from the strong interactions, we have to account for the Coulomb interaction, by separating the far-field region from the near-field

	A	Z	Woods–Saxon		Gauss
			R [fm]	a [fm]	R_{G} [fm]
^{12}C	12	6	2.24	0.46	1.6
^{40}Ca	40	20	3.49	0.547	2.08

Table 5.2: Density parameters for the eikonal approximation for ^{12}C and ^{40}Ca, fitted to the nucleon wave functions and the elastic scattering cross sections.

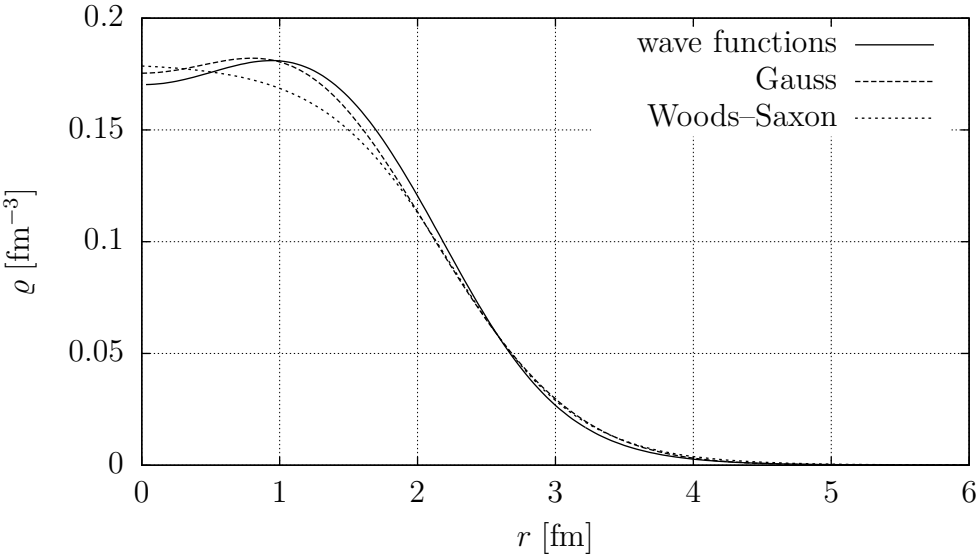

Figure 5.8: The nuclear densities for ^{12}C given by the parametrisations in the text fitted to the densities as calculated from the bound states.

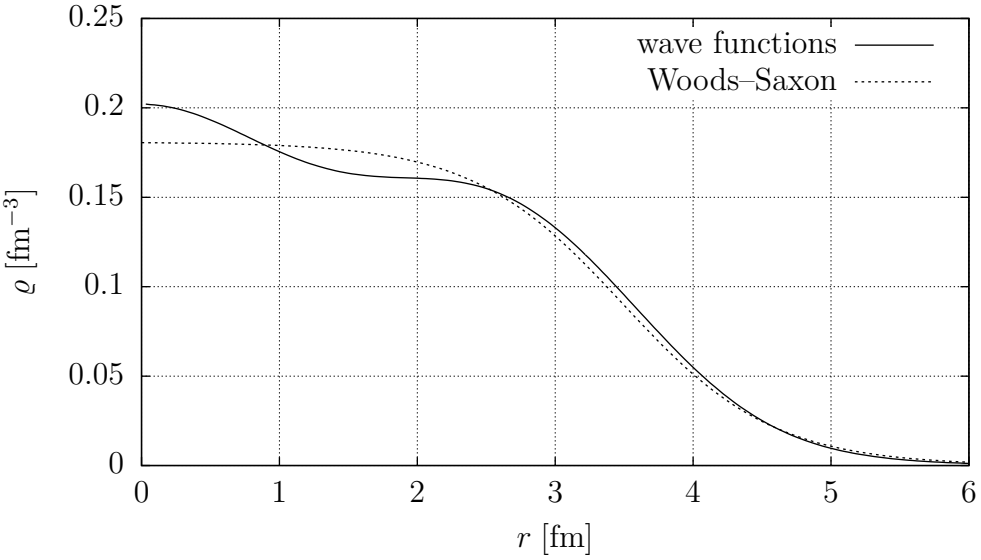

Figure 5.9: The nuclear densities of ^{40}Ca given by the parametrisations in the text and the calculation from the radial parts of the bound state wave function.

in the nucleus. Inside the nucleus, the Coulomb potential comes from the actual charge distribution, whereas outside it is given by the potential of a point-charge with the electric charge Ze. We split the Coulomb part as follows:

$$V_{\text{coul}}^{\text{eff}} = \left(V_{\text{coul}}^{\text{eff}} - V_{\text{coul}}^{\text{pt}}\right) + V_{\text{coul}}^{\text{pt}} \,,$$

where the part in parentheses is the one that vanishes outside the nucleus. This term therefore has about the same range as the optical potential V_{opt} and we add it to the potential as $V_{\text{coul}} := V_{\text{coul}}^{\text{eff}} - V_{\text{coul}}^{\text{pt}}$ for the calculation of the eikonal wave function (5.16).

Both, the optical potential V_{opt} and the Coulomb potential V_{coul} inside the nucleus, give rise to the eikonal phase shift to the plane wave as indicated by (5.16). Outside the nucleus, we only have to deal with the Coulomb potential of a point-charge, which gives the standard Coulomb phase shift to the wave function.

5.4.3 Comparison to elastic scattering data

To verify the validity of the eikonal approximation, and to fix the parameters used for the calculation of the meson wave function, we compare again the calculated differential elastic scattering cross section to data. We start the comparison with the elastic scattering of π^- on ^{12}C at momenta where experimental data is available. The cross sections for $p_{\text{lab}} = 800\,\text{MeV}$ are shown in figure 5.10. Both density distributions are used for the calculations in the eikonal approximation and describe

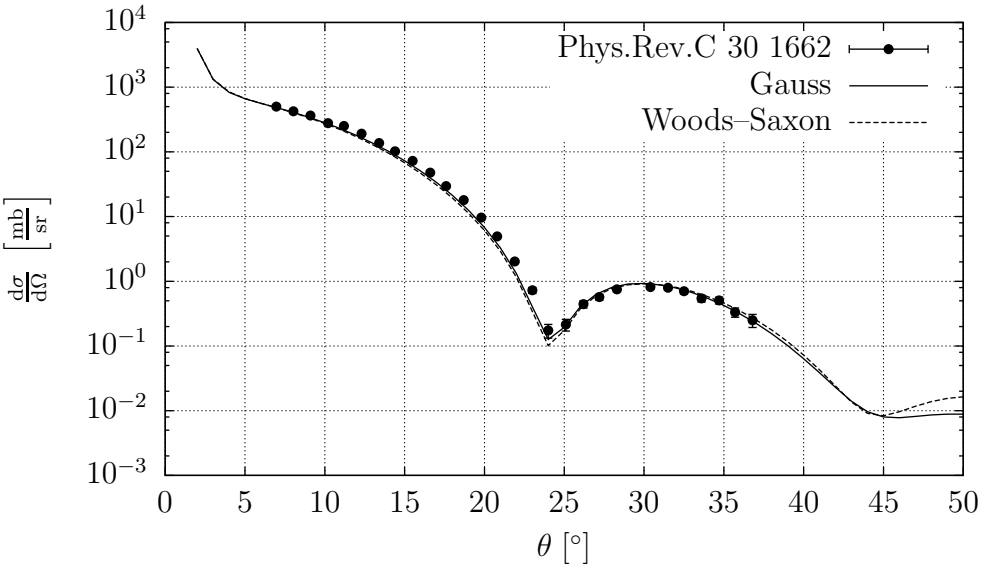

Figure 5.10: Differential cross section for π^--elastic scattering on ^{12}C at p_{lab} = 800 MeV. Shown are the calculations in the eikonal approximation using the Gaussian density distribution (solid line) and the Woods–Saxon parametrisation (dashed line). The experimental data are taken from [116].

the data equally well. They deviate only at large scattering angles, where no data is available.

In figure 5.11 we compare the differential cross section for π^+ on ^{12}C for p_{lab} = 800 MeV calculated by both methods, the solution of the Klein–Gordon equation and the eikonal approximation, against each other. Apart from small differences, the data are well described and it is feasible to use the eikonal approximation at these energies.

The absorption effect of the nuclear potential can be seen when looking at the magnitude of the wave function, in other words the envelope or modulation of the oscillating plane wave. This is related to the imaginary part of the optical potential via (5.16). It is furthermore related to the nuclear density by (5.17) and the projection onto the b-z-plane in figure 5.12 shows that the range of the absorption is indeed given by the size of the nucleus.

5.5 Fourier transformation

We need to Fourier transform the wave function from coordinate space to momentum space to use it for the scattering amplitude calculation as we indicated in section 4.3, in particular in (5.28), (5.27), and (5.29). The four-dimensional Fourier

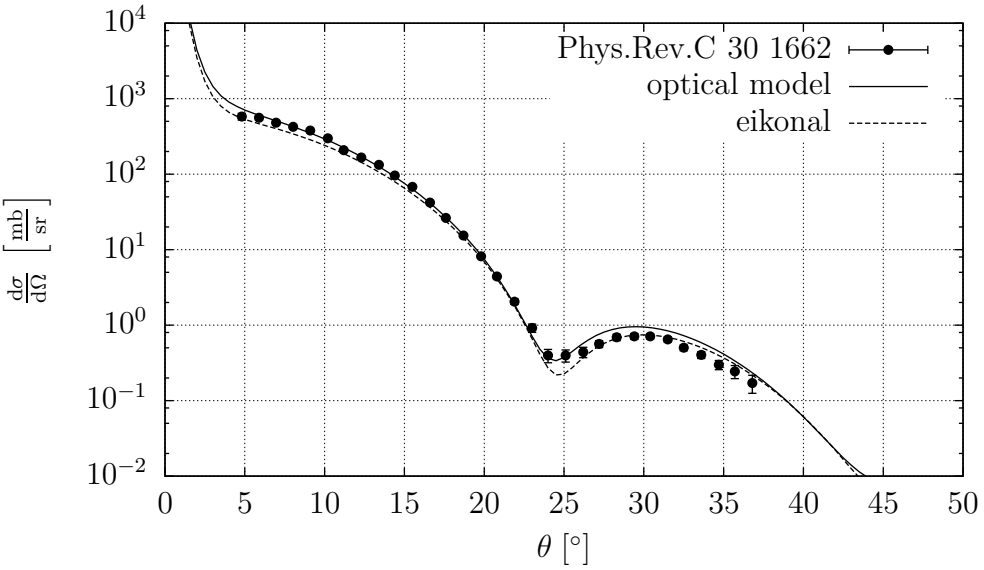

Figure 5.11: The differential cross section for π^+ on ^{12}C at $p_{lab} = 800$ MeV calculated by solving the Klein–Gordon equation with an optical potential (solid line) compared to the result using the eikonal approximation (dashed line). The experimental data are taken from [116].

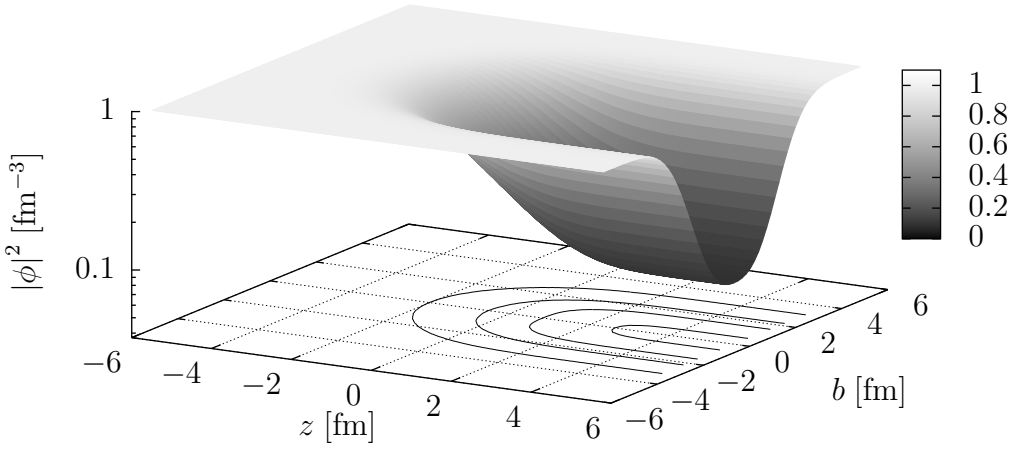

Figure 5.12: The magnitude of the π^+ eikonal wave function in ^{12}C for $p_{lab} = 1050$ MeV in the b-z-plane. The contour lines mainly indicate places of equal distortion, which approximately outline the size of the nucleus ($r \sim 2$ fm).

transformation is given by (see for example [62])

$$\widehat{\phi}(k) = \int\limits_{\mathbb{R}^4} \mathrm{e}^{\mathrm{i}k'\,\cdot\,x}\,\phi(x)\,\mathrm{d}^4x\ . \tag{5.19}$$

Separating the time-dependence from the coordinate space function $\phi(x)$ as in (5.3) gives $2\pi\delta(k'_0 - E)$ from the time-like part in (5.19) and we are left with the three-dimensional Fourier transformation of the space-like part $\phi(\boldsymbol{x})$ of the meson wave function

$$\widehat{\phi}(k') = 2\pi\delta(k'_0 - E)\int\limits_{\mathbb{R}^3} \mathrm{e}^{-\mathrm{i}\boldsymbol{k}'\,\cdot\,\boldsymbol{x}}\,\phi(\boldsymbol{x})\,\mathrm{d}^3x =: 2\pi\delta(k'_0 - E)\widehat{\phi}(\boldsymbol{k}')\ . \tag{5.20}$$

We evaluate (5.20) under the condition that $\phi(\boldsymbol{x})$ can be numerically computed up to a specific radius R, and is for larger radii given by an analytic expression, for example by (5.14). First, we split the three-dimensional integral (5.20) into a radial and an angular part, using again the expansion of the plane waves (2.12). $\widehat{\phi}(\boldsymbol{k}')$ is thereby given by

$$\begin{aligned}\widehat{\phi}(\boldsymbol{k}') = 4\pi\sum_{\ell=0}^{\infty}\sum_{m=-\ell}^{\ell}\sum_{\ell'=0}^{\infty}\sum_{m'=-\ell'}^{\ell'}(-\mathrm{i})^{\ell}\int\limits_0^{\infty} Y_{\ell m}(\hat{k}')j_\ell(k'r)c_{\ell' m'}R_{\ell' m'}(r)\,r^2\mathrm{d}r \\ \times\int\limits_{S^2} Y^*_{\ell m}(\hat{x})Y_{\ell' m'}(\hat{x})\,\mathrm{d}\Omega_x\ .\end{aligned} \tag{5.21}$$

Note that in (5.21), and in what follows, $k' := |\boldsymbol{k}'|$ must not be confused with the four-vector k' in (5.19). Due to the normalisation of the spherical harmonics $Y_{\ell m}$, the integral over $\mathrm{d}\Omega_x$ evaluates to Kronecker deltas,

$$\int\limits_{S^2} Y^*_{\ell m}(\hat{x})Y_{\ell' m'}(\hat{x})\,\mathrm{d}\Omega_x = \delta_{\ell'\ell}\delta_{m' m}\ ,$$

and therefore two of the sums in (5.21) vanish. We are left with only ℓ and m as summation indices and (5.21) reduces to

$$\widehat{\phi}(\boldsymbol{k}') = 4\pi\sum_{\ell=0}^{\infty}\sum_{m=-\ell}^{\ell}(-\mathrm{i})^{\ell}c_{\ell m}Y_{\ell m}(\hat{k}')\int\limits_0^{\infty} j_\ell(k'r)R_{\ell m}(r)\,r^2\mathrm{d}r\ . \tag{5.22}$$

The function $R_{\ell m}(r)$ is either analytically known, usually at large distances, or numerically calculated for short distances. Furthermore, $R_{\ell m}(r)$ does not depend on m and we will write $R_\ell(r)$ instead.

We define the radial integral in (5.22) as $\phi_\ell(k')$ by

$$\phi_\ell(k') := \int\limits_0^{\infty} j_\ell(k'r)R_\ell(r)\,r^2\mathrm{d}r = \int\limits_0^{R} j_\ell(k'r)R^{(1)}_\ell(r)\,r^2\mathrm{d}r + \int\limits_R^{\infty} j_\ell(k'r)R^{(2)}_\ell(r)\,r^2\mathrm{d}r\ .$$

Here, $R_\ell^{(1)}(r)$ is the numerically obtained radial part from integrating (5.4) and $R_\ell^{(2)}(r)$ is known for example from the expansion (5.15) and matched according to $R_\ell^{(1)}(R) = R_\ell^{(2)}(R)$. If the asymptotic functions $R_\ell^{(2)}(r)$ are given in terms of the Coulomb functions as in (5.15) we can evaluate the oscillatory integral in the complex plane as described in [122, 123].

We use again the addition theorem (5.13) and substitute the sum over the magnetic quantum numbers m of the spherical harmonics by a single Legendre polynomial of the angle γ between the asymptotic momentum $\boldsymbol{k}$ and the Fourier transformation evaluation point $\boldsymbol{k}'$. This angle is given by spherical addition theorem [70]

$$\cos\gamma = \cos\theta\cos\theta' + \sin\theta\sin\theta'\cos(\varphi - \varphi') \;,$$

where θ and θ' are the polar angles of $\boldsymbol{k}$ and $\boldsymbol{k}'$, respectively, and φ and φ' are the corresponding azimuthal angles.

Since the numerical solution is properly matched to the far-field solution, the constants $c_{\ell m}$ are the same in both regions and we obtain for the Fourier transformed wave function (5.22) the final expression

$$\begin{aligned}\widehat{\phi}(\boldsymbol{k}') &= 4\pi\sum_{\ell=0}^{\infty}(-\mathrm{i})^\ell 4\pi\mathrm{i}^\ell\frac{2\ell+1}{4\pi}P_\ell(\cos\gamma)\int_0^\infty j_\ell(k'r)R_\ell(r)\,r^2\mathrm{d}r \\ &= 4\pi\sum_{\ell=0}^{\infty}(2\ell+1)P_\ell(\cos\gamma)\phi_\ell(k') \;. \end{aligned} \tag{5.23}$$

5.5.1 Eikonal Fourier transformation

Using $U(\boldsymbol{x}) := 2mV(\boldsymbol{x})$, the Fourier transformation of the eikonal wave function (5.16) is given by

$$\begin{aligned}\widehat{\phi}(\boldsymbol{k}') &= \int_{\mathbb{R}^3}\mathrm{e}^{-\mathrm{i}\boldsymbol{k}'\cdot\boldsymbol{x}}\,\exp\left\{\mathrm{i}\boldsymbol{k}\cdot\boldsymbol{x} - \frac{\mathrm{i}}{2k}\int_{-\infty}^{z}U(\boldsymbol{b},z')\,\mathrm{d}z'\right\}\mathrm{d}^3x \\ &= \int_{\mathbb{R}^3}\mathrm{e}^{\mathrm{i}\boldsymbol{q}\cdot\boldsymbol{x}}\,\exp\left\{-\frac{\mathrm{i}}{2k}\int_{-\infty}^{z}U(\boldsymbol{b},z')\,\mathrm{d}z'\right\}\mathrm{d}^3x \;, \end{aligned} \tag{5.24}$$

where we defined $\boldsymbol{q} := \boldsymbol{k} - \boldsymbol{k}'$. Using the spherical symmetry of the optical potential and (2.12), we define

$$\eta(r,\cos\theta) := \exp\left\{-\frac{\mathrm{i}}{2k}\int_{-\infty}^{z}U(\boldsymbol{b},z')\,\mathrm{d}z'\right\} = \exp\left\{-\frac{\mathrm{i}}{2k}\int_{-\infty}^{r\cos\theta}U(\sqrt{r^2\sin^2\theta + z'^2})\,\mathrm{d}z'\right\}$$

to expand (5.24) into partial waves

$$\widehat{\phi}(\boldsymbol{k}') = 4\pi\sum_{\ell=0}^{\infty}\sum_{m=-\ell}^{\ell}\mathrm{i}^\ell Y_{\ell m}^*(\hat{q})\int_0^\infty\int_{-1}^{1}\int_0^{2\pi} j_\ell(qr)\eta(r,\cos\theta)Y_{\ell m}(\hat{r})\,\mathrm{d}\varphi\,\mathrm{d}(\cos\theta)\,r^2\mathrm{d}r \;.$$

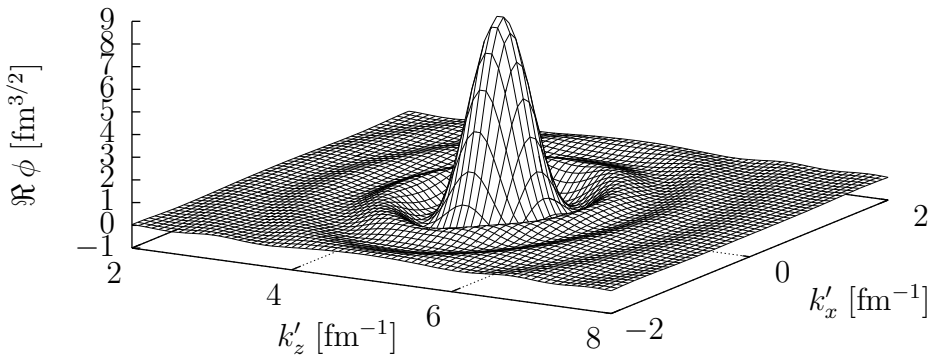

Figure 5.13: The real part $\Re\,\widehat{\phi}$ of the π^+ eikonal wave function in ^{12}C in momentum space for $p_{\mathrm{lab}} = 1050$ MeV in the k'_x-k'_z-plane.

Since the spherical harmonic $Y_{\ell m}(\hat{r})$ is the only function depending on the angle φ of the coordinate vector $\boldsymbol{x}$, we can perform the φ-integration, which gives

$$\int_0^{2\pi} Y_{\ell m}(\cos\theta, \varphi)\,\mathrm{d}\varphi = 2\pi Y_{\ell 0}(\cos\theta)\delta_{m0}\ .$$

Therefore, the momentum space wave function in the eikonal approximation is given by

$$\widehat{\phi}(\boldsymbol{k}') = 8\pi^2 \sum_{\ell=0}^{\infty} \mathrm{i}^{\ell} Y^*_{\ell 0}(\hat{q}) \int_0^{\infty}\int_{-1}^{1} r^2 j_\ell(qr)\eta(r,\cos\theta)Y_{\ell 0}(\cos\theta)\,\mathrm{d}(\cos\theta)\,\mathrm{d}r\ . \qquad (5.25)$$

The disadvantage of (5.25) when compared to (5.23) is, that the integration over r and $\cos\theta$ has to be performed. In the case of the full distorted waves, (5.23), only the r-integration remains since the angular dependence ends up in the Legendre polynomial $P_\ell(\cos\gamma)$.

The pion eikonal wave function in momentum space, projected onto the k'_x-k'_z-plane, is shown in figure 5.15. One can clearly see the peak at $k'_x = 0$ and $k'_z = 4.9$ fm^{-1}, which is the asymptotic momentum for $p_{\mathrm{lab}} = 1050$ MeV. [1]

[1] There are small-scale oscillations which are suppressed by about eight orders of magnitude and not visible in the linear scale in the figure. These are numerical artifacts due to the finite number of points and the finite size of the lattice in coordinate space which is also determined by the maximum ℓ which, in turn, is restricted by the stability of the algorithms used for j_ℓ and $Y_{\ell 0}$.

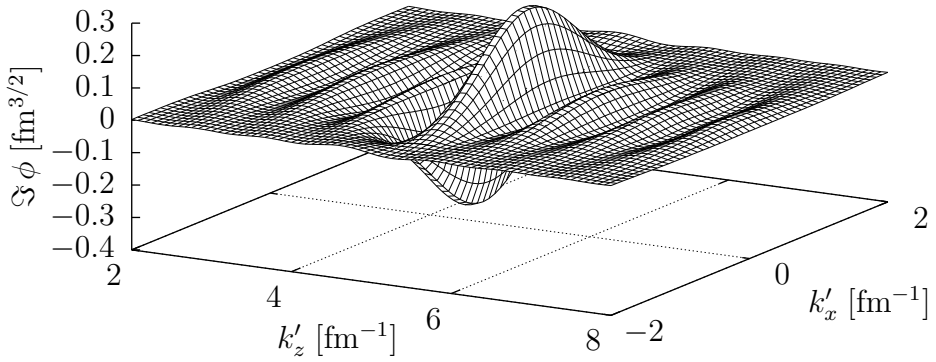

Figure 5.14: The imaginary part $\Im\,\widehat{\phi}$ of the π^+ eikonal wave function in ^{12}C in momentum space for $p_{\text{lab}} = 1050$ MeV in the k'_x-k'_z-plane.

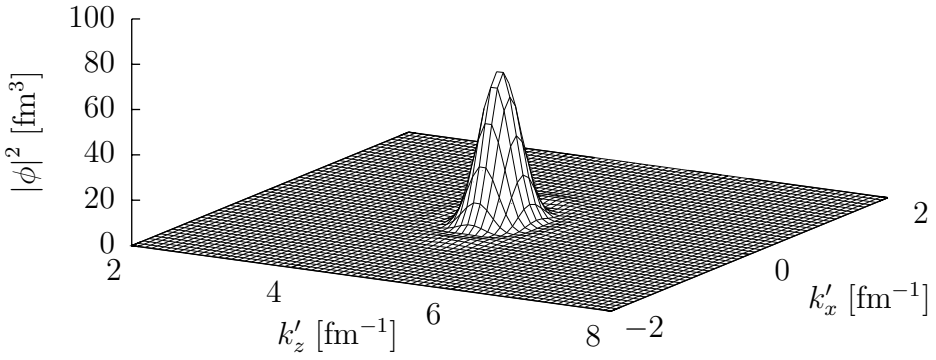

Figure 5.15: The magnitude of the π^+ eikonal wave function in ^{12}C in momentum space for $p_{\text{lab}} = 1050$ MeV in the k'_x-k'_z-plane.

5.6 Matrix elements

We are now in a position to revisit the evaluation of the matrix elements from section 4.3 for the calculation of the differential cross section. The coordinate integrals (x and y in (4.11)–(4.13)) are actually the Fourier transforms of the meson wave functions and we can use the results from section 5.5. In the following sections we restrict ourselves to the pseudoscalar case for the description of how the calculation of the matrix element $\mathcal{M}$ is performed. The other cases are then straight forward to evaluate.

5.6.1 Plane wave approximation

Starting from (4.11), as a first approximation we use plane waves for the kaon and pion wave functions, which are states of sharp momentum; that is, we set

$$\begin{aligned}\phi_{\mathrm{K}}(x) &= \mathrm{e}^{-\mathrm{i}k_{\mathrm{K}}\cdot x}\ ,\\ \phi_{\pi}(x) &= \mathrm{e}^{-\mathrm{i}k_{\pi}\cdot x}\ .\end{aligned}$$

Since the corresponding space-time integrations result in $(2\pi)^4\delta^{(4)}(p-k_\Lambda-k_{\mathrm{K}})$ and $(2\pi)^4\delta^{(4)}(p-k_{\mathrm{N}}-k_\pi)$, respectively, the integrations over two of the momenta are easily performed analytically. We choose to integrate over d^4p and $\mathrm{d}^4k_{\mathrm{N}}$, which leaves the integral over the (four-dimensional) phase space of the Λ

$$\mathcal{M} = \int\frac{\mathrm{d}^4k_\Lambda}{(2\pi)^4}\bar\psi_\Lambda(k_\Lambda)\Gamma_1\,\mathrm{i}\frac{\gamma\cdot(k_\Lambda+k_{\mathrm{K}})+m_{\mathrm{R}}}{(k_\Lambda+k_{\mathrm{K}})^2-m_{\mathrm{R}}^2+\mathrm{i}\epsilon}\Gamma_2\psi_{\mathrm{N}}(k_\Lambda+k_{\mathrm{K}}-k_\pi)\ . \tag{5.26}$$

5.6.2 Distorted wave approximation

When we use distorted waves for the kaon, keeping the plane wave for the pion, then the Fourier transform of the kaon wave function stays in the integral (4.11). Performing the integration over d^4p using the δ-function from the pion plane wave, we eventually have to evaluate

$$\mathcal{M} = \int\frac{\mathrm{d}^4k_{\mathrm{N}}}{(2\pi)^4}\int\frac{\mathrm{d}^4k_\Lambda}{(2\pi)^4}\widehat{\phi}^*_{\mathrm{K}}(k_{\mathrm{N}}+k_\pi-k_\Lambda)\bar\psi_\Lambda(k_\Lambda)\Gamma_1\,\mathrm{i}\frac{\gamma\cdot(k_{\mathrm{N}}+k_\pi)+m_{\mathrm{R}}}{(k_{\mathrm{N}}+k_\pi)^2-m_{\mathrm{R}}^2+\mathrm{i}\epsilon}\Gamma_2\psi_{\mathrm{N}}(k_{\mathrm{N}})\ . \tag{5.27}$$

On the other hand, using distorted waves for the pion and plane waves for the kaon, we have to keep the pion wave function in the integral. In this case we can perform the integration over d^4p using the δ-function from the kaon plane wave, which leads to the integral

$$\mathcal{M} = \int\frac{\mathrm{d}^4k_{\mathrm{N}}}{(2\pi)^4}\int\frac{\mathrm{d}^4k_\Lambda}{(2\pi)^4}\bar\psi_\Lambda(k_\Lambda)\Gamma_1\,\mathrm{i}\frac{\gamma\cdot(k_\Lambda+k_{\mathrm{K}})+m_{\mathrm{R}}}{(k_\Lambda+k_{\mathrm{K}})^2-m_{\mathrm{R}}^2+\mathrm{i}\epsilon}\Gamma_2\widehat{\phi}_\pi(k_\Lambda+k_{\mathrm{K}}-k_{\mathrm{N}})\psi_{\mathrm{N}}(k_{\mathrm{N}})\ . \tag{5.28}$$

Using distorted waves for both mesons in the momentum representation, we have to perform the whole 12-dimensional integration numerically. The matrix element $\mathcal{M}$ in that case is given by

$$\mathcal{M} = \int \frac{\mathrm{d}^4 k_\mathrm{N}}{(2\pi)^4} \int \frac{\mathrm{d}^4 k_\Lambda}{(2\pi)^4} \int \frac{\mathrm{d}^4 p}{(2\pi)^4} \widehat{\phi}^*_\mathrm{K}(p - k_\Lambda) \bar{\psi}_\Lambda(k_\Lambda) \Gamma_1 \, \mathrm{i} \frac{\gamma \cdot p + m_\mathrm{R}}{p^2 - m_\mathrm{R}^2 + \mathrm{i}\epsilon} \Gamma_2 \widehat{\phi}_\pi(p - k_\mathrm{N}) \psi_\mathrm{N}(k_\mathrm{N}) \; . \tag{5.29}$$

We additionally shift the integration from the nucleon to the meson by setting

$$\begin{aligned} k'_\mathrm{K} &:= k_\mathrm{N} + k_\pi - k_\Lambda \; , \\ k'_\pi &:= k_\Lambda + k_\mathrm{K} - k_\mathrm{N} \; , \end{aligned}$$

which means that k_N is replaced by

$$\begin{aligned} k_\mathrm{N} &= k_\Lambda + k'_\mathrm{K} - k_\pi \quad \text{and} \\ k_\mathrm{N} &= k_\Lambda + k_\mathrm{K} - k'_\pi \; , \end{aligned}$$

respectively. Instead of using k_N and p as integration variables in (5.27)–(5.29), we use then k'_K and k'_π.

5.6.3 Evaluation of the matrix elements

In this section we briefly sketch the details for the actual evaluation of the matrix elements as given by (5.26), (5.27), (5.28), or (5.29). For faster computation and numerical evaluation, we simplify the integrands with the help of the Dirac equation with a potential [124]. It is given in momentum space by

$$\not{p} \psi(p) = m \psi(p) + F(p) \; ,$$

where the additional term $F(p)$ is given by the convolution of the potential(s) V (see section 2.4, in particular (2.7)) with the spinor ψ,

$$F(p) = \delta(p_0 - E) \left[\int \mathrm{d}^3 k \, V_\mathrm{s}(-\boldsymbol{k}) \psi(\boldsymbol{p} + \boldsymbol{k}) - \gamma^0 \int \mathrm{d}^3 k \, V_\mathrm{v}(-\boldsymbol{k}) \psi(\boldsymbol{p} + \boldsymbol{k}) \right] \; .$$

We present the details of this evaluation for the plane wave case only, as the other cases are straight forward to evaluate from there on. First, we note that it is possible to bring all the integrands in (5.26)–(5.29) into the following form, thereby calling the integrand M:

$$\begin{aligned} M = {} & \bar{\psi}_\Lambda (c_1 + c'_1 \not{k}_\mathrm{K}) \psi_\mathrm{N} \quad + \bar{\psi}_\Lambda (c_2 + c'_2 \not{k}_\mathrm{K}) F_\mathrm{N} \quad + \bar{F}_\Lambda (c_3 + c'_3 \not{k}_\mathrm{K}) \psi_\mathrm{N} \quad + \bar{F}_\Lambda (c_4 + c'_4 \not{k}_\mathrm{K}) F_\mathrm{N} \\ =: {} & \quad M_1 \quad + \quad M_2 \quad + \quad M_3 \quad + \quad M_4 \; . \end{aligned} \tag{5.30}$$

Next, we use the explicit form of the spinor wave functions $\psi(p)$ of the (hyper)nuclear bound states as it was discussed in chapter 2. The $\psi(p)$, and in a

similar manner the $F(p)$, are given by

$$\psi(p) = \delta(p_0 - E) \begin{pmatrix} f_{n,j}(|\boldsymbol{p}|)\, \mathcal{Y}^{jm_j}_{\ell s}(\hat{p}) \\ -\mathrm{i} g_{n,j}(|\boldsymbol{p}|)\, \mathcal{Y}^{jm_j}_{\ell' s}(\hat{p}) \end{pmatrix} , \tag{5.31a}$$

$$F(p) = \delta(p_0 - E) \begin{pmatrix} \zeta_{n,j}(|\boldsymbol{p}|)\, \mathcal{Y}^{jm_j}_{\ell s}(\hat{p}) \\ -\mathrm{i} \zeta'_{n,j}(|\boldsymbol{p}|)\, \mathcal{Y}^{jm_j}_{\ell' s}(\hat{p}) \end{pmatrix} , \tag{5.31b}$$

with the spinor-spherical harmonics defined by (2.10).

After bringing (5.26)–(5.29) into the form of (5.30), which is explained in detail in appendix E, including the constants $c_1, \ldots, c'_4$. We can then use the explicit forms (5.31) to further simplify M by using the orthogonality relations of the spherical harmonics and the two-dimensional spinor vectors. As an example, the first term of (5.30), M_1, in explicit matrix form reads

$$\begin{aligned} M_1 &:= \bar{\psi}_\Lambda (c_1 + c'_1 \not{k}_\mathrm{K}) \psi_\mathrm{N} \\ &= \delta(p^0_\Lambda - E_\Lambda) \delta(p^0_\mathrm{N} - E_\mathrm{N}) \\ &\quad \times \begin{pmatrix} f_\Lambda\, \mathcal{Y}^\dagger_\Lambda(\hat{p}_\Lambda) & \mathrm{i} g_\Lambda\, \mathcal{Y}^\dagger_{\Lambda'}(\hat{p}_\Lambda) \end{pmatrix} \begin{pmatrix} c_1 + c'_1 k^0_\mathrm{K} & -c'_1 \boldsymbol{\sigma} \cdot \boldsymbol{k}_\mathrm{K} \\ -c'_1 \boldsymbol{\sigma} \cdot \boldsymbol{k}_\mathrm{K} & -c_1 + c'_1 k^0_\mathrm{K} \end{pmatrix} \begin{pmatrix} f_\mathrm{N}\, \mathcal{Y}_\mathrm{N}(\hat{p}_\mathrm{N}) \\ -\mathrm{i} g_\mathrm{N}\, \mathcal{Y}_{\mathrm{N}'}(\hat{p}_\mathrm{N}) \end{pmatrix} , \end{aligned} \tag{5.32}$$

where we abbreviated the respective orbital and total angular momentum variables and spin states by the subscripts $\Lambda^{(\prime)}$ and $\mathrm{N}^{(\prime)}$ for simplicity:

$$\begin{aligned} \mathcal{Y}_\Lambda &:= \mathcal{Y}^{j_\Lambda m_{j\Lambda}}_{\ell_\Lambda s_\Lambda} , \qquad & \mathcal{Y}_{\Lambda'} &:= \mathcal{Y}^{j_\Lambda m_{j\Lambda}}_{\ell'_\Lambda s_\Lambda} , \\ \mathcal{Y}_\mathrm{N} &:= \mathcal{Y}^{j_\mathrm{N} m_{j\mathrm{N}}}_{\ell_\mathrm{N} s_\mathrm{N}} , \qquad & \mathcal{Y}_{\mathrm{N}'} &:= \mathcal{Y}^{j_\mathrm{N} m_{j\mathrm{N}}}_{\ell'_\mathrm{N} s_\mathrm{N}} . \end{aligned}$$

From the expansion of (5.32) it can be seen that M_1 is given by a sum of four terms which mix f_Λ, g_Λ, f_N, and g_N, together with their accompanying spinor-spherical harmonics. We go into more explicit details about the evaluation in appendix E.

Putting then all four terms from (5.30) together, the full expression for the integrand is given by (E.4). Finally, we make use of the δ-functions for the zeroth component of the momentum in the wave functions (5.31) for ψ and F. We are then left with a three-dimensional momentum integral for each undetermined momentum, which are the Λ momentum in the plane wave case, and additionally the meson momentum when using distorted waves. These resulting integrals are eventually evaluated numerically with a Monte-Carlo [125] or a deterministic [126] integration algorithm.

6 Results I: Plane wave calculations

In this chapter, we present the results of our calculations done in the plane wave approximation where the initial and final state interactions of the mesons with the (hyper)nucleus are neglected. We present our results for different nuclei and compare them, where available, to experimental data.

Very good angle resolved data are available from [42], where the production of hypernuclei via the reaction $\mathrm{A}(\pi^+, \mathrm{K}^+)\,{}_\Lambda\mathrm{A}$ was investigated for ^{12}C, ^{51}V, and ^{89}Y. Here, however, we restrict the results to the spherically symmetric nuclei ^{12}C and ^{40}Ca.

In these experiments, the incident pion momentum was chosen as $p_{\mathrm{lab}} = 1050$ MeV. It was selected because of an available pion beam on one hand and a maximum of the elementary reaction cross section [42, 49] on the other hand.

6.1 Results for ^{12}C

Because of the relatively high incident energy, we expect the initial and final state interactions to be of minor importance. We compare our calculations to the experimental data taken from [42]. For the comparison with this data, the incoming pion momentum in the laboratory frame is taken to be 1050 MeV, corresponding to a kinetic energy $T_{\mathrm{lab}} = 920$ MeV, unless otherwise noted.

6.1.1 The $\mathrm{np}_{3/2} \longrightarrow \Lambda\mathrm{s}_{1/2}$ transition

The first process is the Λ-production on the neutron in the $p_{3/2}$ orbital, and the Λ occupying the $s_{1/2}$ orbital. Our results for this transition are shown in figure 6.1, and apart from overestimating the differential cross section compared to experimental data, one can see that all three resonances take part in the production process by about the same amount. The experimental data seems to deviate from the theoretical curve with increasing angle, but the inspected angular range from 2° to 14° in the experiment is not conclusive enough to find out if this discrepancy continues at larger scattering angles and hints at different diffraction patterns.

In figure 6.2, we show the differential cross section over the whole angular range from 0° to 180° for the same process at the same pion incoming momentum. Again, all three resonances contribute by approximately the same amount to the total cross section (obtained by summing the resonance amplitudes coherently) at small scattering angles. At larger scattering angles, interference effects reduce the summed cross section to values below the single resonance contributions at some points.

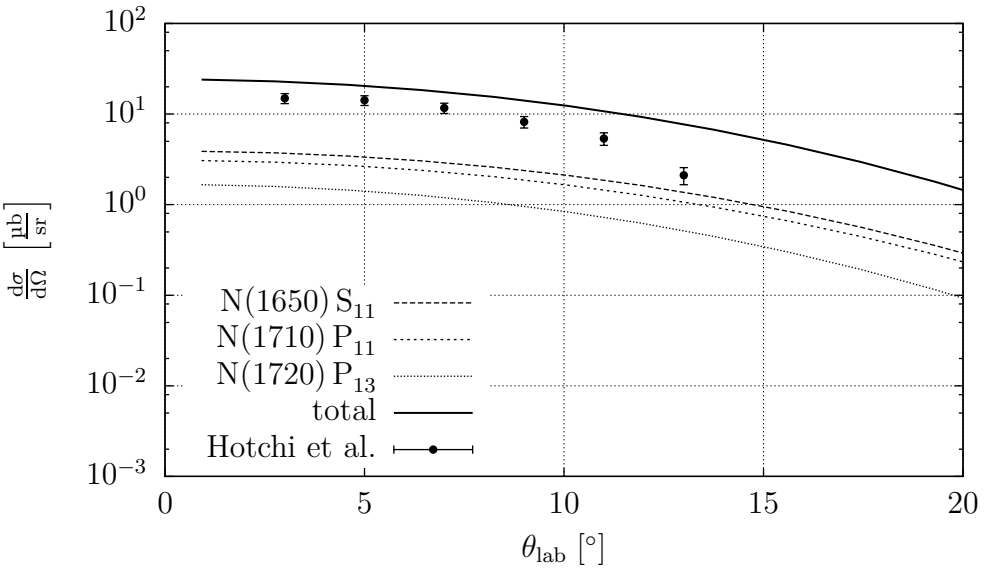

Figure 6.1: The differential cross section for $\pi^+ + {}^{12}\mathrm{C} \rightarrow \mathrm{K}^+ + {}^{12}_{\Lambda}\mathrm{C}$, where the neutron occupies the $p_{3/2}$ orbital, and the Λ the $s_{1/2}$ orbital at a pion incoming momentum of 1050 MeV.

Additionally, the difference in the diffraction pattern between our calculations and the experimental data is even more evident. Unfortunately, and as already mentioned, the experimental angular range is too small to reach a definitive conclusion about this difference. Since the diffraction structure is related to the nuclear form factor, it may be a hint that the bound state wave function is actually larger than calculated in section 2.5.

The cross section as a function of the dimensionless $\cos\theta$ is shown in figure 6.3. Instead of the angle of the outgoing kaon, which is indicated at the x-axis in figures 6.1 and 6.2, the dependence on the magnitude of the momentum transfer $\boldsymbol{q} = \boldsymbol{p}_\pi - \boldsymbol{p}_\mathrm{K}$, $q := |\boldsymbol{q}|$, might provide a better picture. The differential cross section depending on q is shown in figure 6.4.

Furthermore, we calculated the differential cross section for the above process with a varying incoming pion momentum from 700 MeV to 2000 MeV. Our results as a function of the outgoing kaon angle are shown in figure 6.5. The angular dependence varies greatly with the incoming momentum in both, diffraction structure and magnitude. For 700 MeV, which is close to the reaction threshold, we get a flat angular distribution. Increasing the incoming pion momentum leads to an increasingly forward-peaked angular dependence. At $p_\mathrm{lab} \approx 1$ GeV this distribution shows a maximum in its magnitude at the forward angle. Further increasing the incoming momentum leads to even stronger forward peaking but less absolute magnitudes of the differential cross section.

A more revealing figure is obtained by plotting the differential cross section against the momentum transfer q. Figure 6.6 shows this dependence and it can

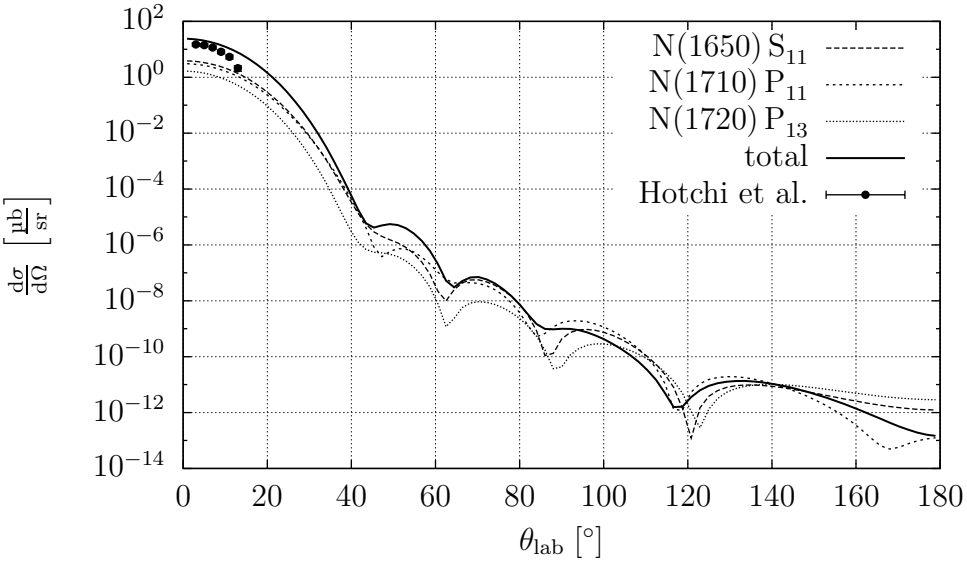

Figure 6.2: The differential cross section for $\pi^+ + {}^{12}\mathrm{C} \rightarrow \mathrm{K}^+ + {}^{12}_{\Lambda}\mathrm{C}$ at a pion incoming momentum of 1050 MeV over the complete angular range from 0° to 180°.

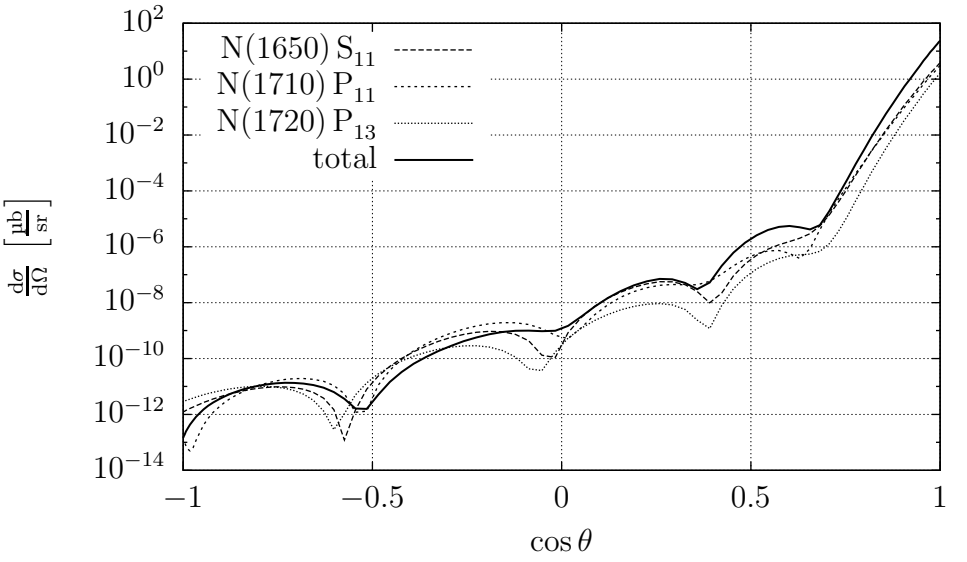

Figure 6.3: The differential cross section for $\pi^+ + {}^{12}\mathrm{C} \rightarrow \mathrm{K}^+ + {}^{12}_{\Lambda}\mathrm{C}$ at a pion incoming momentum of 1050 MeV as a function of $\cos\theta$ from -1 to 1.

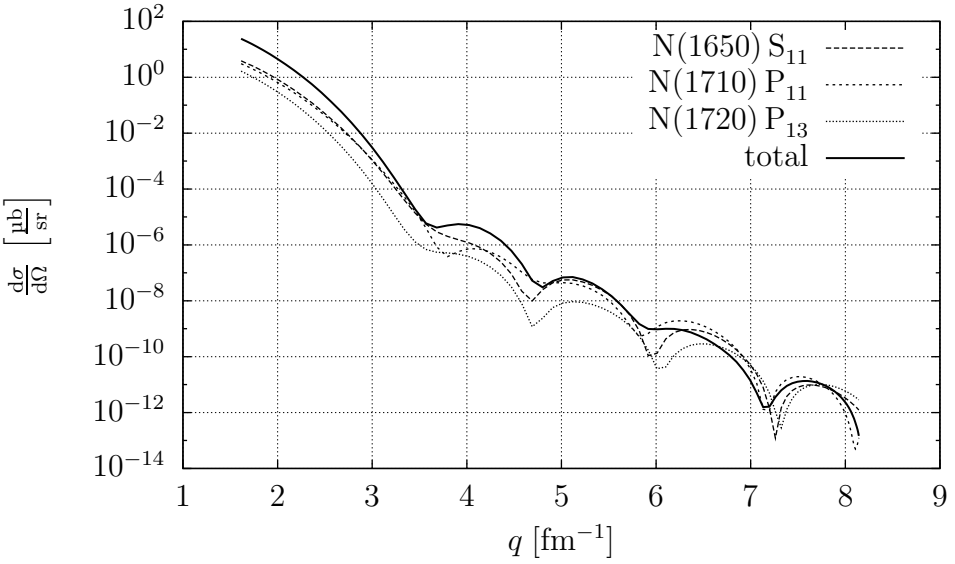

Figure 6.4: The differential cross section for $\pi^+ + {}^{12}\mathrm{C} \rightarrow \mathrm{K}^+ + {}^{12}_{\Lambda}\mathrm{C}$ at a pion incoming momentum of 1050 MeV as a function of the momentum transfer q.

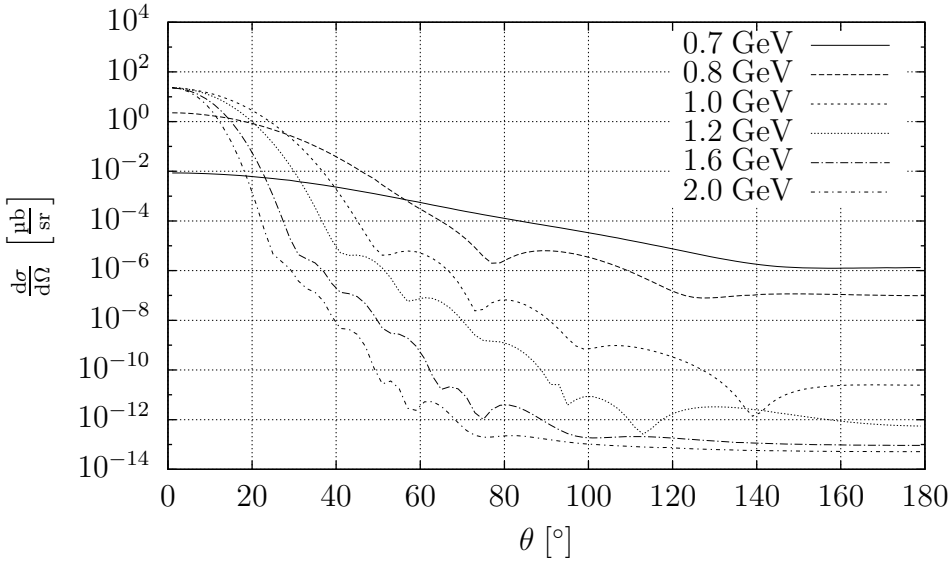

Figure 6.5: The differential cross section for $\pi^+ + {}^{12}\mathrm{C} \rightarrow \mathrm{K}^+ + {}^{12}_{\Lambda}\mathrm{C}$, where the neutron occupies the $p_{3/2}$ orbital, and the Λ the $s_{1/2}$ orbital for a pion incoming momentum range from 700 MeV to 2000 MeV.

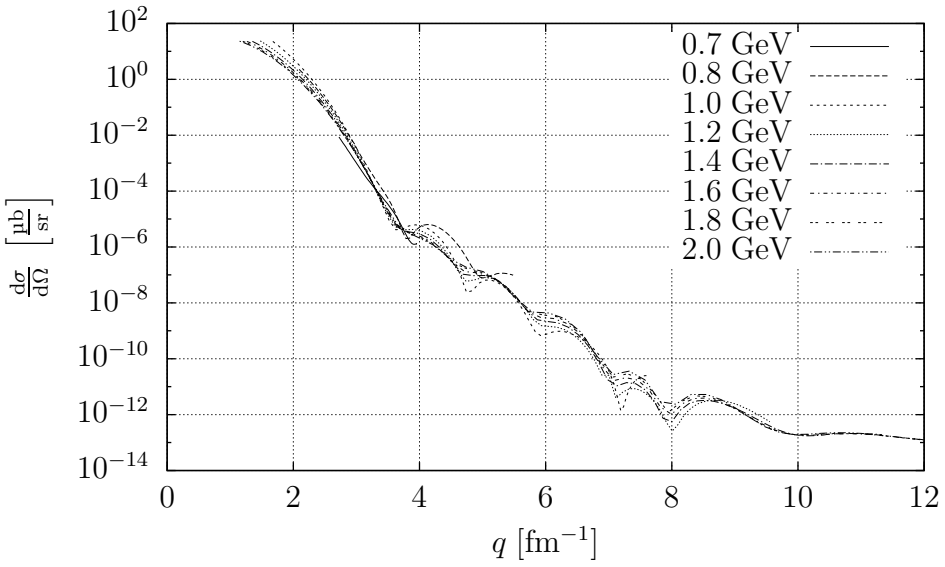

Figure 6.6: The differential cross section for $\pi^+ + {}^{12}\mathrm{C} \rightarrow \mathrm{K}^+ + {}^{12}_{\Lambda}\mathrm{C}$ for the $(\mathrm{n}^{-1}_{p3/2}, \Lambda_{s1/2})$ transition as it depends on the momentum transfer q for a pion incoming momentum range from 700 MeV to 2000 MeV.

be seen, that the different diffraction minima occur at the approximately the same momentum transfers independently from the pion incident momentum.

The total cross section can be calculated from the angular distributions, and it is shown in figure 6.7. The maximum is reached at $p_{\mathrm{lab}} \approx 1$ GeV which confirms what can already be seen in figure 6.5.

6.1.2 The $\mathrm{np}_{3/2} \rightarrow \Lambda\mathrm{p}_{3/2}$ transition

The next Λ-bound state in $^{12}_{\Lambda}$C is the $p_{3/2}$ orbital, which is just bound by about 0.1 MeV. We show the differential cross section for this transition, where the Λ occupies the same orbital as the neutron, compared to experimental data [42] in figure 6.8. One can see that we underestimate the differential cross section at very small scattering angles, but match the data at approximately 10°. It even suggests that the curve of the diffraction structure is matched well. But, as discussed above, the experimental angular range is too small to draw definitive conclusions.

The differential cross section over the whole θ range is shown in figure 6.9 and as a function of $\cos\theta$ in figure 6.10. The dependence on the momentum transfer q is shown in figure 6.11.

Here, again, we calculated the differential cross section with a varying incoming pion momentum from 700 MeV to 2000 MeV. The results as a function of the outgoing kaon angle for some selected pion momenta are shown in figure 6.12. Similar to the results in the previous section, the differential cross section starts out from a flat distribution close to threshold, becoming increasingly forward-peaked

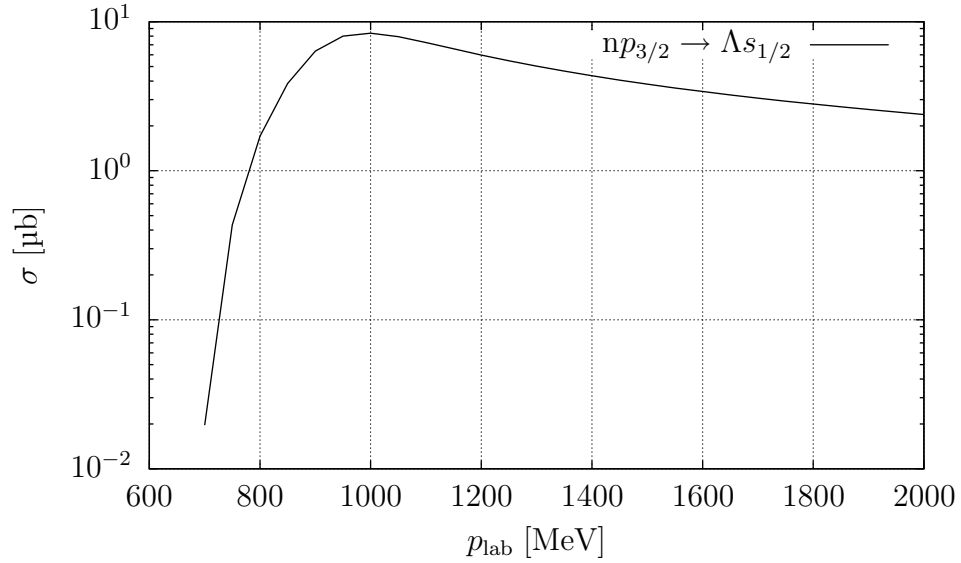

Figure 6.7: The total cross section for $\pi^+ + {}^{12}\mathrm{C} \rightarrow \mathrm{K}^+ + {}^{12}_{\Lambda}\mathrm{C}$ for the $(\mathrm{n}^{-1}_{p3/2}, \Lambda_{s1/2})$ transition as a function of the incident pion momentum p_{lab}.

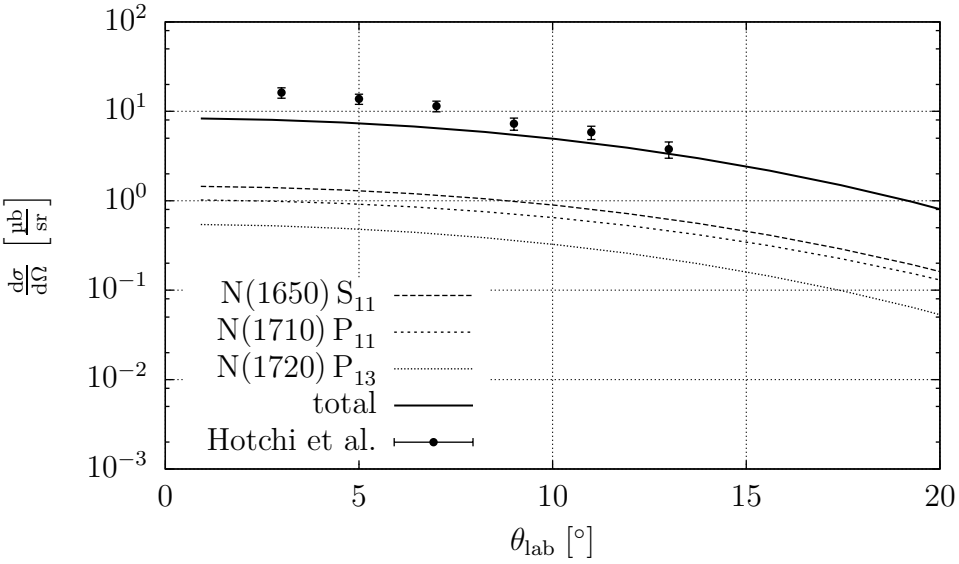

Figure 6.8: The differential cross section for $\pi^+ + {}^{12}\mathrm{C} \rightarrow \mathrm{K}^+ + {}^{12}_{\Lambda}\mathrm{C}$, where the neutron occupies the $p_{3/2}$ orbital, and the Λ the $p_{3/2}$ orbital at a pion incoming momentum of 1050 MeV.

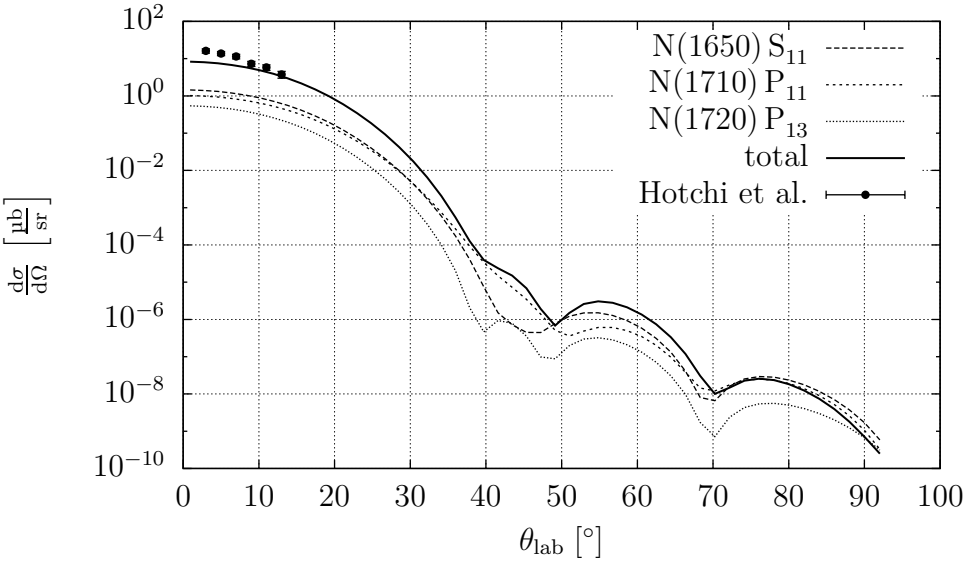

Figure 6.9: The differential cross section for $\pi^+ + {}^{12}\mathrm{C} \rightarrow \mathrm{K}^+ + {}^{12}_{\Lambda}\mathrm{C}$ at a pion incoming momentum of 1050 MeV over the complete angular range from 0° to 180°.

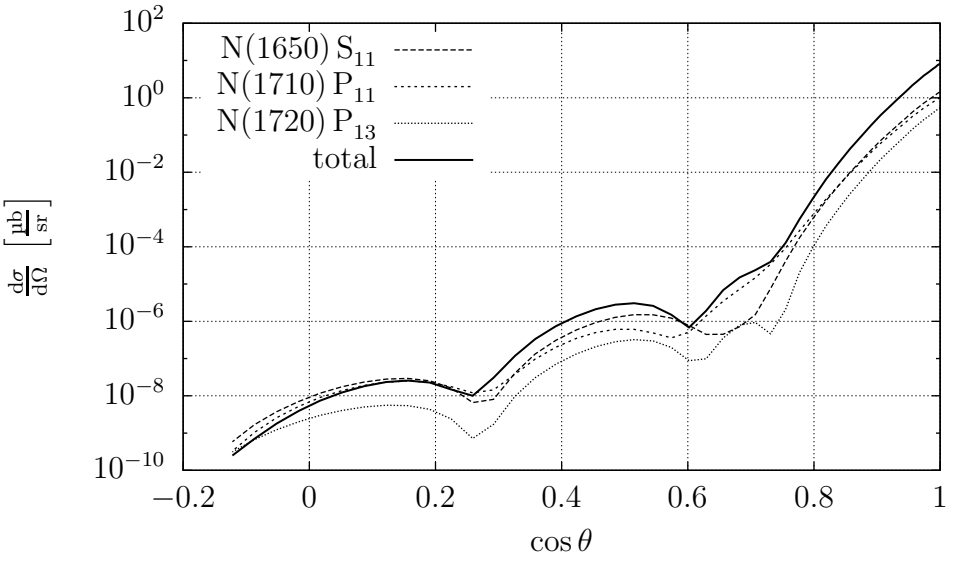

Figure 6.10: The differential cross section for $\pi^+ + {}^{12}\mathrm{C} \rightarrow \mathrm{K}^+ + {}^{12}_{\Lambda}\mathrm{C}$ at a pion incoming momentum of 1050 MeV as a function of $\cos\theta$ from -1 to 1.

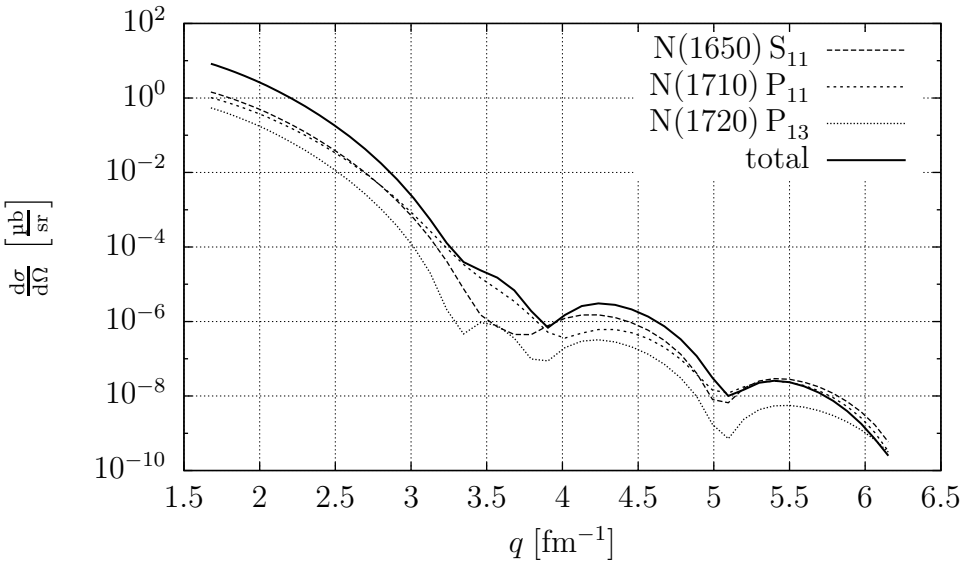

Figure 6.11: The differential cross section for $\pi^+ + {}^{12}\mathrm{C} \rightarrow \mathrm{K}^+ + {}^{12}_{\Lambda}\mathrm{C}$ at a pion incoming momentum of 1050 MeV as a function of the momentum transfer q.

at higher incoming momenta with a maximum at around 1 GeV.

The dependence of the differential cross section on the momentum transfer q is shown in figure 6.13. It can be seen that here too, the different diffraction minima occur at approximately the same momentum transfers for all incoming pion energies.

The total cross section for the considered momentum range, calculated from the angular distributions, is shown in figure 6.14. As noted above, the maximum is again at $p_{\mathrm{lab}} \approx 1$ GeV.

6.2 Results for ^{40}Ca

^{40}Ca is also a spherically symmetric nucleus with an equal number of protons and neutrons. It is larger than ^{12}C and therefore permits more bound states for the Λ than $^{12}_{\Lambda}$C. However, the experimental findings of Λ bound states show that these are not as well defined as in the Carbon case [43].

6.2.1 The $nd_{3/2} \rightarrow \Lambda s_{1/2}$ transition

In ^{40}Ca, the least bound neutron state is the $d_{3/2}$ orbital with a binding energy of 15.641 MeV [67]. The innermost Λ bound state is again the $s_{1/2}$ state as in the case of $^{12}_{\Lambda}$C. Since in this case there are no experimental data available, we present the results of our calculations for the whole θ-range in figure 6.15. It can be seen that

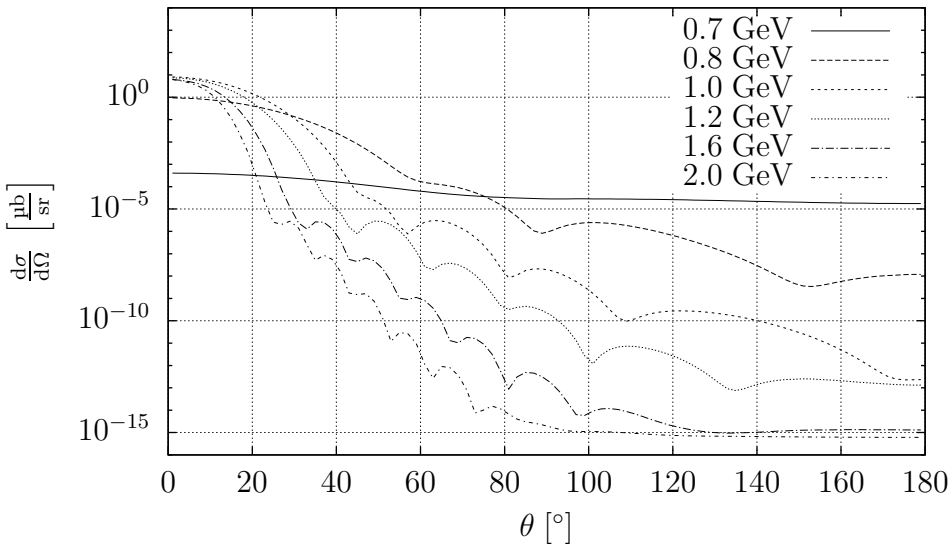

Figure 6.12: The differential cross section for $\pi^+ + {}^{12}\mathrm{C} \rightarrow \mathrm{K}^+ + {}^{12}_{\Lambda}\mathrm{C}$, where the neutron occupies the $p_{3/2}$ orbital, and the Λ the $p_{3/2}$ orbital for a pion incoming momentum range from 700 MeV to 2000 MeV.

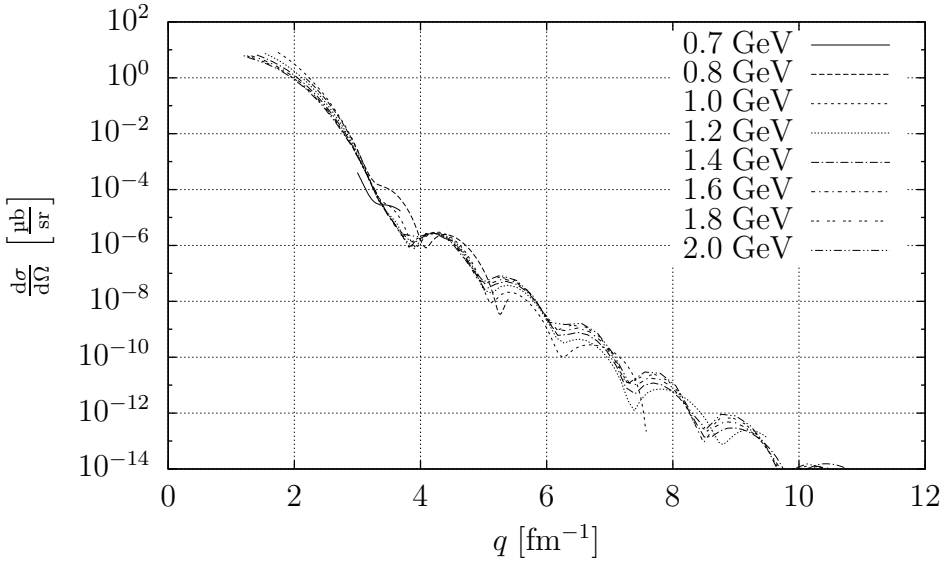

Figure 6.13: The differential cross section for $\pi^+ + {}^{12}\mathrm{C} \rightarrow \mathrm{K}^+ + {}^{12}_{\Lambda}\mathrm{C}$ for the $(\mathrm{n}^{-1}_{p3/2}, \Lambda_{p3/2})$ transition as it depends on the momentum transfer q for a pion incoming momentum range from 700 MeV to 2000 MeV.

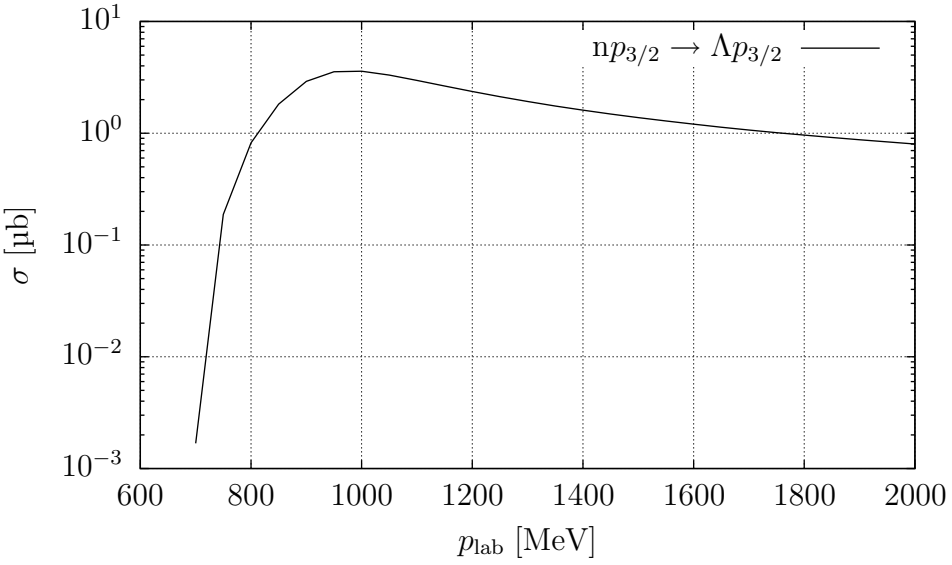

Figure 6.14: The total cross section for $\pi^+ + {}^{12}\mathrm{C} \rightarrow \mathrm{K}^+ + {}^{12}_{\Lambda}\mathrm{C}$ for the $(\mathrm{n}^{-1}_{p3/2}, \Lambda_{p3/2})$ transition as a function of the incident pion momentum p_{lab}.

the diffraction pattern has a shorter period compared to the same process at ^{12}C. The reason for this is that the diffraction pattern is related to the nuclear form factor and hence to the mass distribution. In particular, the period is inversely proportional to the size of the nucleus.

The differential cross section as a function of $\cos\theta$ is shown in figure 6.16 and the q-dependence in figure 6.17. Again it can be seen that the all resonance contribute about the same to the reaction cross section with interference effects showing at larger scattering angles.

The incoming momentum dependence of the differential cross section for a pion momentum from 700 MeV to 2000 MeV is show in figure 6.18. Similar to the results on ^{12}C, the differential cross section starts out from a flat distribution close to threshold and becomes increasingly forward-peaked at higher incoming momenta. The maximum is again at around 1 GeV.

The q-dependence of the differential cross section for this incoming momentum range is shown in figure 6.19. The differences in the diffraction structure when viewing the angular dependence vanish and it can be seen that, again, the different diffraction minima occur at approximately the same momentum transfers. This leaves only slight differences in the magnitude visible in the figure.

The dependence of the total cross section on p_{lab}, for the considered momentum range and calculated from the angular distributions, is shown in figure 6.20. As noted above, the maximum is again at $p_{\mathrm{lab}} \approx 1$ GeV.

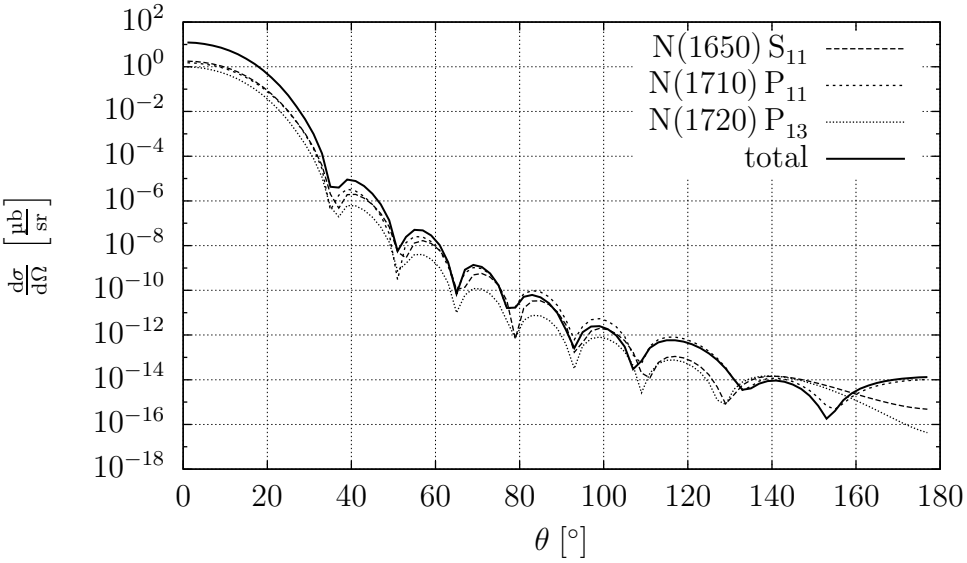

Figure 6.15: The differential cross section for $\pi^+ + {}^{40}\mathrm{Ca} \rightarrow \mathrm{K}^+ + {}^{40}_{\Lambda}\mathrm{Ca}$ at a pion incoming momentum of 1050 MeV over the complete angular range from 0° to 180°.

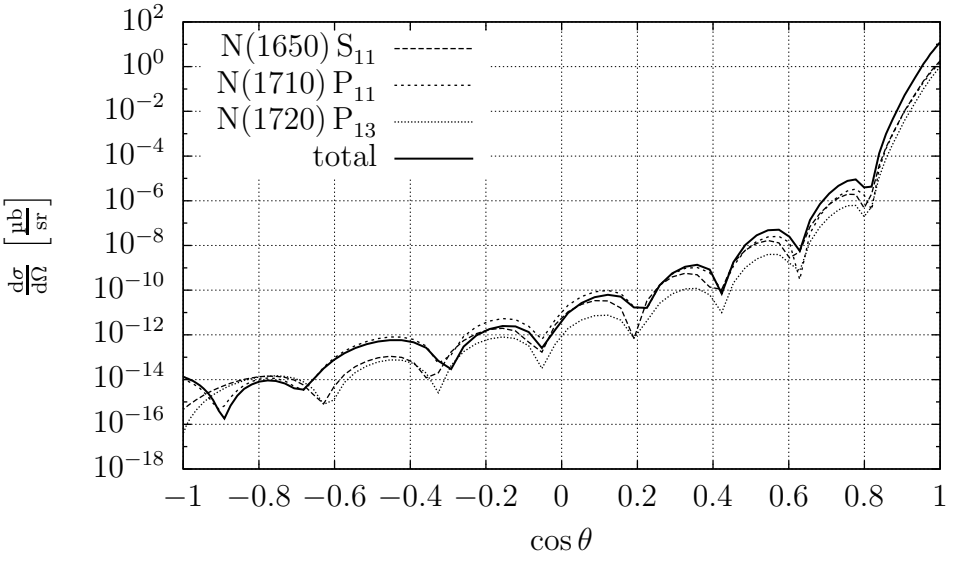

Figure 6.16: The differential cross section for $\pi^+ + {}^{40}\mathrm{Ca} \rightarrow \mathrm{K}^+ + {}^{40}_{\Lambda}\mathrm{Ca}$ at a pion incoming momentum of 1050 MeV as a function of $\cos\theta$ from -1 to 1.

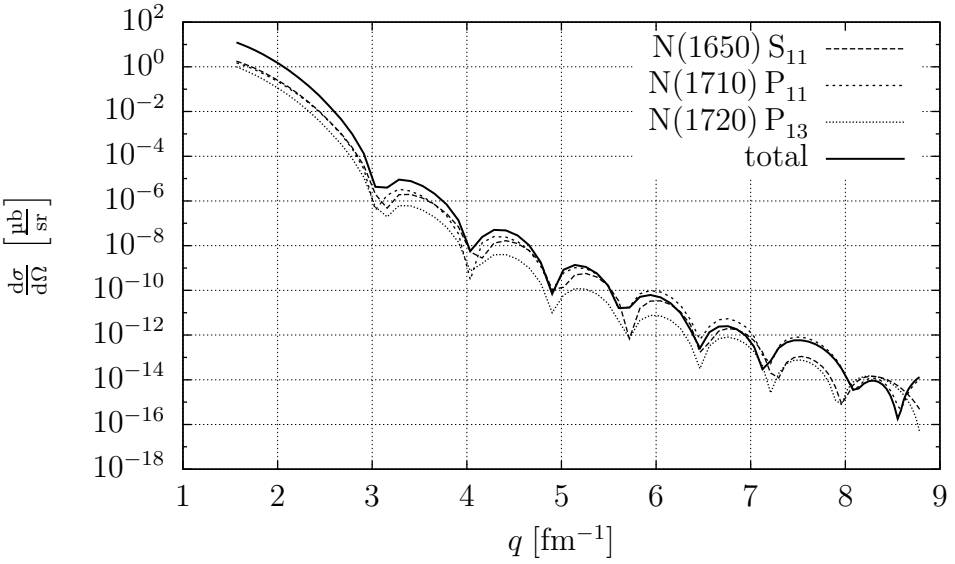

Figure 6.17: The differential cross section for $\pi^+ + {}^{40}\mathrm{Ca} \rightarrow \mathrm{K}^+ + {}^{40}_{\Lambda}\mathrm{Ca}$ at a pion incoming momentum of 1050 MeV as a function of the momentum transfer q.

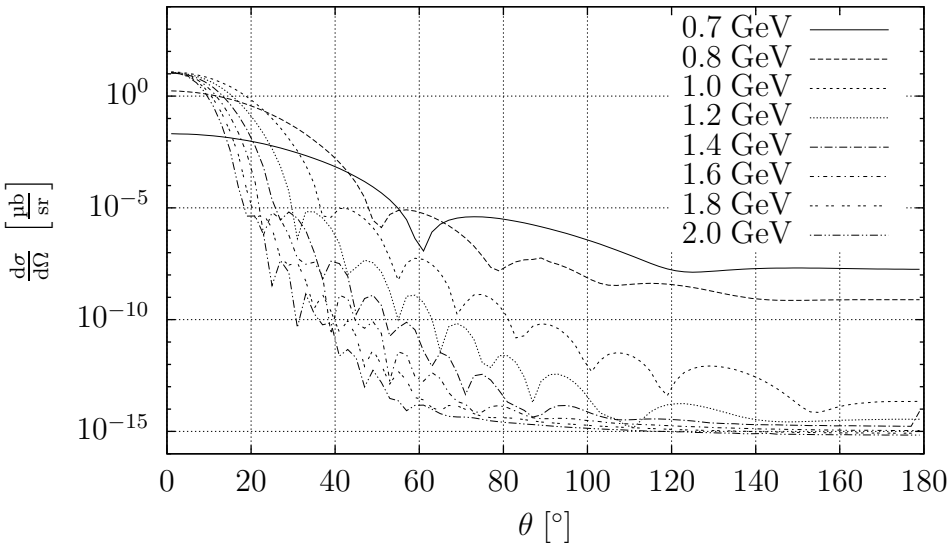

Figure 6.18: The angular dependence of the differential cross section for $\pi^+ + {}^{40}\mathrm{Ca} \rightarrow \mathrm{K}^+ + {}^{40}_{\Lambda}\mathrm{Ca}$ for the $(\mathrm{n}^{-1}_{d3/2}, \Lambda_{s1/2})$ transition and a pion incoming momentum range from 700 MeV to 2000 MeV.

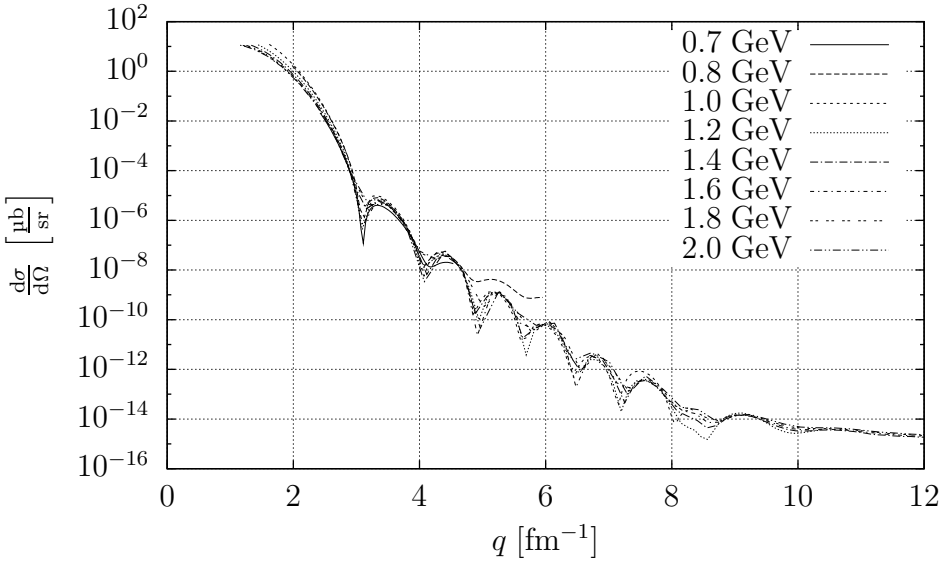

Figure 6.19: The differential cross section for $\pi^+ + {}^{40}\mathrm{Ca} \rightarrow \mathrm{K}^+ + {}^{40}_{\Lambda}\mathrm{Ca}$ for the $(\mathrm{n}^{-1}_{d3/2}, \Lambda_{s1/2})$ transition as it depends on the momentum transfer q for a pion incoming momentum range from 700 MeV to 2000 MeV.

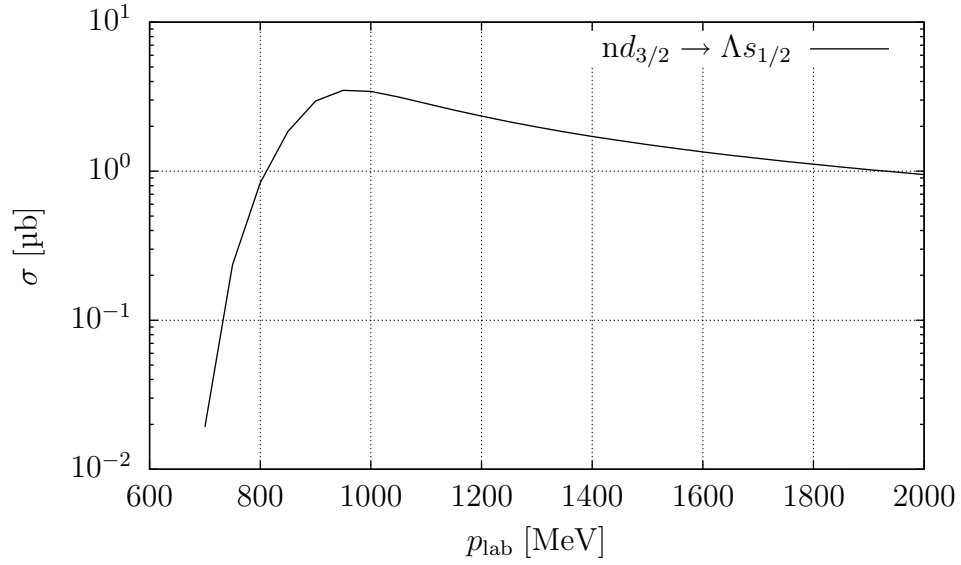

Figure 6.20: The total cross section for $\pi^+ + {}^{40}\mathrm{Ca} \rightarrow \mathrm{K}^+ + {}^{40}_{\Lambda}\mathrm{Ca}$ for the $(\mathrm{n}^{-1}_{d3/2}, \Lambda_{s1/2})$ transition as a function of the incident pion momentum p_{lab}.

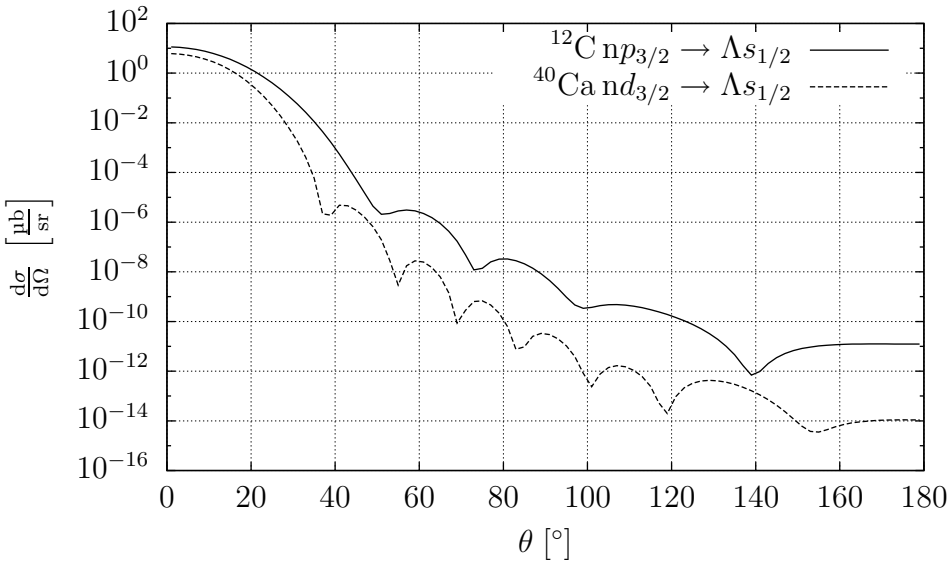

Figure 6.21: The differential cross sections for $\pi^+ + {}^{12}\mathrm{C} \to \mathrm{K}^+ + {}^{12}_{\Lambda}\mathrm{C}$ (solid line) and $\pi^+ + {}^{40}\mathrm{Ca} \to \mathrm{K}^+ + {}^{40}_{\Lambda}\mathrm{Ca}$ (dashed line) for the $(\mathrm{n}^{-1}_{p3/2}, \Lambda_{s1/2})$ transition in the first reaction and for the $(\mathrm{n}^{-1}_{d3/2}, \Lambda_{s1/2})$ transition in the second. Shown are the angular distributions for an incident pion momentum of $p_{\mathrm{lab}} = 1000$ MeV.

6.3 Comparison of ^{12}C and ^{40}Ca

Although the reactions on the two nuclei are quite different, we compare the results of our calculations for an incoming pion momentum $p_{\mathrm{lab}} = 1$ GeV, where both reactions have their maximum cross section. First, we show the difference in the diffraction pattern of both processes by looking at the angular distribution in figure 6.21. As can be seen, the cross section on ^{40}Ca is comparable to the one on ^{12}C at forward scattering angles and gets smaller in comparison at large scattering angles. The difference in the structure of the data reflects the larger radius of ^{40}Ca, as discussed above.

The differential cross section as a function of the momentum transfer q is shown in figure 6.22. Because of its larger rest mass, ^{40}Ca picks up less recoil from the reaction. Hence, more energy is transferred to the kaon which is reflected by the fact that the dashed line reaches higher q values.

The momentum dependence of the total cross section for both reactions is shown in figure 6.23. As already indicated by the angular distribution, the cross section on ^{40}Ca is smaller than the one on ^{12}C. The maximum of the total cross section gets also shifted a small amount to lower incoming momenta from $p_{\mathrm{lab}} = 1$ GeV to $p_{\mathrm{lab}} = 950$ MeV.

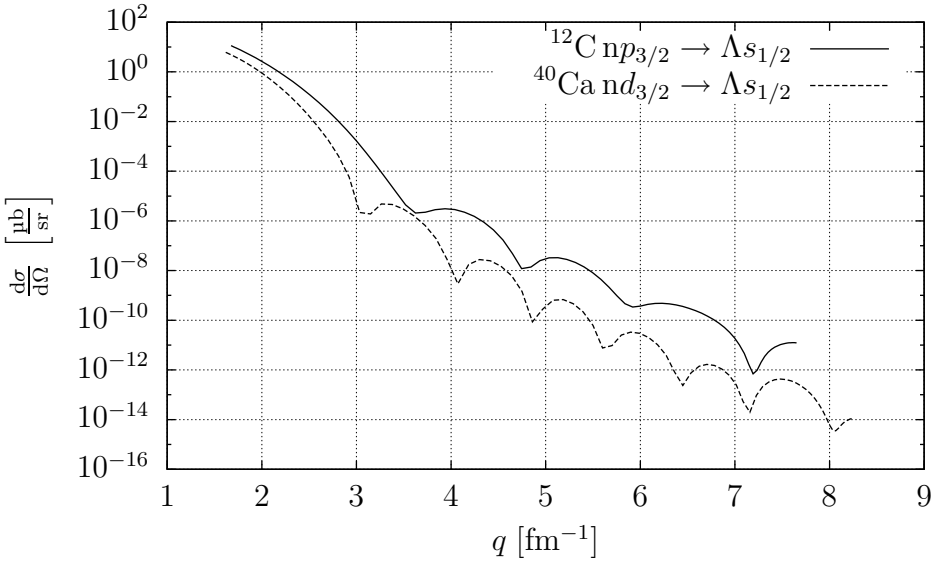

Figure 6.22: The momentum dependence of the differential cross sections for $\pi^+ + {}^{12}\mathrm{C} \rightarrow \mathrm{K}^+ + {}^{12}_{\Lambda}\mathrm{C}$ (solid line) and $\pi^+ + {}^{40}\mathrm{Ca} \rightarrow \mathrm{K}^+ + {}^{40}_{\Lambda}\mathrm{Ca}$ (dashed line), for the $(\mathrm{n}^{-1}_{p3/2}, \Lambda_{s1/2})$ transition in the first reaction and for the $(\mathrm{n}^{-1}_{d3/2}, \Lambda_{s1/2})$ transition in the second.

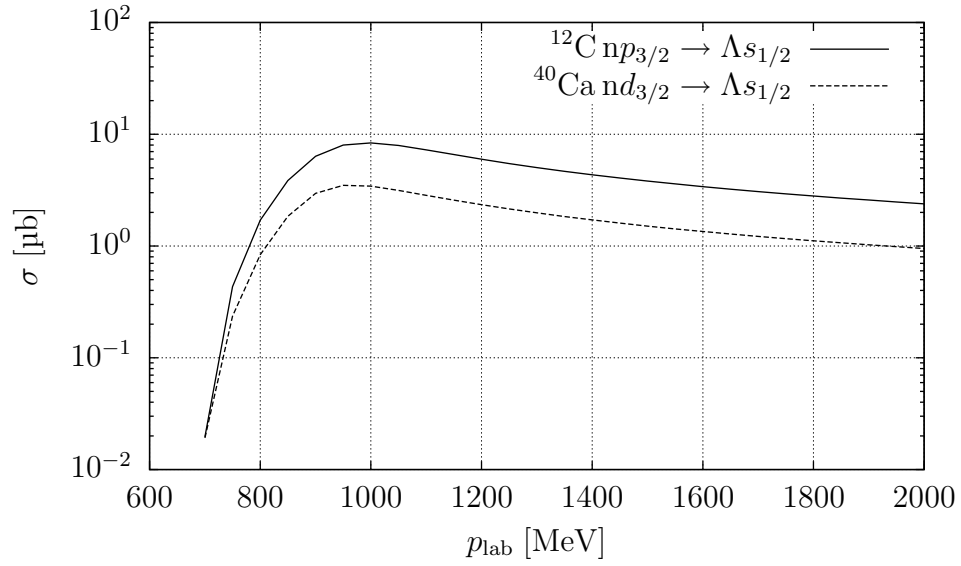

Figure 6.23: The total cross sections for $\pi^+ + {}^{12}\mathrm{C} \rightarrow \mathrm{K}^+ + {}^{12}_{\Lambda}\mathrm{C}$ (solid line) and $\pi^+ + {}^{40}\mathrm{Ca} \rightarrow \mathrm{K}^+ + {}^{40}_{\Lambda}\mathrm{Ca}$ (dashed line) for the $(\mathrm{n}^{-1}_{p3/2}, \Lambda_{s1/2})$ transition in the first reaction and for the $(\mathrm{n}^{-1}_{d3/2}, \Lambda_{s1/2})$ transition in the second, as a function of the incident pion momentum p_{lab}.

7 Results II: Distorted wave calculations

In this chapter, we present the results of the calculations with the inclusion of the initial state interactions introduced in chapter 5. We present the results including the initial state interactions within the eikonal approximation from section 5.4. The results of the previous chapter without these interactions are already comparable to experimental data. However, the absolute magnitude of the cross sections also depends on the total flux of the incoming and outgoing particles. This is expected to be reduced when the above mentioned interactions are taken into account.

7.1 Pion eikonal calculations

Because of its high energy, the first approximation to the pion wave function is the eikonal approximation, where the plane wave is modified by a straight line integral over the simplified optical potential as discussed in section 5.4. To make the comparison to the plane wave calculations easier, we start with the same differential cross sections as above.

Since the numerical calculations get expensive with respect to CPU time, we concentrate on the $\mathrm{n}p_{3/2} \to \Lambda s_{1/2}$ transition in the $\pi^+ + {}^{12}\mathrm{C} \to \mathrm{K}^+ + {}^{12}_{\Lambda}\mathrm{C}$ reaction at $p_{\mathrm{lab}} = 1050\,\mathrm{MeV}$. For the same reason is the calculated angular range very restricted.

First, we present the comparison to data for the small angular range of the experiment [42]. In figure 7.1, our calculations with the initial state interactions of the pion within the eikonal approximation is shown. Still, our results overestimate the cross section and does not fit the form of the diffraction pattern very well. However, and as already mentioned in the plane-wave case, the small angular range of the experimental data is not conclusive enough to tell if this trend continues to larger scattering angles or not.

A larger angular range is shown in figure 7.2, where we again show the θ_{lab} dependence of the differential cross section. The angular range is restricted by the calculation time of the numerical computer code. This gets longer as the value of the cross section gets smaller due to the minimal contributions of each single integration point. In our case at hand, we stopped the calculation at 75°.

The differential cross sections as functions of $\cos\theta$ and the momentum transfer q are shown in figure 7.3 and in figure 7.4, respectively.

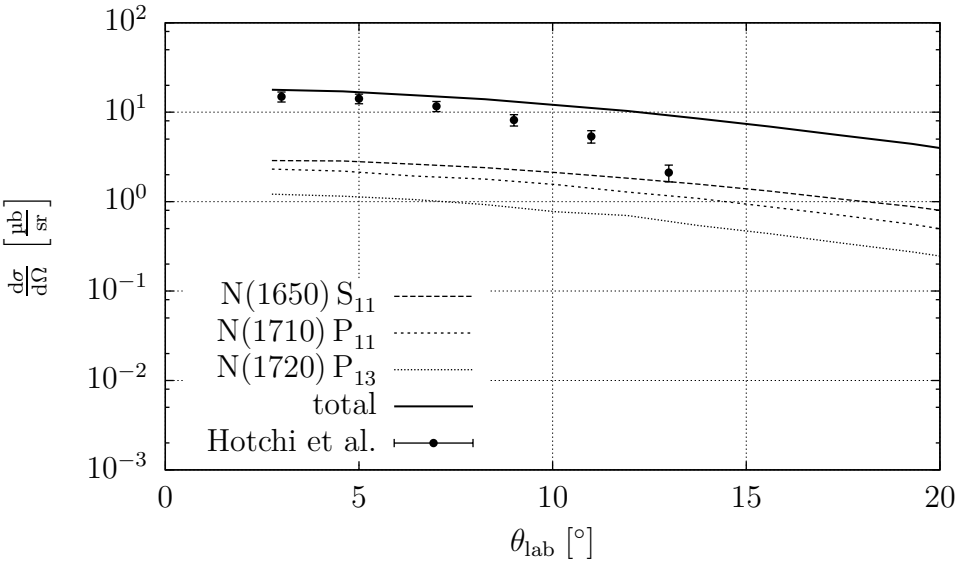

Figure 7.1: The differential cross section for $\pi^+ + {}^{12}\mathrm{C} \rightarrow \mathrm{K}^+ + {}^{12}_{\Lambda}\mathrm{C}$ where the neutron occupies the $p_{3/2}$ orbital, and the Λ the $s_{1/2}$ orbital at a pion incoming momentum of 1050 MeV including the final state interaction within the eikonal approximation.

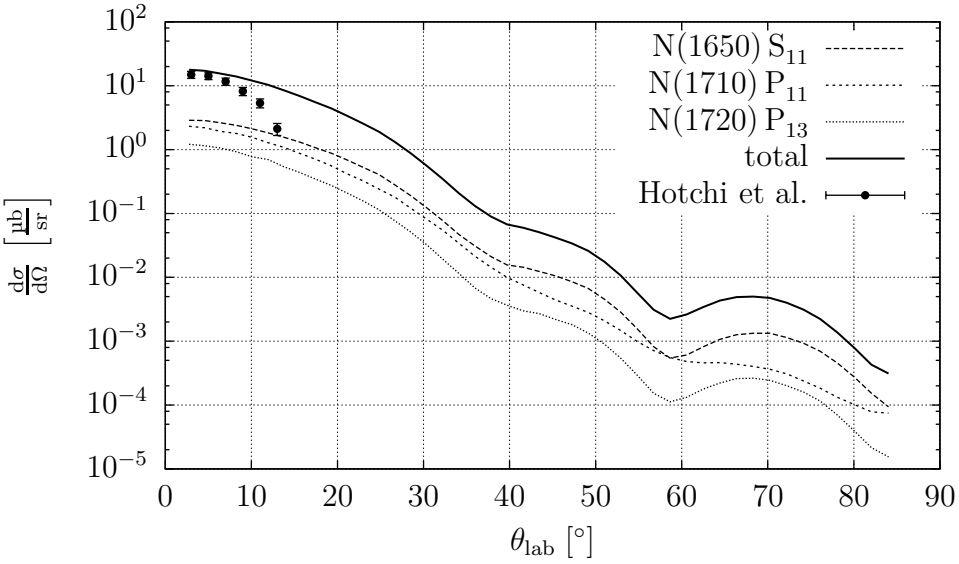

Figure 7.2: The differential cross section for $\pi^+ + {}^{12}\mathrm{C} \rightarrow \mathrm{K}^+ + {}^{12}_{\Lambda}\mathrm{C}$ at a pion incoming momentum of 1050 MeV over the complete angular range from 0° to 180°.

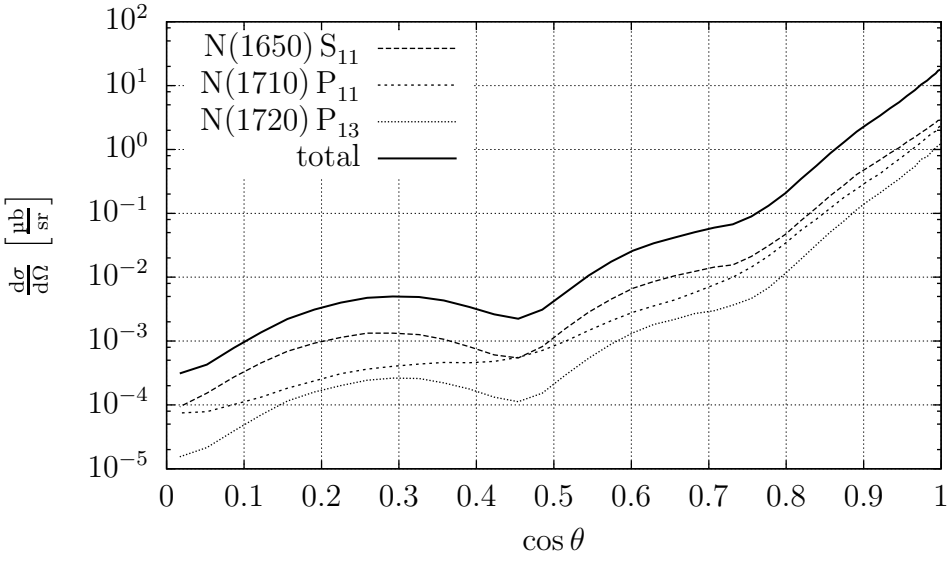

Figure 7.3: The differential cross section for $\pi^+ + {}^{12}\mathrm{C} \rightarrow \mathrm{K}^+ + {}^{12}_{\Lambda}\mathrm{C}$ at a pion incoming momentum of 1050 MeV as a function of $\cos\theta$.

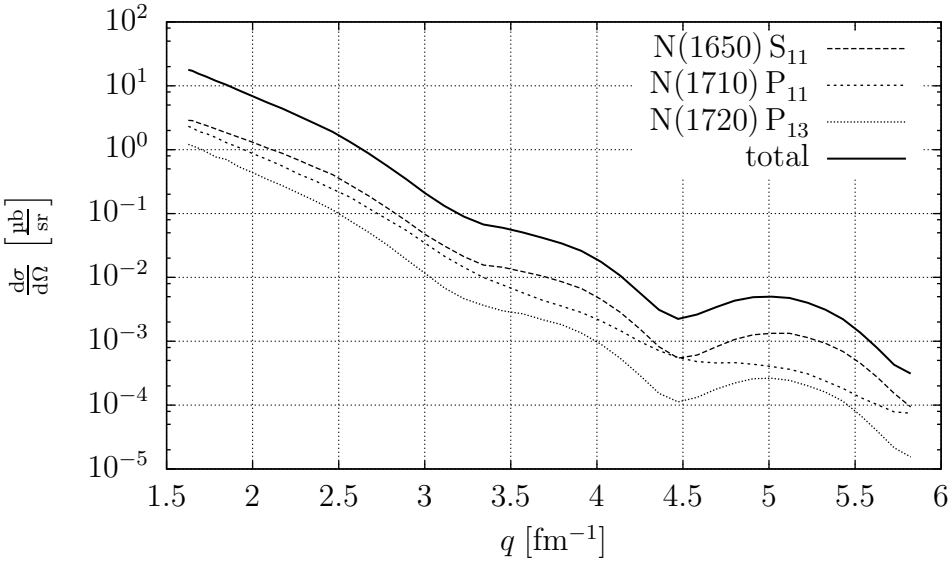

Figure 7.4: The differential cross section for $\pi^+ + {}^{12}\mathrm{C} \rightarrow \mathrm{K}^+ + {}^{12}_{\Lambda}\mathrm{C}$ at a pion incoming momentum of 1050 MeV as a function of the momentum transfer q.

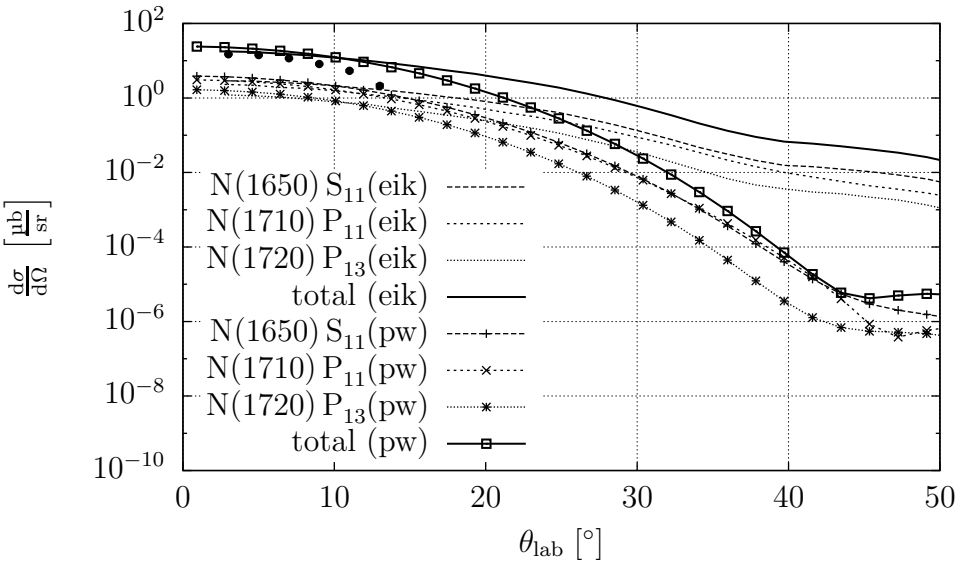

Figure 7.5: The differential cross section for $\pi^+ + {}^{12}\mathrm{C} \rightarrow \mathrm{K}^+ + {}^{12}_{\Lambda}\mathrm{C}$ at a pion incoming momentum of 1050 MeV. Shown is the comparison between the pion plane-wave calculations (lines) and the results for the initial state interactions using the eikonal approximation for the pion (lines with points). The same line-types mark the same resonance contributions.

7.1.1 Comparison to the plane wave results

We compared both results, for the plane wave case and the initial state interactions within the eikonal approximation, in figure 7.5. The differential cross section gets minimally suppressed at forward angles in the eikonal case. However, it does not decrease as fast as the plane wave cross section at larger angles. Furthermore, the diffraction pattern becomes less pronounced which might hint at that the eikonal wave function merely "smears" the pion incoming momentum and therefore the diffraction pattern of the nuclear form factor.

8 Summary and Outlook

In this work we studied the production of particles with a strange quark, kaons and Λ-particles, in pion-nucleus reactions. Thereby, the Λ occupies one of the hypernuclear orbitals and forms a hypernucleus, together with the remaining nucleons. The calculation of the full process involves knowledge about the production of the particles, the internal structure of the nucleus, and the interactions of the incoming and outgoing particles with the nucleus. We reduced the complexity of this description in several steps by disentangling the interaction of the incoming pion with the nucleus by reducing it to a reaction on a single nucleon. Thereby, we considered the nucleus as a superposition of bound nucleons on which this reaction takes place, treating the inter-nucleon interactions completely independently from the main production process. The secondary (elastic) reactions of the incoming and outgoing mesons are separated in a similar fashion to make the process on the nucleus computable.

Chapter 2 was devoted to the nuclear models which are used to calculate the (hyper)nuclear wave functions for our calculations. After a short overview over the available and more sophisticated methods used in involved nuclear calculations, we presented our simplified but realistic approach which, however, is justified by its agreement with experimental data and the results from such involved model calculations. It results in a Dirac equation with a scalar and a vector potential and has the advantage of being much faster to solve for the nucleon wave functions numerically. We presented the details of the used potentials in section 2.4 together with the method to solve the resulting differential equation. Furthermore, we presented the numerical solutions in coordinate space in section 2.4 for the nucleon bound states and in section 2.5 for the Λ bound states. Since our calculations of the reaction cross sections were done in momentum space, we had to Fourier transform these wave functions. We made use of the spherical symmetry of the potential and the resulting decomposition of the wave functions into radial and angular parts. The numerical results of the bound states in momentum space were shown in section 2.6.

The following chapter then dealt with the description of the reaction process itself in terms of a so-called resonance model. First, we described how we disentangle the elementary reaction process from the effective elastic scattering and absorption processes of the mesons. Then we went into the details of our model for the elementary process which deals with the excitation and subsequent decay of nucleon resonances. We take those resonances into account, that have a significant branching into the kaon-Λ channel and whose masses are reachable by our available centre-of-mass energy. The details of these resonances are described in

section 3.2. For our calculations, what we need is an interaction Lagrangian and we presented our choices for the different resonances in section 3.3. Basically, one can choose between pseudovector and pseudoscalar types for the spin-1/2 ones. We settled with the variant favoured by [79, 82], where the pseudoscalar type is used for the odd parity resonance, and the pseudovector one for the even parity resonance. In addition to the pure interaction vertices that are described by the Lagrangian, we have the resonance propagators. Since the resonances are unstable excitations, these propagators are modified by the decay width, which is described in more detail in section 3.4.

The general aspects of reaction theory were recapitulated in chapter 4. Following the approach from [62, 63, 70], we presented the details of the kinematics and the peculiarities for our approach in section 4.1. We then presented a short derivation of the formula for the differential cross section for our process in section 4.2. The final section in that chapter is devoted to the details of the calculation of the scattering matrix elements from the interaction Lagrangians and the resulting Feynman rules. In addition to that, we presented the implications of the various approximations for the meson wave functions.

Before turning to the results of our calculations in chapters 6 and 7, we described the initial and final state interactions of the mesons in chapter 5. These interactions are modelled by a so-called optical potential and we discussed the details about it in section 5.2. Therein, we showed how, in principle, this potential is obtained from an elementary interaction by solving the resulting Schwinger–Dyson equations and iterating the loop diagrams shown in figure 5.1. We also discussed that the optical potential can be parametrised in different ways. And for our calculations, we used a very simple parametrisation, just as we did for the nucleon bound states. This optical potential gives rise to a modified Klein–Gordon equation which can easily be solved numerically for spherically symmetric potentials. That solution was used to verify the validity of this rather simple approach using the elastic scattering data for K^+ and π^+ on ^{12}C at various incoming momenta. We used the fitted parameters to determine their value for our case, since there are no experimental data available for exactly those meson momenta that we investigated. In section 5.4 we then introduced the eikonal approximation since at the relatively high energy, that the pion has in our case, the full solution of the Klein–Gordon equation becomes numerically involved and unstable. Furthermore, we used another approximation for the optical potential, the so-called $t\varrho$-approximation. It connects the potential to the free-space forward scattering amplitude (or, equally, the total elementary cross section) and the nuclear density. The nuclear density, in turn, is approximated by a Gaussian for light nuclei and a Woods–Saxon form for heavier nuclei, but the parameters are fitted in such a way that the nuclear density as calculated from the bound states is reproduced. With all these approximations, the elastic pion scattering data could be very well described, which justifies this approach. The magnitude of the eikonal wave function, which acts as an envelope or modulation to the plane wave, was shown in figure 5.12 and the nuclear distortion effects are clearly visible therein. The last section in that chapter dealt with the Fourier transformation of

the meson wave functions to momentum space for the cross section calculations. We went into the details of how we made use of the partial wave expansion in coordinate space for this transform. The resulting eikonal wave function was then shown in figure 5.15, where we found a visible peak at the on-shell momentum. In contrast to the plane wave approximation, where we would have had a δ-function, it has a finite width which reflects the in-medium changes to the wave function.

Finally, in the last two chapters we presented the results of our calculations on different nuclei. As target nuclei we investigated ^{12}C as a light nucleus and ^{40}Ca as a medium-heavy one. Both are even-even nuclei, that is they consist of an even number of protons and neutrons. On top of that, they are isospin symmetric nuclei consisting of the same number of protons and neutrons. In chapter 6, the results in the plane wave approximation are shown and compared to experimental data from [42]. Section 6.1 dealt with our results for the π^+-^{12}C reaction. We found that within that approximation the data for the n$p_{3/2} \to \Lambda s_{1/2}$ transition can be reproduced apart from an overall factor of $2 \ldots 3$. The other deviation, which is related to the diffraction pattern, suggests that the experimental data decreases faster than our calculations. But the small angular range of the experimental data makes a definite conclusion, if there really is a difference, difficult. The same applies for the least bound Λ orbit in $^{12}_{\Lambda}$C, when we looked at the n$p_{3/2} \to \Lambda p_{3/2}$ transition. Here, the data seems to be a bit better described, but the actual diffraction pattern is hard to compare.

We presented our results for the pion induced strangeness production on ^{40}Ca in section 6.2. Unfortunately, there are no experimental data available to compare to. Furthermore, the Λ bound states are much less well-known than in the Carbon case and the shell structure is less pronounced [43]. However, we presented our results for the n$d_{3/2} \to \Lambda s_{1/2}$ transition in that section, as well as a direct comparison to the reaction on ^{12}C in section 6.3. It can be noted that the structure of the diffraction pattern is slightly different with a shorter period for the heavier nucleus. The absolute magnitude is quite similar in the forward direction and differs by about two orders of magnitude at larger scattering angles, the ^{12}C cross section being larger than the one for ^{40}Ca. This is also reflected in the momentum dependence of the total cross section, which is always higher in the Carbon case for $p_{\text{lab}} \approx 800$ MeV and above. Additionally, the maximum of the momentum distribution of the total cross section is shifted to a slightly smaller value from $p_{\text{lab}} \approx 1000$ MeV in the Carbon case to $p_{\text{lab}} \approx 950$ MeV in the Calcium case.

In the last chapter we presented how the results changed when the initial state interactions of the pion are described within the eikonal approximation. Due to the time-consuming numerical calculations, we restricted ourselves to the n$p_{3/2} \to \Lambda s_{1/2}$ transition in the π^+-^{12}C reaction. As a result, the differential cross section gets suppressed very slightly at forward angles, but is larger compared to the plane wave results at larger scattering angles. Additionally, the diffraction pattern gets less pronounced.

As already mentioned in chapter 7, the calculations including the final state interaction of the kaon are left for future work, since the use of the final state

interactions, as discussed in section 5.3, lead to unexpected numerical problems in the cross section calculation. Similarly, the inclusion of additional t- or u-channel diagrams (in addition to the s-channel resonance exchange depicted in figure 3.5) might further improve the results of the differential cross section. Hopefully this will work for both, the magnitude and the shape of the diffraction pattern.

A Notations

Throughout this thesis we follow the quasi-standard in quantum field theory, see for example [62], that is, we use *natural* units in which

$$\hbar = 1 = c \, .$$

The dimensions of mass, length, energy, and time are related as follows:

$$[\text{mass}] = [\text{energy}] = [\text{length}]^{-1} = [\text{time}]^{-1} \, .$$

We use, however, often *Fermi*: 1 fm $= 10^{-15}$ m for distances, fm^{-1} for momenta, and MeV: 1 MeV $= 10^6$ eV for energies and masses. The units fm and MeV are related to $\hbar c = 1$ by

$$1 = \hbar c = 197.326968 \text{ MeV fm} \, .$$

A.1 Coordinate system and metric

Following the conventions in [63], our space-time coordinates are denoted by the *contravariant* vector

$$x^\mu = (x^0, x^1, x^2, x^3) = (t, \boldsymbol{x}) = (t, x, y, z) \, .$$

A *covariant* vector $x_\mu = (t, -\boldsymbol{x})$ is obtained by multiplying a contravariant vector by the so-called *west-coast* metric,

$$\eta_{\mu\nu} = \eta^{\mu\nu} = \begin{pmatrix} 1 & 0 & 0 & 0 \\ 0 & -1 & 0 & 0 \\ 0 & 0 & -1 & 0 \\ 0 & 0 & 0 & -1 \end{pmatrix} \, .$$

It is in general used to switch from lower to upper indices and vice versa. The inner product is calculated by contracting lower and upper indices using the sum convention

$$\langle x, y \rangle = x \cdot y = x_\mu y^\mu = \eta_{\mu\nu} x^\mu y^\nu \equiv \sum_{\mu=0}^{3} \eta_{\mu\nu} x^\mu y^\nu = x^0 y^0 - \boldsymbol{x} \cdot \boldsymbol{y} \, .$$

The Euclidean scalar product in $\mathbb{R}^3$ is denoted by $\boldsymbol{x} \cdot \boldsymbol{y} = x^i y^i \equiv \sum_{i=1}^{3} x^i y^i$. When we use spherical coordinates for $\boldsymbol{x} \in \mathbb{R}^3$, we usually use the notation $(r, \theta, \varphi) =: (r, \hat{x})$, where θ is the polar angle and φ is the azimuthal angle.

The partial derivative with respect to a contravariant vector gives a covariant vector,

$$\partial_\mu = \frac{\partial}{\partial x^\mu} = \left(\frac{\partial}{\partial t}, \boldsymbol{\nabla}\right) .$$

A.2 Dirac matrices

Working with spin-1/2 particles involves working with the Clifford algebra generated by the Gamma matrices γ^μ,

$$\{\gamma^\mu, \gamma^\nu\} = 2\eta^{\mu\nu} ,$$

which is also called *Dirac* algebra. We use the Dirac representation for their explicit form, which is given by

$$\gamma^0 = \begin{pmatrix} \mathbb{1}_{2\times 2} & 0 \\ 0 & -\mathbb{1}_{2\times 2} \end{pmatrix} , \quad \gamma^i = \begin{pmatrix} 0 & \sigma^i \\ -\sigma^i & 0 \end{pmatrix} ,$$

where σ^i are the 2×2 Pauli matrices, explicitly given by

$$\sigma^1 = \begin{pmatrix} 0 & 1 \\ 1 & 0 \end{pmatrix} , \quad \sigma^2 = \begin{pmatrix} 0 & -\mathrm{i} \\ \mathrm{i} & 0 \end{pmatrix} , \quad \sigma^3 = \begin{pmatrix} 1 & 0 \\ 0 & -1 \end{pmatrix} .$$

The hermitean conjugate of γ^μ is given by

$$(\gamma^\mu)^\dagger = \gamma^0 \gamma^\mu \gamma^0 .$$

The matrix γ^5 is defined by

$$\gamma^5 := \frac{\sqrt{\det \eta}}{4!} \varepsilon_{\mu\nu\alpha\beta} \gamma^\mu \gamma^\nu \gamma^\alpha \gamma^\beta = \mathrm{i}\gamma^0\gamma^1\gamma^2\gamma^3 = \begin{pmatrix} 0 & \mathbb{1}_{2\times 2} \\ \mathbb{1}_{2\times 2} & 0 \end{pmatrix} = \gamma_5$$

with the convention $\varepsilon_{0123} = 1$. It obeys the anticommutation relation $\{\gamma^5, \gamma^\mu\} = 0$ and it is hermitean, $(\gamma^5)^\dagger = \gamma^5$.

The "Dirac slash" is defined as an abbreviation for the contraction of a four-vector x with the Dirac matrices

$$\not{x} := \gamma_\mu x^\mu .$$

A.3 Fourier transformation

We use the convention used in [62] for the Fourier transform $\widehat{f}(k)$ of a function $f(x)$, $k, x \in \mathbb{R}^n$, that is

$$\widehat{f}(k) := \int_{\mathbb{R}^n} \mathrm{d}^n x \; \mathrm{e}^{\mathrm{i}\langle k, x\rangle} \, f(x) ,$$

and the inverse Fourier transformation is given by

$$f(x) = \int\limits_{\mathbb{R}^n} \frac{\mathrm{d}^n k}{(2\pi)^n}\, \mathrm{e}^{-\mathrm{i}\langle k,x\rangle}\, \widehat{f}(k)\ .$$

The general inner product in $\mathbb{R}^n$ is denoted by $\langle\,\cdot\,,\,\cdot\,\rangle$, and in the four-dimensional Minkowski space it is defined by (A.1).

The following useful identity relates the Fourier transform of the constant function 1 to the (n-dimensional) δ-function by

$$\int\limits_{\mathbb{R}^n} \mathrm{d}^n x\ \mathrm{e}^{\mathrm{i}\langle k,x\rangle} = (2\pi)^n \delta^{(n)}(k)\ .$$

B Feynman rules

Here we give a brief overview of the Feynman rules used to calculate the tree diagrams as shown in figure B.1.

B.1 Coordinate space

In the notation used in this thesis, time goes from left to right, and the Feynman rules in coordinate space are:

- For every external meson line, we put the meson wave function $\phi(x)$ for the incoming meson, and $\phi^*(x)$ for the outgoing meson. When using the pseudovector type interactions, we insert the derivatives of these, $\partial_\mu\phi(x)$ and $\partial_\mu\phi^*(x)$, respectively.

- For every external nucleon line, we put the wave function $\psi(x)$ for an incoming particle and the Dirac conjugate $\bar{\psi}(x)$ for an outgoing one.

- At every interaction vertex, the factor Γ is inserted as deduced from the interaction Lagrangians and we have to integrate over the position four-vector:

$$\Gamma \int \mathrm{d}^4x \ .$$

- The spin-1/2 resonance propagator G_R is given by (4.10)

$$G_\mathrm{R}(x,y) = \mathrm{i}\int\limits_{\mathbb{R}^4} \frac{\mathrm{d}^4p}{(2\pi)^4} \frac{\not{p} + m_\mathrm{R}}{p^2 - m_\mathrm{R}^2 + \mathrm{i}\epsilon}\, \mathrm{e}^{-\mathrm{i}p\,\cdot\,(x-y)} \ .$$

- The spin-3/2 resonance propagator G_R is given by

$$G_\mathrm{R}^{\mu\nu}(x,y) = -\mathrm{i}\int\limits_{\mathbb{R}^4} \frac{\mathrm{d}^4p}{(2\pi)^4} \frac{\not{p} + m_\mathrm{R}}{p^2 - m_\mathrm{R}^2 + \mathrm{i}\epsilon} P^{\mu\nu}\, \mathrm{e}^{-\mathrm{i}p\,\cdot\,(x-y)} \ ,$$

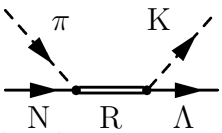

Figure B.1: Tree diagram for the elementary process of pion-induced strangeness production via resonance excitation and decay on a single nucleon.

with the spin-3/2 projector $P^{\mu\nu}$ (3.7)

$$P^{\mu\nu} = \eta^{\mu\nu} - \frac{1}{3}\gamma^\mu\gamma^\nu - \frac{2}{3m^2}p^\mu p^\nu + \frac{1}{3m}\left(p^\mu\gamma^\nu - p^\nu\gamma^\mu\right) \ .$$

The T-matrix is then given by the integral over all position four-vectors x and y.

The interaction vertices in coordinate space for the three resonances are listed in table B.1

J^P	type	$\Gamma^{(\mu)}$
$1/2^+$	pseudoscalar	$-g\gamma^5$
$1/2^+$	pseudovector	$\mathrm{i}g\gamma^\mu\gamma^5$
$1/2^-$	pseudoscalar	$\mathrm{i}g$
$1/2^-$	pseudovector	$-g\gamma^\mu$
$3/2^+$	conventional	$\mathrm{i}g$

Table B.1: Vertex factors in coordinate space as given from the interaction Lagrangians.

B.2 Momentum space

The Feynman rules in momentum space are:

- For every external meson line, we put the Fourier transform of the meson wave function, $\widehat{\phi}(p)$ for the incoming meson and $\widehat{\phi}^*(p)$ for the outgoing meson. When using the pseudovector Lagrangians, we have to insert additional factors of $-\mathrm{i}k_\mu$, where k is the respective meson momentum.
- For every external nucleon line, we put the Fourier transform of the wave function, $\psi(p)$ for an incoming particle and the Dirac conjugate $\bar{\psi}(p)$ for an outgoing one.
- At every interaction vertex, the factors Γ_1 and Γ_2, translated to momentum space, are inserted as deduced from the interaction Lagrangians.
- The spin-1/2 resonance propagator G_R is given by (3.5)

$$G_\mathrm{R} = \mathrm{i}\frac{\not{p} + m}{p^2 - m^2 + \mathrm{i}\epsilon} \ .$$

- The spin-3/2 resonance propagator G_R is given by (3.8)

$$G_\mathrm{R}^{\mu\nu} = -\mathrm{i}\frac{\not{p} + m}{p^2 - m^2 + \mathrm{i}\epsilon}P^{\mu\nu} \ .$$

Finally, the T-matrix is then given by the integrating over all momenta which are not fixed from the outside or by momentum conservation.

C Symmetries of the interaction Lagrangian

We express all reactions in this thesis starting from amplitudes, which means that all the contributions of the various resonances interfere with each other. For a correct calculation we have, therefore, to take care of the correct interference terms which can be deduced from the symmetries of our interaction Lagrangian.

Since the Lagrangian should be invariant under all Lorentz transformations, it follows that it has to be in particular invariant under the following discrete symmetries:

- parity,
- time reversal, and
- charge conjugation.

C.1 Parity

The parity transformation is defined by $\boldsymbol{x} \mapsto -\boldsymbol{x}$, which implies for the spinor wave function [62]

$$\begin{aligned} P\psi(t,\boldsymbol{x})P^{-1} &= \eta_a \gamma^0 \psi(t,-\boldsymbol{x}) \ , \\ P\bar{\psi}(t,\boldsymbol{x})P^{-1} &= \eta_a^* \bar{\psi}(t,-\boldsymbol{x})\gamma^0 \ , \end{aligned}$$

where $|\eta_a|^2 = 1$.

The pion wave function changes its sign under the parity transformation, that is $\phi_\pi \mapsto -\phi_\pi$. Furthermore, only the space-like components of the partial derivative ∂_μ change their sign:

$$\begin{aligned} \partial_0 &\mapsto \partial_0 \ , \\ \partial_i &\mapsto -\partial_i \ , \quad i \in \{1,2,3\} \ . \end{aligned}$$

Putting these together, we find for the bilinears

$$\begin{aligned} \bar{\psi}\psi &\mapsto \bar{\psi}\psi \ , \\ \bar{\psi}\gamma^\mu\psi &\mapsto \pm\bar{\psi}\gamma^\mu\psi \ , \\ \mathrm{i}\bar{\psi}\gamma^5\psi &\mapsto -\mathrm{i}\bar{\psi}\gamma^5\psi \ , \\ \bar{\psi}\gamma^\mu\gamma^5\psi &\mapsto \mp\bar{\psi}\gamma^\mu\gamma^5\psi \ , \end{aligned}$$

where the upper sign holds for $\mu = 0$ and the lower one for $\mu \in \{1,2,3\}$.

C.2 Time reversal

The time reversal operator acts on the wave functions as

$$T\psi(t,\boldsymbol{x})T^{-1} = (-\gamma^1\gamma^3)\psi(-t,\boldsymbol{x})$$

and we get, consequently, for the Dirac conjugate

$$T\bar{\psi}(t,\boldsymbol{x})T^{-1} = \bar{\psi}(-t,\boldsymbol{x})\gamma^1\gamma^3 \ .$$

The partial derivative changes its sign only in the time component,

$$\begin{aligned}\partial_0 &\mapsto -\partial_0 \ , \\ \partial_i &\mapsto \partial_i \ , \quad i \in \{1,2,3\} \ .\end{aligned}$$

From [63, p.127, (15.132)], the charged components of the pion are interchanged and all of them get a negative sign, but there is a phase factor remaining:

$$\begin{aligned}\phi_{\pi^\pm} &\mapsto \pm\phi_{\pi^\mp} \ , \\ \phi_{\pi^0} &\mapsto \pm\phi_{\pi^0} \ .\end{aligned}$$

Thus, the combination $\boldsymbol{\tau}\cdot\boldsymbol{\phi}$ would map to $\pm(\boldsymbol{\tau}\cdot\boldsymbol{\phi})^t$. Since we also have to take the complex conjugate of all (complex) numbers, τ_2 becomes τ_2^t, and therefore

$$\boldsymbol{\tau}\cdot\boldsymbol{\phi} \mapsto \pm\boldsymbol{\tau}\cdot\boldsymbol{\phi} \ .$$

In analogy to the parity transformation, the bilinears transform as follows:

$$\begin{aligned}\bar{\psi}\psi &\mapsto \bar{\psi}\psi \ , \\ \bar{\psi}\gamma^\mu\psi &\mapsto \pm\bar{\psi}\gamma^\mu\psi \ , \\ \mathrm{i}\bar{\psi}\gamma^5\psi &\mapsto -\mathrm{i}\bar{\psi}\gamma^5\psi \ , \\ \bar{\psi}\gamma^\mu\gamma^5\psi &\mapsto \pm\bar{\psi}\gamma^\mu\gamma^5\psi \ ,\end{aligned}$$

where the upper sign holds for $\mu = 0$ and the lower one for $\mu \in \{1,2,3\}$.

C.3 Charge conjugation

This operator acts on the wave functions via γ^2:

$$C\psi(x)C^{-1} = -\mathrm{i}\gamma^2\psi^*(x) = (-\mathrm{i}\bar{\psi}\gamma^0\gamma^2)^t \ ,$$

from which the action on $\bar{\psi}$ can be seen to be

$$C\bar{\psi}C^{-1} = (-\mathrm{i}\gamma^0\gamma^2\psi)^t \ .$$

The resulting transformations of the bilinear terms are then given by

$$\begin{aligned}\bar{\psi}\psi &\mapsto \bar{\psi}\psi \ , \\ \bar{\psi}\gamma^\mu\psi &\mapsto -\bar{\psi}\gamma^\mu\psi \ , \\ \mathrm{i}\bar{\psi}\gamma^5\psi &\mapsto \mathrm{i}\bar{\psi}\gamma^5\psi \ , \\ \bar{\psi}\gamma^\mu\gamma^5\psi &\mapsto \bar{\psi}\gamma^\mu\gamma^5\psi \ ,\end{aligned}$$

C.4 Summary

We can now compose a table for the discrete symmetries, which results in

	$\bar{\psi}\psi$	$\bar{\psi}\gamma^\mu\psi$	$\mathrm{i}\bar{\psi}\gamma^5\psi$	$\bar{\psi}\gamma^\mu\gamma^5\psi$	∂_μ	$\boldsymbol{\tau}\cdot\boldsymbol{\phi}$
P	$+1$	±1	-1	∓1	±1	-1
T	$+1$	±1	-1	±1	∓1	±1
C	$+1$	-1	$+1$	$+1$	$+1$	$+1$

C.5 Pseudovector spin-1/2 resonances

The ansatz for the pseudovector Lagrangian for the pion-nucleus-resonance vertex is given by

$$\mathcal{L} = \alpha\bar{\psi}_\mathrm{R}\boldsymbol{\tau}\cdot\partial_\mu\boldsymbol{\phi}_\pi\gamma^\mu\psi_\mathrm{N} + \text{h. c.}\,, \tag{C.1}$$

where α is the (complex) coupling constant and $\boldsymbol{\tau}$ are the isospin Pauli matrices. We absorb the isospin multiplication into a factor, which is $\sqrt{2}$ at the πNR vertex and one at the RKΛ vertex [127].

To check the discrete symmetries, we start with the first term of (C.1).

C.5.1 Parity

We know that $\bar{\psi}\gamma^\mu\psi$ and ∂_μ change their sign for $\mu \in \{1,2,3\}$ and not for $\mu = 0$. Taking into account the sign change of the pion wave function, we find that the behaviour of this term is determined by the parity of the resonance:

$$\bar{\psi}_\mathrm{R}\partial_\mu\phi_\pi\gamma^\mu\psi_\mathrm{N} \mapsto -P_\mathrm{R}\bar{\psi}_\mathrm{R}\partial_\mu\phi_\pi\gamma^\mu\psi_\mathrm{N}\,.$$

Applying the same arguments to the hermitean conjugate term of (C.1), we find that the Lagrangian is invariant under parity transformations if the resonance has odd parity.

For even parity resonances the ansatz for the Lagrangian is

$$\mathcal{L} = \alpha\bar{\psi}_\mathrm{R}\boldsymbol{\tau}\cdot\partial_\mu\boldsymbol{\phi}_\pi\gamma^\mu\gamma^5\psi_\mathrm{N} + \text{h. c.}\,,$$

where the sign change of $\bar{\psi}\gamma^\mu\gamma^5\psi$ compensates that of the partial derivatives.

C.5.2 Time reversal

Since we are free to choose the phase factor of the combination $\boldsymbol{\tau}\cdot\boldsymbol{\phi}$, time reversal invariance can always be satisfied and leads to no additional constraints on the coupling.

C.5.3 Charge conjugation

The transformations under charge conjugation require a little more investigation since they interchange the two spinor wave functions of the resonance and the nucleon or Λ. Taking that into account, we get reality conditions for the coupling constant. While the partial derivatives are not affected by charge conjugation, the charged pions get interchanged.

This means, (C.1) transforms as

$$\bar{\psi}_{\mathrm{R}} \partial_\mu \phi_\pi \gamma^\mu \psi_{\mathrm{N}} \mapsto -\bar{\psi}_{\mathrm{N}} \partial_\mu \phi_\pi \gamma^\mu \psi_{\mathrm{R}} \ ,$$

and the Lagrangian for even-parity resonances behaves as

$$\bar{\psi}_{\mathrm{R}} \partial_\mu \phi_\pi \gamma^\mu \gamma^5 \psi_{\mathrm{N}} \mapsto \bar{\psi}_{\mathrm{N}} \partial_\mu \phi_\pi \gamma^\mu \gamma^5 \psi_{\mathrm{R}} \ .$$

To be invariant under charge conjugation, these terms have to be equal to the hermitean conjugate term in the Lagrangian. For odd-parity resonances this means that $-\alpha = \alpha^*$, and for even-parity ones we have $\alpha = \alpha^*$. We introduce the real coupling constant by $\alpha = \mathrm{i}g$ in the first and $\alpha = g$ in the second case, with $g \in \mathbb{R}$.

Now we have

$$\mathcal{L} = g \bar{\psi}_{\mathrm{R}} \partial_\mu \phi_\pi \gamma^\mu \left\{ \begin{array}{c} \mathrm{i} \\ \gamma^5 \end{array} \right\} \psi_{\mathrm{N}} + \mathrm{h.\ c.} \ ,$$

with the upper factor for odd-parity and the lower one for even-parity resonances. Written this way, it is invariant under parity and charge conjugation and it is hermitean by construction.

C.6 Pseudoscalar spin-1/2 resonances

The ansatz for the pseudoscalar Lagrangian for the pion-nucleus-resonance vertex is given by

$$\mathcal{L} = \alpha \bar{\psi}_{\mathrm{R}} \boldsymbol{\tau} \cdot \boldsymbol{\phi}_\pi \psi_{\mathrm{N}} + \mathrm{h.\ c.} \ , \tag{C.2}$$

where the notation is the same as in the previous section. The isospin multiplication is again absorbed into a single factor.

C.6.1 Parity

Since there are no derivatives or gamma matrices, the first term of (C.2) changes its sign because of the pion wave function, and a second sign change may come from the parity of the resonance:

$$\bar{\psi}_{\mathrm{R}} \phi_\pi \psi_{\mathrm{N}} \mapsto -P_{\mathrm{R}} \bar{\psi}_{\mathrm{R}} \phi_\pi \psi_{\mathrm{N}} \ .$$

And, again, this shows that (C.2) is invariant if the resonance has odd parity.

For even parity resonances, we introduce an additional γ^5 into the Lagrangian above, which restores parity invariance

$$\mathcal{L} = \alpha \bar{\psi}_{\mathrm{R}} \boldsymbol{\tau} \cdot \boldsymbol{\phi}_\pi \gamma^5 \psi_{\mathrm{N}} + \mathrm{h.\ c.} \ . \tag{C.3}$$

C.6.2 Time reversal

Since we are free to choose the phase factor of the combination $\boldsymbol{\tau} \cdot \boldsymbol{\phi}$, time reversal invariance can always be satisfied and, again, this leads to no additional constraints for the coupling.

C.6.3 Charge conjugation

Invariance under charge conjugation gives again reality conditions for the complex coupling α. In particular the first term in (C.2) behaves as

$$\bar{\psi}_{\mathrm{R}} \phi_\pi \psi_{\mathrm{N}} \mapsto \bar{\psi}_{\mathrm{N}} \phi_\pi \psi_{\mathrm{R}} \ ,$$

where only the spinor wave functions are interchanged. The same holds for (C.3), but there the hermitean conjugate changes the sign of α^*. In the first case we have therefore $\alpha = \alpha^*$ and in the second case it is $\alpha = -\alpha^*$.

Put together, our parity and charge conjugation invariant pseudoscalar Lagrangian is

$$\mathcal{L} = g \bar{\psi}_{\mathrm{R}} \phi_\pi \left\{ \begin{array}{c} \mathbb{1} \\ \mathrm{i}\gamma^5 \end{array} \right\} \psi_{\mathrm{N}} + \mathrm{h.\ c.} \ ,$$

and again the upper factor is for odd-parity and the lower one for even-parity resonances.

D Solution of the mean-field Dirac equation

The calculation of the nuclear bound states is based on the mean-field Dirac equation

$$[\gamma^\mu(\mathrm{i}\partial_\mu - \Sigma_\mu) - (m - \Sigma^\mathrm{s})]\,\psi = 0\,, \tag{2.5}$$

which can be simplified for spherically symmetric nuclei to

$$\left(\mathrm{i}\not{\partial} - m - \gamma^0 V^0 - V^\mathrm{s}\right)\psi = 0\,.$$

It can be viewed as the equation of motion from the Lagrangian density

$$\mathcal{L} = \bar{\psi}\left(\mathrm{i}\not{\partial} - m - \gamma^0 V^0 - V^\mathrm{s}\right)\psi\,.$$

The canonical momentum is given by $\pi = \mathrm{i}\bar{\psi}\gamma^0 = \mathrm{i}\psi^\dagger$, and following [62], the Hamiltonian is given by

$$H = \int \mathrm{d}^3x\,\bar{\psi}\left(\mathrm{i}\gamma^i\partial_i + \gamma^0 V^0 + m + V^\mathrm{s}\right)\psi = \int \mathrm{d}^3x\,\psi^\dagger\left(\mathrm{i}\gamma^0\gamma^i\partial_i + V^0 + \gamma^0(m + V^\mathrm{s})\right)\psi$$

with the single-particle Hamilton density

$$h = \mathrm{i}\gamma^0\gamma^i\partial_i + V^0 + \gamma^0(m + V^\mathrm{s}) = -\mathrm{i}\boldsymbol{\alpha}\cdot\boldsymbol{\nabla} + V^0 + \gamma^0(m + V^\mathrm{s})\,, \tag{D.1}$$

such that

$$h\psi = \varepsilon\psi \tag{D.2}$$

with the single-particle energy ε.

The solution to (D.2) with the Hamiltonian (D.1) are then the bound states. They can be separated into an angular and a radial part with the ansatz

$$\psi(\boldsymbol{x}) = \begin{pmatrix} f_{n,j}(r)\,\mathcal{Y}_{\ell s}^{jm_j}(\hat{x}) \\ -\mathrm{i}g_{n,j}(r)\,\mathcal{Y}_{\ell' s}^{jm_j}(\hat{x}) \end{pmatrix}$$

with the spinor-spherical harmonics

$$\mathcal{Y}_{\ell s}^{jm_j}(\hat{x}) = \sum_{m_\ell, m_s} \langle \ell, m_\ell, s, m_s \,|\, j, m_j\rangle\, Y_{\ell m_\ell}(\hat{x})\chi_{s,m_s}\,. \tag{2.10}$$

The upper and lower components, $f(r)$ and $g(r)$ respectively, then satisfy the coupled equations

$$\left(V^0 + V^\mathrm{s} + m - \varepsilon\right) f\,\mathcal{Y}_{\ell s}^{jm_j} = \boldsymbol{\sigma}\cdot\boldsymbol{\nabla} g\,\mathcal{Y}_{\ell' s}^{jm_j}\,, \tag{D.3}$$

$$\left(V^0 - V^\mathrm{s} - m - \varepsilon\right) g\,\mathcal{Y}_{\ell' s}^{jm_j} = -\boldsymbol{\sigma}\cdot\boldsymbol{\nabla} f\,\mathcal{Y}_{\ell s}^{jm_j}\,. \tag{D.4}$$

Eliminating $g(r)$ from (D.3) with the help of (D.4) then leads to

$$\left[(V^0-\varepsilon)^2-(m+V^{\mathrm{s}})^2-\frac{\boldsymbol{\sigma}\cdot\boldsymbol{\nabla}(V^0-V^{\mathrm{s}})}{V^0-m-V^{\mathrm{s}}-\varepsilon}\boldsymbol{\sigma}\cdot\boldsymbol{\nabla}+\triangle\right]f(r)\,\mathcal{Y}_{\ell s}^{jm_j}(\hat{x})=0\,. \quad \text{(D.5)}$$

For the evaluation of the $\boldsymbol{\sigma}\cdot\boldsymbol{\nabla}$-terms, the following identity [128–130] is useful[1]:

$$\begin{aligned}\boldsymbol{\sigma}\cdot\boldsymbol{\nabla}fY&=(\boldsymbol{\sigma}\cdot\hat{\boldsymbol{x}})(\boldsymbol{\sigma}\cdot\hat{\boldsymbol{x}})\boldsymbol{\sigma}\cdot\boldsymbol{\nabla}fY\\&=\frac{1}{r^2}(\boldsymbol{\sigma}\cdot\boldsymbol{x})\left[\boldsymbol{x}\cdot\boldsymbol{\nabla}+\mathrm{i}\boldsymbol{\sigma}\cdot(\boldsymbol{x}\times\boldsymbol{\nabla})\right]fY\\&=\frac{1}{r^2}(\boldsymbol{\sigma}\cdot\boldsymbol{x})\left[\boldsymbol{x}\cdot\boldsymbol{\nabla}-\boldsymbol{\sigma}\cdot\boldsymbol{L}\right]fY\,. \quad \text{(D.6)}\end{aligned}$$

The eigenvalues of $\boldsymbol{\sigma}\cdot\boldsymbol{L}$ are given by

$$\boldsymbol{\sigma}\cdot\boldsymbol{L}\,\mathcal{Y}_{\ell s}^{jm_j}=-1\pm\left(j+\frac{1}{2}\right)\mathcal{Y}_{\ell s}^{jm_j}\,,$$

where $j=\ell\pm1/2$, and (D.6) can be written as

$$\boldsymbol{\sigma}\cdot\boldsymbol{\nabla}fY=\frac{1}{r^2}(\boldsymbol{\sigma}\cdot\boldsymbol{x})\left[r\frac{\partial}{\partial r}-\left(-1\pm\left(j+\frac{1}{2}\right)\right)\right]fY\,.$$

This fully separates the radial and angular parts and (D.5) leads to a differential equation for $f(r)$:

$$\begin{aligned}\Bigg[\frac{1}{r}\frac{\partial^2}{\partial r^2}r-\frac{\ell(\ell+1)}{r^2}+(V^0-\varepsilon)^2-(m+V^{\mathrm{s}})^2\\-\frac{1}{V^0-m-V^{\mathrm{s}}-\varepsilon}\frac{\partial(V^0-V^{\mathrm{s}})}{\partial r}\left(\frac{\partial}{\partial r}+\frac{1\mp(j+1/2)}{r}\right)\Bigg]f(r)=0\,.\end{aligned}$$

This equation can easily be solved numerically, and by using (D.3) and (D.4) we obtain $g(r)$ and hence $\psi(\boldsymbol{x})$.

[1] We use the abbreviation $\hat{\boldsymbol{x}}:=\boldsymbol{x}/r$ with $r=|\boldsymbol{x}|$.

E Matrix elements and cross sections

E.1 Detailed discussion of the matrix element calculation

Our choice for calculating the scattering amplitude(s) and cross section(s) is a Monte-Carlo integration of the integrand (5.30). As already indicated in section 5.6.3, we want to simplify this expression as far as possible by analytical methods for faster numerical evaluation. We will calculate (5.32) in more detail, as well as determine the variables $c_1, \ldots, c_4'$ explicitly.

As discussed, (5.32) gives four terms mixing the upper and lower components of the Λ and nucleon wave function. The first term is

$$\begin{aligned} M_1^a &:= f_\Lambda f_\mathrm{N}(c_1 + c_1' k_\mathrm{K}^0)\, \mathcal{Y}_\Lambda^\dagger\, \mathcal{Y}_\mathrm{N} \\ &= f_\Lambda f_\mathrm{N}(c_1 + c_1' k_\mathrm{K}^0) \\ &\quad \times \sum_{m,m'} \left\langle \ell, m_j - m, \frac{1}{2}, m \,\middle|\, j, m_j \right\rangle \left\langle L, m_J - m', \frac{1}{2}, m' \,\middle|\, J, m_J \right\rangle \\ &\quad\quad \times Y^*_{\ell, m_j - m} Y_{L, m_J - m'} \chi^\dagger_{1/2,m} \chi_{1/2,m'} \ , \end{aligned} \tag{E.1}$$

where we used again the single indices Λ and N to denote all the indices and arguments of the wave functions for the Λ and the nucleon, respectively. Written explicitly, we used them as follows:

$$\begin{aligned} f_\Lambda &:= f_{n,j}(|\boldsymbol{k}_\Lambda|) \ , & \mathcal{Y}_\Lambda &:= \mathcal{Y}_{\ell s}^{j m_j}(\hat{k}_\Lambda) \ , \\ f_\mathrm{N} &:= f_{N,J}(|\boldsymbol{k}_\mathrm{N}|) \ , & \mathcal{Y}_\mathrm{N} &:= \mathcal{Y}_{LS}^{J m_J}(\hat{k}_\mathrm{N}) \ . \end{aligned}$$

Furthermore, we used lower case letters n, ℓ, s, j, m_j for the Λ indices and upper case letters N, L, S, J, and m_J for the nucleon indices. The arguments of the spherical harmonics are $Y^*_{\ell,\ldots} = Y^*_{\ell,\ldots}(\hat{k}_\Lambda)$ and $Y_{L,\ldots} = Y_{L,\ldots}(\hat{k}_\mathrm{N})$, respectively.

The orthogonality relation for the two-dimensional spinors in the last line of (E.1) gives the constraint $m = m'$ and we are left with

$$\begin{aligned} M_1^a &= f_\Lambda f_\mathrm{N}(c_1 + c_1' k_\mathrm{K}^0) \\ &\quad \times \sum_{m} \left\langle \ell, m_j - m, \frac{1}{2}, m \,\middle|\, j, m_j \right\rangle \left\langle L, m_J - m, \frac{1}{2}, m \,\middle|\, J, m_J \right\rangle Y^*_{\ell, m_j - m} Y_{L, m_J - m} \ . \end{aligned} \tag{E.2}$$

The mixed terms in (5.32) involve the angular momentum algebra because of the $\boldsymbol{\sigma}\cdot\boldsymbol{k}$ term. This term acts between the two-dimensional spinors and we can use $\sigma_x = s_+ + s_-$ and $\sigma_y = -\mathrm{i}(s_+ - s_-)$, where s_+ and s_- are the spin-1/2 ladder operators. They act on the spinor components as

$$s_\pm \chi_{s,m} = \sqrt{(s \mp m)(s + 1 \pm m)}\chi_{s,m\pm1}$$

and $\sigma_z\chi_{s,m} = 2s_z\chi_{s,m} = 2m\chi_{s,m}$. Hence, we arrive at

$$\begin{aligned}\chi^\dagger_{1/2,m}(\boldsymbol{\sigma}\cdot\boldsymbol{k})\chi_{1/2,m'} = &\sqrt{\left(\frac{1}{2} - m'\right)\left(\frac{3}{2} + m'\right)}(k_x - \mathrm{i}k_y)\delta_{m,m'+1} \\ &+ \sqrt{\left(\frac{1}{2} + m'\right)\left(\frac{3}{2} - m'\right)}(k_x + \mathrm{i}k_y)\delta_{m,m'-1} + 2mk_z\delta_{m,m'} \ .\end{aligned}$$

The x-, y-, and z-directions of the momentum vector $\boldsymbol{k}$ are determined by the incoming pion momentum $\boldsymbol{k}_\pi$, which is taken to be in the z-direction: $\boldsymbol{k}_\pi = (0, 0, |\boldsymbol{k}_\pi|)$. This gives for the second term in (5.32) the following expression

$$\begin{aligned}M_1^b &:= \mathrm{i}c_1' f_\Lambda g_\mathrm{N}\, \mathcal{Y}^\dagger_\Lambda(\boldsymbol{\sigma}\cdot\boldsymbol{k}_\mathrm{K})\, \mathcal{Y}_\mathrm{N} \\ &= \mathrm{i}c_1' f_\Lambda g_\mathrm{N} \sum_m \left\langle L', m_J - m, \frac{1}{2}, m \,\middle|\, J, m_J \right\rangle Y_{L',m_J-m} \\ &\quad \times \Bigg[k_x \left\langle \ell, m_j - m - 1, \frac{1}{2}, m + 1 \,\middle|\, j, m_j \right\rangle Y^*_{\ell,m_j-m-1}\sqrt{\left(\frac{1}{2} - m\right)\left(\frac{3}{2} + m\right)} \\ &\qquad + k_y \left\langle \ell, m_j - m + 1, \frac{1}{2}, m - 1 \,\middle|\, j, m_j \right\rangle Y^*_{\ell,m_j-m+1}\sqrt{\left(\frac{1}{2} + m\right)\left(\frac{3}{2} - m\right)} \\ &\qquad + 2mk_z \left\langle \ell, m_j - m, \frac{1}{2}, m | j, m_j \right\rangle Y^*_{\ell,m_j-m} \Bigg] \ . \end{aligned} \tag{E.3}$$

The third part of M_1 can be expressed analogously to (E.3), substituting f_Λ by g_Λ, g_N by f_N, and i by $-$i. And for the fourth part of (5.32) we get the same expression as (E.2) but we have to substitute f by the respective g, and c_1 by $-c_1$.

We can use the same reasoning for the parts $M_2, \ldots, M_4$ of (5.30), where F_N gives rise to factors ζ_N and ζ'_N instead of f_N and g_N, respectively. Similarly, the occurrence of $\bar{F}_\Lambda$ in M_3 and M_4 leads to factors ζ_Λ and ζ'_Λ, using the fact that these are real functions.

We now define four functions $F_1, \ldots, F_4$ as follows:

$$\begin{aligned}
F_1 &:= (c_1 + c_1' k_{\mathrm{K}}^0) f_\Lambda f_{\mathrm{N}} + (c_2 + c_2' k_{\mathrm{K}}^0) f_\Lambda \zeta_{\mathrm{N}} \\
&\quad + (c_3 + c_3' k_{\mathrm{K}}^0) \zeta_\Lambda f_{\mathrm{N}} + (c_4 + c_4' k_{\mathrm{K}}^0) \zeta_\Lambda \zeta_{\mathrm{N}} \,, \\
F_2 &:= \mathrm{i} \left(c_1' f_\Lambda g_{\mathrm{N}} + c_2' f_\Lambda \zeta_{\mathrm{N}}' + c_3' \zeta_\Lambda g_{\mathrm{N}} + c_4' \zeta_\Lambda \zeta_{\mathrm{N}}' \right) \,, \\
F_3 &:= -\mathrm{i} \left(c_1' g_\Lambda f_{\mathrm{N}} + c_2' g_\Lambda \zeta_{\mathrm{N}} + c_3' \zeta_\Lambda' f_{\mathrm{N}} + c_4' \zeta_\Lambda' \zeta_{\mathrm{N}} \right) \,, \\
F_4 &:= (-c_1 + c_1' k_{\mathrm{K}}^0) g_\Lambda g_{\mathrm{N}} + (-c_2 + c_2' k_{\mathrm{K}}^0) g_\Lambda \zeta_{\mathrm{N}}' \\
&\quad + (-c_3 + c_3' k_{\mathrm{K}}^0) \zeta_\Lambda' g_{\mathrm{N}} + (-c_4 + c_4' k_{\mathrm{K}}^0) \zeta_\Lambda' \zeta_{\mathrm{N}}' \,.
\end{aligned}$$

With these definitions, we can now write down M in terms of $c_1, \ldots, c_4'$ and the radial wave function parts f, g, ζ, and ζ', together with their respective angular parts, as

$$\begin{aligned}
M_1 = {} & F_1 \sum_m \left\langle \ell, m_j - m, \frac{1}{2}, m \,\middle|\, j, m_j \right\rangle \left\langle L, m_J - m, \frac{1}{2}, m \,\middle|\, J, m_J \right\rangle Y^*_{\ell, m_j - m} Y_{L, m_J - m} \\
& + F_2 \sum_m \left\langle L', m_J - m, \frac{1}{2}, m \,\middle|\, J, m_J \right\rangle Y_{L', m_J - m} \\
& \quad \times \Bigg[k_x \left\langle \ell, m_j - m - 1, \frac{1}{2}, m + 1 \,\middle|\, j, m_j \right\rangle Y^*_{\ell, m_j - m - 1} \sqrt{\left(\frac{1}{2} - m\right)\left(\frac{3}{2} + m\right)} \\
& \qquad + k_y \left\langle \ell, m_j - m + 1, \frac{1}{2}, m - 1 \,\middle|\, j, m_j \right\rangle Y^*_{\ell, m_j - m + 1} \sqrt{\left(\frac{1}{2} + m\right)\left(\frac{3}{2} - m\right)} \\
& \qquad + 2 m k_z \left\langle \ell, m_j - m, \frac{1}{2}, m \middle| j, m_j \right\rangle Y^*_{\ell, m_j - m} \Bigg] \\
& + F_3 \sum_m \left\langle L, m_J - m, \frac{1}{2}, m \,\middle|\, J, m_J \right\rangle Y_{L, m_J - m} \times [\ell \mapsto \ell'] \\
& + F_4 \sum_m \left\langle \ell', m_j - m, \frac{1}{2}, m \,\middle|\, j, m_j \right\rangle \left\langle L', m_J - m, \frac{1}{2}, m \,\middle|\, J, m_J \right\rangle Y^*_{\ell', m_j - m} Y_{L', m_J - m} \,.
\end{aligned} \tag{E.4}$$

E.2 The variables $c_1, \ldots, c_4'$

With the form (E.4) for the integrand of the matrix element, all we need is the explicit form of the variables $c_1, \ldots, c_4'$ from the interaction Lagrangians. Since we have different possibilities for each of the amplitudes, we order them, first by resonance and then by their pseudovector and pseudoscalar variants.

E.2.1 N(1650) S_{11}

First, we write down the variables for the N(1650) S_{11} resonance, which has spin-1/2 and odd parity. For the pseudoscalar coupling we get the following expressions:

$$c_1 = m_\Lambda + m_\mathrm{R}\,, \quad c_1' = 1\,, \quad c_3 = 1\,,$$

all the others evaluate to zero.

Next, for the pseudovector case, these variables change to:

$$\begin{aligned}
c_1 &= m_\mathrm{R}(k_\mathrm{K}^2 + k_\mathrm{K}\cdot k_\Lambda) + m_\mathrm{N}(k_\mathrm{K}^2 - 2k_\mathrm{R}\cdot k_\mathrm{K})\,,\\
c_1' &= k_\mathrm{R}^2 - m_\Lambda m_\mathrm{R} - m_\mathrm{N} m_\mathrm{R} + m_\Lambda m_\mathrm{N}\,,\\
c_2 &= k_\mathrm{K}^2 - 2k_\mathrm{R}\cdot k_\mathrm{K}\,,\\
c_2' &= m_\mathrm{R} + m_\Lambda\,,\\
c_3 &= 0\,, \quad c_3' = -m_\mathrm{R} + m_\mathrm{N}\,,\\
c_4 &= 0\,, \quad c_4' = 1\,.
\end{aligned}$$

E.2.2 N(1710) P_{11}

The amplitude variables for the pseudoscalar case of the N(1710) P_{11} read:

$$c_1 = -m_\Lambda + m_\mathrm{R}\,, \quad c_1' = -1\,, \quad c_3 = 1\,,$$

all the others being zero. For the pseudovector case, these variables are related to the ones for N(1650) S_{11} by setting $m_\mathrm{R} \mapsto -m_\mathrm{R}$ and $M \mapsto -M$.

E.2.3 N(1720) P_{13}

Here we have only one choice for the Lagrangian, and the calculated variables are

$$
\begin{aligned}
c_1 &= (k_\mathrm{K}\cdot k_\pi)(m_\Lambda + m_\mathrm{R}) - \frac{2}{3}m_\Lambda k_\mathrm{R}\cdot k_\mathrm{K} + \frac{1}{3}k_\mathrm{K}^2(m_\mathrm{N} - m_\mathrm{R}) - \frac{2}{3}m_\mathrm{R}k_\mathrm{K}\cdot k_\Lambda \\
&\quad - \frac{2}{m_\mathrm{R}^2}(k_\mathrm{K}\cdot k_\mathrm{R})(k_\mathrm{R}\cdot k_\pi)(m_\Lambda + m_\mathrm{R}) - \frac{1}{3m_\mathrm{R}}k_\mathrm{K}^2(k_\mathrm{R}\cdot k_\pi) \\
&\quad + \frac{1}{3m_\mathrm{R}}(k_\mathrm{R}\cdot k_\mathrm{K})(k_\mathrm{R}^2 - m_\Lambda m_\mathrm{N} + m_\mathrm{R}m_\Lambda - m_\mathrm{R}m_\mathrm{N})\ , \\
c_1' &= k_\mathrm{K}\cdot k_\pi + \frac{k_\mathrm{R}^2}{3} - \frac{2}{3}k_\mathrm{R}\cdot k_\mathrm{K} + \frac{1}{3}(m_\Lambda m_\mathrm{N} + m_\mathrm{R}m_\mathrm{N} + m_\mathrm{R}m_\Lambda) - \frac{2}{3m_\mathrm{R}^2}(k_\mathrm{K}\cdot k_\mathrm{R})(k_\mathrm{R}\cdot k_\pi) \\
&\quad + \frac{1}{3m_\mathrm{R}}k_\mathrm{R}\cdot k_\mathrm{K}(m_\mathrm{R} - m_\mathrm{N}) - \frac{1}{3m_\mathrm{R}}k_\mathrm{R}\cdot k_\pi(m_\mathrm{R} + m_\Lambda)\ , \\
c_2 &= k_\mathrm{K}\cdot k_\pi - \frac{2}{3}k_\mathrm{R}\cdot k_\mathrm{K} - \frac{2}{3m_\mathrm{R}^2}(k_\mathrm{K}\cdot k_\mathrm{R})(k_\mathrm{R}\cdot k_\pi) + \frac{1}{3m_\mathrm{R}}k_\mathrm{R}\cdot k_\mathrm{K}(m_\mathrm{R} - m_\mathrm{N})\ , \\
c_2' &= \frac{1}{3}(m_\mathrm{N} + m_\mathrm{R}) - \frac{1}{3m_\mathrm{R}}k_\mathrm{R}\cdot k_\pi\ , \\
c_3 &= \frac{k_\mathrm{K}^2}{3} - \frac{1}{3m_\mathrm{R}}k_\mathrm{R}\cdot k_\mathrm{K}(m_\Lambda + m_\mathrm{R})\ , \\
c_3' &= \frac{1}{3}(m_\Lambda + m_\mathrm{R}) + \frac{1}{3m_\mathrm{R}}k_\mathrm{R}\cdot k_\mathrm{K}\ , \\
c_4 &= -\frac{1}{3m_\mathrm{R}}k_\mathrm{R}\cdot k_\mathrm{K}\ , \quad c_4' = \frac{1}{3}\ .
\end{aligned}
$$

E.3 Cross sections

Here, we briefly discuss the difference of the prefactors of the two equations for the differential cross section (4.8) and (E.5) in section 4.2. According to [17, 62], the differential cross section for the two-body-reaction in our case is given by

$$\frac{\mathrm{d}\sigma}{\mathrm{d}\Omega_\mathrm{K}} = \frac{1}{64\pi^2}\frac{|\boldsymbol{p}_\mathrm{K}|}{|\boldsymbol{p}_\pi|}\frac{|\mathcal{M}|^2}{s}\ , \tag{E.5}$$

whereas our result from section 4.2 is given by

$$\frac{\mathrm{d}\sigma}{\mathrm{d}\Omega_\mathrm{K}} = \frac{1}{16\pi^2}\frac{m_\mathrm{A}m_\mathrm{B}}{s}\frac{|\boldsymbol{p}_\mathrm{K}(\widetilde{E}_\mathrm{K})|}{|\boldsymbol{p}_\pi|}|\mathcal{M}(E_\mathrm{K} = \widetilde{E}_\mathrm{K})|^2\ . \tag{4.8}$$

As already mentioned in section 4.2, the difference in the prefactor stems from the different normalisations of the asymptotic states involved. Whereas in [62] these are the free solutions of the Dirac equation for the nucleon, and the free solutions of the Klein–Gordon equation for the meson, in our case the nucleon wave functions are given by the bound states in the nuclear potential (see also chapter 2).

Furthermore, these asymptotic states are calculated using the notation and normalisation of [63], where the free spinors u satisfy

$$\bar{u}(p,s)u(p,s) = 1 \ .$$

This is different to the normalisation used in [62], which is given by

$$\bar{u}(p,s)u(p,s) = 2m \ .$$

Similarly, the nucleon and hyperon bound state wave functions we use, are normalised in such a way that

$$\int\limits_{\mathbb{R}^3} \psi^\dagger(\boldsymbol{x})\psi(\boldsymbol{x})\,\mathrm{d}^3x = 1 \ .$$

Summing over all nucleons (hyperons) then gives the mass number A (B), which translates to factors of the (hyper)nucleus mass m_A (m_B) in the cross section formulae. Therefore, (4.8) is related to (E.5) by substituting the factors $m_{(\mathrm{A,B})}/E_{(\mathrm{A,B})}$ by $1/2E_{(\mathrm{A,B})}$ in (4.1).

Bibliography

[1] E. Rutherford, *The Scattering of α and β Particles by Matter and the Structure of the Atom*, Philos. Mag. **21**:669–688, Apr 1911.

[2] N. Bohr, *On the Constitution of Atoms and Molecules, Part I*, Philos. Mag. **26**:1–25, 1913.

[3] N. Bohr, *On the Constitution of Atoms and Molecules, Part II Systems Containing Only a Single Nucleus*, Philos. Mag. **26**:476–502, 1913.

[4] N. Bohr, *On the Constitution of Atoms and Molecules, Part III Systems containing several nuclei*, Philos. Mag. **26**:857–875, 1913.

[5] A. Sommerfeld, *Atombau und Spektrallinien*, Friedrich Vieweg und Sohn, Braunschweig, 1919.

[6] J. Chadwick, *Possible Existence of a Neutron*, Nature **129**:312–312, February 1932.

[7] H. Yukawa, *On the interaction of elementary particles*, Proc. Phys. Math. Soc. Jap. **17**:48–57, 1935.

[8] J. D. Walecka, *A theory of highly condensed matter*, Ann. Phys. **83**(2):491–529, Apr. 1974.

[9] B. D. Serot and J. D. Walecka, *The Relativistic Nuclear Many Body Problem*, Adv. Nucl. Phys. **16**:1–327, 1986.

[10] G. D. Rochester and C. C. Butler, *EVIDENCE FOR THE EXISTENCE OF NEW UNSTABLE ELEMENTARY PARTICLES*, Nature **160**:855–857, 1947.

[11] Y. Ne'eman, *Derivation of strong interactions from a gauge invariance*, Nucl. Phys. **26**(2):222–229, Aug. 1961.

[12] M. Gell-Mann, *Symmetries of Baryons and Mesons*, Phys. Rev. **125**(3):1067–1084, Feb. 1962.

[13] M. Gell-Mann, *A schematic model of baryons and mesons**, Physics Letters **8**(3):214–215, Feb. 1964.

[14] G. Zweig, *An SU_3 model for strong interaction symmetry and its breaking; Part I* (CERN-TH-401):24 p, Jan 1964.

[15] G. Zweig, *An SU_3 model for strong interaction symmetry and its breaking; Part II* (CERN-TH-412):80 p, Feb 1964.

[16] U. Mosel, *Fields, Symmetries, and Quarks*, Texts and monographs in physics, Springer, Berlin; New York, 2nd rev. and enl. ed. ed., 1999.

[17] C. Amsler, et al., *Review of Particle Physics*, Phys. Lett. B **667**(1-5):1–1340, Sep. 2008.

[18] J. Schaffner and I. N. Mishustin, *Hyperon-rich matter in neutron stars*, Phys. Rev. C **53**(3):1416–1429, Mar. 1996, `nucl-th/9506011`.

[19] T. Klähn, et al., *Constraints on the high-density nuclear equation of state from the phenomenology of compact stars and heavy-ion collisions*, Phys. Rev. C **74**(3):035802, 2006, `nucl-th/0602038`.

[20] J. M. Lattimer and M. Prakash, *Neutron star observations: Prognosis for equation of state constraints*, Phys. Rept. **442**(1-6):109–165, Apr. 2007, `astro-ph/0612440`.

[21] D. Blaschke, T. Klaehn, and F. Weber, *Constraints on the High-Density Nuclear Equation of State from Neutron Star Observables*, 0808.1279 Aug. 2008, `arXiv:0808.1279`.

[22] J. Schaffner-Bielich, *Hypernuclear physics for neutron stars*, Nucl. Phys. A **804**(1-4):309–321, May 2008, `arXiv:0801.3791`.

[23] F. Özel and D. Psaltis, *Reconstructing the Neutron-Star Equation of State from Astrophysical Measurements*, 0905.1959 May 2009, `arXiv:0905.1959`.

[24] D. Page, picture, 1997.

[25] J. Piekarewicz, *Nuclear Physics of Neutron Stars* Jan. 2009, `arXiv:0901.4475`.

[26] H. Schulze, A. Polls, A. Ramos, and I. Vidana, *Maximum mass of neutron stars*, Phys. Rev. C **73**(5):058801, May 2006.

[27] E. Witten, *Cosmic separation of phases*, Phys. Rev. D **30**(2):272–285, Jul. 1984.

[28] N. Yasutake, et al., *General relativistic compact stars with exotic matter*, in *PERSPECTIVE IN NUCLEAR PHYSICS: Proceedings of the 6th Japan-Italy Symposium on Heavy-Ion Physics*, vol. 1120, 146–150, AIP, Tokai (Japan), May 2009, `arXiv:0904.3203`.

[29] R. Mallick, S. K. Ghosh, and S. Raha, *Magnetic field inhibits the conversion of neutron stars to quark stars*, 0904.3393 Apr. 2009, arXiv:0904.3393.

[30] P. C. C. Freire, et al., *A Massive Neutron Star in the Globular Cluster M5*, Astrophys. J. **679**(2):1433–1442, 2008, arXiv:0712.3826.

[31] T. C. Chan, et al., *Could the compact remnant of SN 1987A be a quark star?*, Astrophys. J. **695**(1):732–746, 2009, arXiv:0902.0653.

[32] A. K. Wroblewski, *Hypernuclei (and strange particles): How it all began?*, Acta Phys. Polon. B **35**:901–927, 2004.

[33] A. Zenoni and P. Gianotti, *The physics of hypernuclei*, Europhysics News **33**(5):5 pages, 2002.

[34] J. Pochodzalla, *Future hypernuclear physics at MAMI-C and PANDA-GSI*, Nucl. Phys. A **754**:430–442, May 2005.

[35] H. Bandō, M. Sano, J. Žofka, and M. Wakai, *Production of hypernuclei in relativistic ion beams*, Nucl. Phys. A **501**(4):900–914, Oct. 1989.

[36] M. Wakai, H. Bandō, and M. Sano, *Hypernucleus formation in high-energy nuclear collisions*, Phys. Rev. C **38**(2):748–759, 1988.

[37] M. Wakai, *Energy dependence of hypernucleus production in high-energy nuclear collision*, Nucl. Phys. A **547**(1-2):89–93, Sep. 1992.

[38] T. Gaitanos, H. Lenske, and U. Mosel, *Fragment formation in proton induced reactions within a BUU transport model*, Phys. Lett. B **663**(3):197–201, May 2008, arXiv:0712.3292.

[39] T. Gaitanos, H. Lenske, and U. Mosel, *Formation of hypernuclei in high energy reactions within a covariant transport model*, 0904.2106 Apr. 2009, arXiv:0904.2106.

[40] S. Bianchin, et al., *The HypHI project: Hypernuclear spectroscopy with stable heavy ion beams and rare isotope beams at GSI and FAIR*, 0812.4148 Dec. 2008, arXiv:0812.4148.

[41] K. Itonaga, T. Motoba, O. Richter, and M. Sotona, *Hypernuclear and Λ-spin polarizations produced in the (pi^+, K^+) reaction*, Phys. Rev. C **49**(2):1045–1058, Feb. 1994.

[42] H. Hotchi, et al., *Spectroscopy of medium-heavy Λ hypernuclei via the (π^+, K^+) reaction*, Phys. Rev. C **64**(4):044302, Sep 2001.

[43] H. Bandō, T. Motoba, and J. Žofka, *Production, structure and decay of hypernuclei*, Int. J. Mod. Phys. A **5**(21):4021–4198, Nov. 1990.

[44] T. Motoba, H. Bandō, R. Wünsch, and J. Žofka, *Hypernuclear production by the (π^+,K^+) reaction*, Phys. Rev. C **38**(3):1322–1334, Sep 1988.

[45] H. Bandō, T. Motoba, M. Sotona, and J. Žofka, *Polarization of hypernuclei in the (π^+, K^+) reaction*, Phys. Rev. C **39**(2):587–594, Feb. 1989.

[46] P. H. Pile, et al., *Study of hypernuclei by associated production*, Phys. Rev. Lett. **66**(20):2585–2588, May 1991.

[47] S. Ajimura, et al., *The Λ hypernuclear spectroscopy with the SKS spectrometer at KEK 12 GeV PS*, Nucl. Phys. A **585**(1-2):173–182, Mar. 1995.

[48] M. May, et al., *First Observation of the $p_\Lambda \rightarrow s_\Lambda$ γ-Ray Transition in ${}_\Lambda{}^{13}C$*, Phys. Rev. Lett. **78**(23):4343–4346, Jun 1997.

[49] T. Hasegawa, et al., *Spectroscopic study of ${}^{10}_{\Lambda}B$, ${}^{12}_{\Lambda}C$, ${}^{28}_{\Lambda}Si$, ${}^{89}_{\Lambda}Y$, ${}^{139}_{\Lambda}La$, and ${}^{208}_{\Lambda}Pb$ by the (π^+,K^+) reaction*, Phys. Rev. C **53**(3):1210–1220, Mar. 1996.

[50] O. Hashimoto and H. Tamura, *Spectroscopy of Λ hypernuclei*, Progress in Particle and Nuclear Physics **57**(2):564–653, Oct. 2006.

[51] R. Shyam, *$pp \rightarrow pK^+\Lambda$ reaction in an effective Lagrangian model*, Phys. Rev. C **60**(5):055213, Oct 1999, `nucl-th/9901038`.

[52] R. Shyam, *Dynamics of strangeness production in the near threshold nucleon-nucleon collisions*, Matter and Materials **21**:15, 2004, `hep-ph/0406297`.

[53] R. Shyam, W. Cassing, and U. Mosel, *Exclusive pion production in proton-nucleus collisions and the relativistic two nucleon dynamics*, Nucl. Phys. A **586**(4):557–585, Apr. 1995.

[54] R. Shyam, H. Lenske, and U. Mosel, *Exclusive K^+ production in proton-nucleus collisions*, Phys. Rev. C **69**(6):065205, Jun 2004, `nucl-th/0308085`.

[55] R. Shyam, H. Lenske, and U. Mosel, *Hypernuclear production by the (γ, K^+) reaction within a relativistic model*, Phys. Rev. C **77**(5):052201–052206, May 2008, `arXiv:0710.4888`.

[56] S. A. Chin, *A relativistic many-body theory of high density matter*, Ann. Phys. **108**(2):301–367, Oct. 1977.

[57] H. Lenske and C. Fuchs, *Rearrangement in the density dependent relativistic field theory of nuclei*, Phys. Lett. B **345**(4):355–360, Feb. 1995.

[58] C. Fuchs, H. Lenske, and H. H. Wolter, *Density dependent hadron field theory*, Phys. Rev. C **52**(6):3043–3060, Dec 1995, `nucl-th/9507044`.

[59] C. M. Keil, F. Hofmann, and H. Lenske, *Density dependent hadron field theory for hypernuclei*, Phys. Rev. C **61**(6):064309, May 2000, `nucl-th/9911014`.

[60] Y. K. Gambhir, P. Ring, and A. Thimet, *Relativistic mean field theory for finite nuclei*, Ann. Phys. **198**(1):132–179, Feb. 1990.

[61] N. K. Glendenning, et al., *Relativistic mean-field calculations of* Λ *and* Σ *hypernuclei*, Phys. Rev. C **48**(2):889–895, Aug 1993, `nucl-th/9211012`.

[62] M. M. Peskin and D. V. Schroeder, *An Introduction to Quantum Field Theory*, Perseus Books Publishing, L.L.C., 1995.

[63] J. D. Bjorken and S. D. Drell, *Relativistic Quantum Fields*, vol. 2, McGraw-Hill, Inc., New York, 1965, german translation: Bibliograph. Inst. Mannheim 1967, 409 P.(B.i.-Hochschultaschenbuecher, Band 101).

[64] F. Hofmann, *Relativistische Feldtheorie für exotische Kerne und seltsame Kernmaterie*, Ph.D. thesis, University Giessen, 2000.

[65] C. Itzykson and J. B. Zuber, *Quantum field theory*, International series in pure and applied physics, McGraw-Hill International Book Co., New York, 1980.

[66] K. A. Brueckner, J. R. Buchler, S. Jorna, and R. J. Lombard, *Statistical Theory of Nuclei*, Phys. Rev. **171**(4):1188–1195, Jul. 1968.

[67] W. Peters, *Die kohärente Photoproduktion von Pionen und Eta-Mesonen an sphärischen Kernen in einem relativistischen, nicht-lokalem Modell*, Ph.D. thesis, University Giessen, 1998.

[68] I. Sick and J. S. McCarthy, *Elastic electron scattering from* ^{12}C *and* ^{16}O, Nucl. Phys. A **150**(3):631–654, Jul. 1970.

[69] W. Peters, H. Lenske, and U. Mosel, *Coherent photoproduction of pions on spin-zero nuclei in a relativistic, non-local model*, Nucl. Phys. A **640**(1):89–113, Sep. 1998, `nucl-th/9803009`.

[70] C. J. Joachain, *Quantum collision theory*, North-Holland Publishing Company, Amsterdam, 1975.

[71] M. Rufa, et al., *Multi-lambda hypernuclei and the equation of state of hypermatter*, Phys. Rev. C **42**(6):2469–2478, Dec 1990.

[72] R. E. Chrien, et al., *States of* $^{12}_{\Lambda}C$ *formed in the reaction* $^{12}C(K^-, \pi^-)$, Phys. Lett. B **89**(1):31–35, Dec. 1979.

[73] D. Davis, *Hypernuclei - the early days*, Nucl. Phys. A **547**(1-2):369c–378c, Sep. 1992.

[74] P. Dluzewski, et al., *On the binding energy of the ${}^{12}_{\Lambda}C$(g.s.) hypernucleus*, Nucl. Phys. A **484**(3-4):520–524.

[75] R. Shyam, H. Lenske, and U. Mosel, *A relativistic two-nucleon model for $A(p, K^+)_\Lambda B$ reaction*, Nucl. Phys. A **764**:313–337, 2006, `nucl-th/0505043`.

[76] R. Shyam, *Hyperon production in near-threshold nucleon-nucleon collisions*, Phys. Rev. C **73**(3):035211–6, Mar. 2006, `nucl-th/0512007`.

[77] D. M. Manley and E. M. Saleski, *Multichannel resonance parametrization of πN scattering amplitudes*, Phys. Rev. D **45**(11):4002–4033, Jun. 1992.

[78] T. Feuster and U. Mosel, *Electromagnetic couplings of nucleon resonances*, Nucl. Phys. A **612**(3-4):375–390, 1997, `nucl-th/9604026`.

[79] T. Feuster and U. Mosel, *Unitary model for meson-nucleon scattering*, Phys. Rev. C **58**(1):457–488, Jul 1998, `nucl-th/9708051`.

[80] G. Penner and U. Mosel, *Vector meson production and nucleon resonance analysis in a coupled-channel approach for energies $m_N < \sqrt{s} < 2$ GeV. I. Pion-induced results and hadronic parameters*, Phys. Rev. C **66**(5):055211, Nov. 2002, `nucl-th/0207066`.

[81] A. Gridnev and N. Kozlenko, *Pion-nucleon scattering in the K-matrix approach*, Eur. Phys. J. A **4**(2):187–194, Feb. 1999.

[82] T. Feuster and U. Mosel, *Photon- and meson-induced reactions on the nucleon*, Phys. Rev. C **59**(1):460–491, Jan 1999, `nucl-th/9803057`.

[83] C. Sauermann, B. L. Friman, and W. Nörenberg, *Resonance model for πN scattering and η-meson production in the S_{11} channel*, Phys. Lett. B **341**(3-4):261–267, Jan 1995, `nucl-th/9408012`.

[84] G. Penner, *Vector Meson Production and Nucleon Resonance Analysis in a Coupled Channel Approach*, Ph.D. thesis, University Giessen, 2002.

[85] W. Rarita and J. Schwinger, *On a Theory of Particles with Half-Integral Spin*, Phys. Rev. **60**(1):61, Jul 1941.

[86] L. M. Nath, B. Etemadi, and J. D. Kimel, *Uniqueness of the Interaction Involving Spin-3/2 Particles*, Phys. Rev. D **3**(9):2153–2161, May 1971.

[87] L. M. Nath and B. K. Bhattacharyya, *Photoproduction of pions at low energy*, Z. Phys. C **5**(1):9–15, Mar. 1980.

[88] V. Pascalutsa, *Quantization of an interacting spin-3/2 field and the Δ-isobar*, Phys. Rev. D **58**(9):096002, Sep 1998, `hep-ph/9802288`.

[89] V. Pascalutsa, *Correspondence of consistent and inconsistent spin-3/2 couplings via the equivalence theorem*, Phys. Lett. B **503**(1-2):85–90, Mar. 2001, hep-ph/0008026.

[90] C. Fronsdal, *Massless fields with integer spin*, Phys. Rev. D **18**(10):3624–3629, Nov. 1978.

[91] P. van Nieuwenhuizen, *Supergravity*, Phys. Rept. **68**(4):189–398, Feb. 1981.

[92] V. Pascalutsa and R. Timmermans, *Field theory of nucleon to higher-spin baryon transitions*, Phys. Rev. C **60**(4):042201, 1999, nucl-th/9905065.

[93] C. L. Korpa, *Complete spin structure of the pion-nucleon-loop delta self-energy*, Heavy Ion Phys. **5**:77–84, Mar. 1997, erratum-ibid. 5 (1997) 319–320, hep-ph/9703339.

[94] M. Post, *Hadronic Spectral Functions in Nuclear Matter*, Ph.D. thesis, University Giessen, 2003.

[95] M. Post, S. Leupold, and U. Mosel, *Hadronic spectral functions in nuclear matter*, Nucl. Phys. A **741**:81–148, Sep. 2004, nucl-th/0309085.

[96] W. Peters, et al., *The spectral function of the rho meson in nuclear matter*, Nucl. Phys. A **632**(1):109–127, Mar. 1998, nucl-th/9708004.

[97] E. L. Bratkovskaya, W. Cassing, M. Effenberger, and U. Mosel, *e^+e^- production from pp reactions at BEVALAC energies*, Nucl. Phys. A **653**(3):301–317, Jul. 1999, nucl-th/9903009.

[98] L. S. Kisslinger, *Scattering of Mesons by Light Nuclei*, Phys. Rev. **98**(3):761–765, May 1955.

[99] L. S. Kisslinger and F. Tabakin, *Pion-nucleus coordinate-space potential*, Phys. Rev. C **9**(1):188–199, Jan 1974.

[100] J. Nieves, E. Oset, and C. Garcia-Recio, *Many-body approach to low-energy pion-nucleus scattering*, Nucl. Phys. A **554**(4):554–579, Mar. 1993.

[101] H. Feshbach, *Unified theory of nuclear reactions*, Ann. Phys. **5**(4):357–390, Dec. 1958.

[102] H. Feshbach, *A unified theory of nuclear reactions. II*, Ann. Phys. **19**(2):287–313, Aug. 1962.

[103] T. Mizutani and D. S. Koltun, *Coupled channel theory of pion-deuteron reaction applied to threshold scattering*, Ann. Phys. **109**(1):1–40, Nov. 1977.

[104] G. E. Brown and W. Weise, *Pion scattering and isobars in nuclei*, Phys. Rept. **22**(6):279–337, Dec. 1975.

[105] J. Nieves, E. Oset, and C. Garcia-Recio, *A theoretical approach to pionic atoms and the problem of anomalies*, Nucl. Phys. A **554**(4):509–553, Mar. 1993.

[106] R. A. Eisenstein and G. A. Miller, *Pirk: A computer program to calculate the elastic scattering of pions from nuclei*, Comput. Phys. Commun. **8**(2):130–140, Sep. 1974.

[107] R. A. Eisenstein and G. A. Miller, *DWPI: A computer program to calculate the inelastic scattering of pions from nuclei*, Comput. Phys. Commun. **11**(1):95–112, Jan 1976.

[108] R. A. Eisenstein and F. Tabakin, *Pipit: A momentum space optical potential code for pions*, Comput. Phys. Commun. **12**(2):237–257, Nov 1976.

[109] M. Döring and E. Oset, *s-wave pion-nucleus optical potential*, Phys. Rev. C **77**(2):024602–25, Feb. 2008, `arXiv:0705.3027`.

[110] S. R. Cotanch and F. Tabakin, *Kaon-nucleus inelastic scattering*, Phys. Rev. C **15**(4):1379–1383, Apr 1977.

[111] M. Kohno, et al., *Semiclassical distorted-wave model analysis of the* (π^-, K^+) Σ *formation inclusive spectrum*, Phys. Rev. C **74**(6):064613, Dec 2006, `nucl-th/0611080`.

[112] M. Abramowitz and I. A. Stegun, *Handbook of mathematical functions, with formulas, graphs, and mathematical tables*, Dover Publications, New York, 1965, 1972.

[113] R. E. Chrien, et al., *Elastic and inelastic scattering of* K^+ *from* ^6Li *and* ^{12}C, Nucl. Phys. A **625**(1-2):251–260, Oct. 1997.

[114] R. Michael, et al., K^+ *elastic scattering from C and* ^6Li *at 715 MeV/c*, Phys. Lett. B **382**(1-2):29–34, Aug. 1996.

[115] D. Marlow, et al., *Kaon scattering from C and Ca at 800 MeV/c*, Phys. Rev. C **25**(5):2619–2637, May 1982.

[116] D. Marlow, et al., *Pion scattering from C and Ca at 800 MeV/c*, Phys. Rev. C **30**(5):1662–1670, Nov 1984.

[117] S. J. Wallace, *Eikonal Expansion.*, Phys. Rev. Lett. **27**(9):622–625, 1971.

[118] J.-F. Germond and C. Wilkin, *Coulomb corrections to elastic pion-nucleus scattering in the eikonal model*, Ann. Phys. **121**(1-2):285–317, Sep. 1979.

[119] M. H. Cha and Y. J. Kim, *First-order eikonal approximation for the elastic scattering of 800 MeV/c pions from ^{12}C and ^{40}Ca nuclei*, Phys. Rev. C **54**(1):429–431, Jul. 1996.

[120] G. Satchler, *Introduction to nuclear reactions*, Wiley, New York, 1980.

[121] G. Satchler, *Direct nuclear reactions*, Clarendon Press ;;Oxford University Press, Oxford ;New York, 1983.

[122] K. T. R. Davies, *Complex-plane methods for evaluating highly oscillatory integrals in nuclear physics. II*, Journal of Physics G: Nuclear Physics **14**(7):973–993, 1988.

[123] K. T. R. Davies, M. R. Strayer, and G. D. White, *Complex-plane methods for evaluating highly oscillatory integrals in nuclear physics. I*, Journal of Physics G: Nuclear Physics **14**(7):961–972, 1988.

[124] H. A. Bethe and E. E. Salpeter, *Quantum Mechanics of One- and Two-Electron Atoms*, New York: Academic Press, 1957.

[125] M. Galassi, et al., *GNU Scientific Library Reference Manual - Third Edition (v1.12)*, Network Theory Ltd., 3rd revised edition ed., Jan. 2009.

[126] T. Hahn, *Cuba–a library for multidimensional numerical integration*, Comput. Phys. Commun. **168**(2):78–95, Jun. 2005, `hep-ph/0404043`.

[127] W. Chiang, B. Saghai, F. Tabakin, and T. H. Lee, *Dynamical coupled-channel model of kaon-hyperon interactions*, Phys. Rev. C **69**(6):065208, Jun. 2004, `nucl-th/0404062`.

[128] A. deShalit and H. Feshbach, *Theoretical nuclear physics, Volume I: Nuclear structure*, J. Wiley and Sons, New York, 1974.

[129] F. Schwabl, *Quantenmechanik für Fortgeschrittene (QM II)*, Springer, Berlin, 1997.

[130] J. D. Walecka, *Theoretical Nuclear and Subnuclear Physics*, Imperial College Press ; World Scientific, London; Singapore; Hackensack, NJ, 2nd ed. ed., 2004.

List of Figures

List of Tables

Deutsche Zusammenfassung

Seit des experimentellen Nachweises des Atomkernes und seiner Bestandteile, den Neutronen und Protonen, lag das wissenschaftliche Interesse darin, den Zusammenhalt dieser im Kern zu verstehen. Dabei spielten vor allem die Untersuchung der Kerneigenschaften im allgemeinen und die von besonders ungewöhnlichen im besonderen eine Rolle. So wurden und werden vor allem die Extrembereiche der Nuklidkarte ausgelotet, um Rückschlüsse auf die Anwendbarkeit von Kernmodellen zu ziehen und deren Gültigkeit zu überprüfen. Zu diesen Bereichen gehören unter anderem Kerne abseits des Stabilitätstals, wie etwa besonders neutronen- oder protonenreiche Kerne, aber auch solche mit zusätzlichen Teilchen statt der Protonen oder Neutronen. Zu diesen gehören die sogenannten Hyperkerne, die Baryonen mit Seltsamkeit enthalten und deren Produktion in dieser Arbeit untersucht wird.

Wir beschäftigen uns mit pioneninduzierter Hyperkernproduktion, bei der dieser Produktionsprozeß durch ein einlaufendes π-Meson (Pion) ausgelöst wird, welches im weiteren Verlauf der Reaktion durch die Wechselwirkung mit den Nukleonen eine Resonanz anregt, deren Zerfall die untersuchten Teilchen, ein K-Meson (Kaon) und ein Λ-Baryon, erzeugt. Diese Teilchen sind weitere Bestandteile des Standardmodells der Teilchenphysik. Durch die Untersuchung der weiteren Zerfallsprodukte können im Experiment Rückschlüsse auf deren Erzeugung beziehungsweise die zwischenzeitliche Existenz eines gebundenen Λ-Kern Zustandes, den oben angesprochenen Hyperkern, gezogen werden.

Die Teilchen mit Seltsamkeit wurden durch ihre besonderen Eigenschaften entdeckt und dementsprechend benannt, weil sie sich nicht wie erwartet verhielten. Sie besaßen eine wesentlich längere Lebenszeit, als aufgrund ihrer Masse zu erwarten war. Diese ließ sich nur damit erklären, daß diese Teilchen eine Besonderheit besitzen, die einen schnelleren Zerfall verhindert und somit "Seltsamkeit" (auf Englisch *strangeness*) genannt wurde. Später wurde diese Eigenschaft durch die entsprechende Einordnung in das Quarkmodell im Rahmen der Quantenchromodynamik erklärt.

So ergeben sich für die Baryonen und Mesonen, die aus jeweils drei Quarks beziehungsweise einem Quark und einem Antiquark aufgebaut sind, Relationen, die sich in Form von Oktets darstellen lassen, der sogenannte "eight-fold way" [11–13]. Das Mesonenoktet ist in Bild 1.1 dargestellt, und das Baryonenoktet in Bild 1.2. Darin ist jeweils der Anteil des sogenannten strange-Quarks gegenüber der Hyperladung Y aufgetragen, welche sich aus den Quantenzahlen der Seltsamkeit S und der Baryonenzahl B gemäß $Y = S + B$ ergibt. Mit der elektrischen Ladung Q und der dritten Komponenten des Isotopenspins I_3 ergibt sich dafür alternativ $Y = 2(Q - I_3)$. Weiterführende Details über die gruppentheoretische Klassifizierung

der Baryonen und Mesonen sind zum Beispiel in [16, 17] zu finden.

Für unsere Arbeit relevant sind diejenigen Teilchen, die genau ein strange-Quark beinhalten. Bei den Mesonen sind das die Kaonen (K^+, K^-, K^0, $\overline{K}^0$), und bei den Baryonen die Σ-Teilchen (Σ^-, Σ^0, Σ^+) und das Λ-Teilchen. Diese Baryonen werden oftmals auch *Hyperonen* genannt, und sie besitzen die Hyperladung $Y = 0$, da für ihre Baryonenzahl $B = 1$ und für ihre Seltsamkeit, aus historischen Gründen, $S = -1$ gilt. Wir werden in dieser Arbeit nicht die angeregten Zustände dieser Baryonen und Mesonen betrachten, die die Anzahl dieser seltsamen Teilchen vergrößert.

Die Erzeugung von Teilchen mit Seltsamkeit, wie wir sie in dieser Arbeit beschreiben, hat unter anderem eine wichtige astrophysikalische Bedeutung. So bestimmt die Anzahl der vorhandenen Freiheitsgrade zum Beispiel den Radius von Neutronensternen. Dabei können eventuell im Inneren vorhandene Teilchen mit Seltsamkeit (unter anderem eben die oben erwähnten Hyperonen) diesen beeinflussen [18–22], ebenso wie das Vorhandensein von freien Quarks und Gluonen [27–29]. Die Beobachtung von Neutronensternen mit Radien, die von solchen Modellen vorhergesagt werden, aber durch andere Modelle nicht beschrieben werden können, kann somit einen Hinweis auf die mögliche Zusammensetzung von Neutronensternen im Inneren geben [30, 31]. Weiterhin lassen sich damit Rückschlüsse auf das Verhalten von Materie bei extremen Bedingungen wie hoher Dichte, starker Gravitation und hohen Temperaturen ziehen. Das Verständnis der Erzeugungsprozesse der einzelnen möglichen Bestandteile auf elementarer Ebene ist somit ein interessantes Forschungsgebiet.

Andere, verwandte, Arbeiten beschäftigen sich mit der Hyperkernproduktion in sekundären Reaktionen bei Experimenten mit schweren Ionen [35–37]. Bei diesen Prozessen streuen Teilchen aus der primären Reaktion an den, bis dahin, unbeteiligten Nukleonen, und können dadurch Hyperkerne erzeugen. Dies funktioniert dann durch die gleiche Reaktion, wie wir sie auch in dieser Arbeit betrachten. Diese Reaktionen, ausgelöst durch Schwerionenkollisionen, sind ebenfalls Gegenstand aktueller Forschungen, auf theoretischer Ebene zum Beispiel im Rahmen von semiklassischen Transportmodellen [38, 39], und auf experimenteller Seite durch die HypHI Kollaboration [40]. Die meisten theoretischen Beschreibungen der Hyperkernproduktion sind allerdings entweder semi-klassisch [38, 39], oder beschränken sich auf eine nichtrelativistische Behandlung der Bindungszustände des Kerns [41, 42]. Die vorliegende Arbeit zeichnet sich dadurch aus, daß diese Reaktionen vollständig relativistisch und quantenmechanisch zu beschrieben werden.

Ein wichtiger Teil bei der Berechnung von Pion-Kern Wechselwirkungen ist die Beschreibung der Zustände im Kern beziehungsweise Hyperkern selbst. Diesen widmeten wir uns in Kapitel 2, in dem wir zuerst die allgemeinen Zugänge beleuchteten. Diese bestehen hauptsächlich aus dem phänomenologischen Walecka Modell [8, 9] und der Dirac–Brueckner Theorie, die versucht, die Kerneigenschaften aus den elementaren Wechselwirkungen zu bestimmen. Eine detaillierte Beschreibung dieser wurde und wird, zum Beispiel, im Rahmen der sogenannten dichteabhängigen relativistischen Hadronenfeldtheorie untersucht [58]. Für unsere Zwecke ausreichend ist ein vergleichsweise einfaches Modell, welches jedoch durch die erfolgreiche Beschrei-

bung der relevanten Kernparameter wie Radius und Ladungsverteilung gerechtfertigt ist. Die dazu benutzte Dirac-Gleichung enthält ein skalares und ein vektorielles Potential, welche die für uns interessanten Wechselwirkungen beschreiben. Als Differentialgleichung zweiter Ordnung für die Radialanteile der Wellenfunktionen lassen sich die Lösungen mit numerischen Algorithmen berechnen. Das Ergebnis sind die Kernwellenfunktionen im Ortsraum, $\psi(\boldsymbol{x})$, welche für unsere Rechnungen noch in den Impulsraum fouriertransformiert werden.

Das eigentliche Modell in dieser Arbeit beschreibt die Produktion von Teilchen mit Seltsamkeit durch die Erzeugung und den anschließenden Zerfall von Nukleonenresonanzen. Darauf gingen wir in Kapitel 3 näher ein. Diese elementare Reaktion des Pions findet dabei immer nur an einem Nukleon statt, was *Stoßnäherung* genannt wird. Sie ist immer dann gerechtfertigt ist, wenn die kinetische Energie der einlaufenden Teilchen, T_{lab}, groß gegenüber die Fermienergie ε_{F} der Nukleonen ist, $T_{\mathrm{lab}} \gg \varepsilon_{\mathrm{F}}$. In diesem Fall wird die Reaktion am Kern durch Einteilchenstöße dominiert. Da die Anfangs- und Endzustandswechselwirkungen einen Einfluß auf den Wirkungsquerschnitt haben können, müssen diese unter Umständen berücksichtigt werden. Wie dies im Rahmen der Stoßnäherung gehandhabt werden kann, wurde in Abschnitt 3.1 dargelegt. Die Details über die in dieser Arbeit verwendeten Resonanzen sind in Abschnitt 3.2 zu finden. Weiterhin werden für unsere Rechnungen Wechselwirkungslagrangedichten benötigt, die unter Berücksichtigung von Spin und Drehimpuls die richtigen Kopplungen an das Pion und Nukleon auf der einen Seite und das Kaon und Λ auf der anderen Seite beinhalten. So gibt es für die Spin-1/2 Resonanzen im wesentlichen die Möglichkeiten einer pseudoskalaren oder einer pseudovektoriellen Kopplung beziehungsweise einer Mischung aus beiden. Da eine beliebige Mischung mehr Parameter bedeuten würde, haben wir uns anhand [79, 82] auf die pseudoskalare Kopplung für Resonanzen mit ungerader Parität und die pseudovektorielle Kopplung für Resonanzen mit gerader Parität festgelegt. Zusätzlich betrachteten wir die entsprechenden Propagatoren und die Breiten der Resonanzen, die darin auftauchen, in Abschnitt 3.4.

In Kapitel 4 rekapitulierten wir die allgemeinen Aspekte der Beschreibung von Reaktionen anhand [62, 63, 70]. Wir präsentierten die kinematischen Details und die Besonderheiten in unserem Fall in Abschnitt 4.1. Eine kurze Herleitung der Gleichung für den (differentiellen) Wirkungsquerschnitt für den in dieser Arbeit betrachteten Prozeß haben wir in Abschnitt 4.2 gegeben. Zuletzt betrachteten wir in jenem Kapitel die Berechnung des Matrixelements selbst, welches die dynamischen Eigenschaften der Reaktion beschreibt. Dieses funktioniert durch die Anwendung der Feynmanregeln welche sich aus den Lagrangedichten ergeben. Zudem berücksichtigten wir die verschiedenen Näherungen für die Anfangs- und Endzustandswechselwirkungen auf die dafür zu lösenden Integrale.

Anschließend betrachteten wir die Wechselwirkungen der ein- und auslaufenden Mesonen. Diese werden im einfachsten Fall vernachlässigt, das heißt, die Mesonen werden durch ebene Wellen beschrieben. Der Sinn des Kapitels 5 bestand jedoch darin, die verschiedenen Möglichkeiten der Beschreibung dieser Wechselwirkungen und eventueller Näherungen auszuführen. So haben wir dort die Einzelheiten

des optischen Potentials (siehe Abschnitt 5.2) und dessen Berechnung geschildert. Weiterhin haben wir darauf aufmerksam gemacht, daß die Parametrisierung dieses Potentials vom Impuls beziehungsweise von der Energie des betrachteten Teilchens abhängig ist. Allen Ansätzen gemein ist jedoch, daß die Einführung eines zusätzlichen Potentialterms die Klein–Gordon Gleichung modifiziert. Die daraus berechneten Lösungen sind die von uns gesuchten Wellenfunktionen der Mesonen im Medium. Für einige ausgewählte Energien haben wir damit den elastischen Wirkungsquerschnitt für K^+ und π^+ an ^{12}C berechnet und mit experimentellen Daten verglichen. Dies erlaubte uns, sowohl die Parameter des optischen Potentials zu bestimmen und dessen Brauchbarkeit zu überprüfen.

Im Gegensatz zum relativ langsamen Kaon (im Vergleich zu seiner Ruhemasse), hat das Pion eine relativ hohe kinetische Energie (~ 1 GeV). Dadurch können für die Beschreibung seiner Wechselwirkungen weitere Näherungen vorgenommen werden. In unserem Fall betätigen wir uns der Eikonalnäherung, welche wir in Abschnitt 5.4 darlegten. Diese ist im wesentlichen eine Modifizierung der ebenen Welle durch ein geradliniges Integral über das optische Potential. Für diese Abänderung der freien Lösung benutzen wir eine weitere Näherung, bei der das optische Potential durch die elastische Streuamplitude und die Kerndichte gegeben ist. Diese sogenannte $t\varrho$-Näherung ist für Pionen in dem Energiebereich, den wir betrachten, durchaus brauchbar, wie in jenem Abschnitt gezeigt wurde. Weiterhin haben wir dafür die Kerndichte parametrisiert um eine schnelle numerische Auswertung zu ermöglichen. Bei den zwei Parametrisierungen handelt es sich um eine modifizierte Gaußform für leichte Kerne und eine Woods–Saxon-Form für schwerere Kerne. Beide Parametersätze haben wir dabei an die in Kapitel 2 berechneten Kernwellenfunktionen, beziehungsweise an die daraus resultierenden Dichteverteilungen, angepaßt. Der Betrag der Pion-Wellenfunktion, welcher einer Einhüllenden oder Modulation der zugrundeliegenden ebenen Welle entspricht, ist in Bild 5.12 zu sehen. Dabei wird das Ausmaß der Wechselwirkungen sichtbar, welches in etwa dem Kernradius entspricht.

Der letzte Abschnitt in Kapitel 5 ist dann der Fouriertransformation gewidmet, weil wir die Wellenfunktionen für die Berechnung des Wirkungsquerschnitts im Impulsraum benötigen. Wir haben dort die Möglichkeiten aufgezeigt, wie man dabei die Partialwellenentwicklung ausnutzen kann. Als Beispiel sei dabei die Eikonalwellenfunktion im Impulsraum angeführt und welche in Bild 5.15 dargestellt ist. Deutlich zu sehen ist die Peak-Struktur am On-Shell Punkt, die im Gegensatz zum Fall ohne Wechselwirkung eine endliche Breite besitzt.

Die letzten beiden Kapitel widmeten wir unseren Ergebnissen, indem wir unsere Rechnungen mit experimentellen Daten [42] verglichen. Als Targetkerne betrachteten wir dabei ^{12}C und ^{40}Ca, von denen allerdings nur für ^{12}C experimentelle Daten vorliegen. Beide Kerne haben die gleiche (gerade) Anzahl von Protonen und Neutronen, und sind kugelsymmetrisch und isospin-symmetrisch. Somit sind unsere Ansätze für die Potentiale, die auf der Kugelsymmetrie des Kerns beruhen, gerechtfertigt. Bei den Ergebnissen legten wir zuerst in Kapitel 6 Wert auf die Rechnungen ohne zusätzliche Wechselwirkungen der Mesonen mit dem Kern. Dabei wiederum,

begannen wir mit der Reaktion von π^+ an ^{12}C und zeigten die Ergebnisse für den $np_{3/2} \to \Lambda s_{1/2}$ Übergang. Wir erreichten dabei eine recht gute Übereinstimmung bis auf einen Faktor $2 \ldots 3$, um den sich unsere Berechnungen von den experimentellen Daten noch unterscheiden. Eine weitere kleine Diskrepanz ergab sich jedoch auch bei der Beugungsstruktur, allerdings ist hier der im Experiment betrachtete Bereich des Streuwinkels zu klein, um eine endgültige Aussage darüber zu treffen. Beim zweiten betrachteten Übergang, $np_{3/2} \to \Lambda p_{3/2}$, ergibt sich ein ähnliches Bild, wobei die Daten mit unserem Modell ein bißchen besser beschrieben werden, was den Absolutwert des Wirkungsquerschnitts betrifft. Aber auch hier läßt sich keine Aussage treffen, ob wir die Beugungsstruktur richtig beschreiben.

In Abschnitt 6.2 widmeten wir uns der Reaktion an ^{40}Ca. Leider gibt es für diese Reaktionen keine experimentellen Daten mit denen wir vergleichen könnten. Außerdem sind die gebundenen Λ Zustände in $^{40}_{\Lambda}$Ca weniger genau definiert wie in $^{12}_{\Lambda}$C [43]. So betrachteten wir ausschließlich den $nd_{3/2} \to \Lambda s_{1/2}$ Übergang und für diesen wieder die Winkelverteilung und die Impulsabhängigkeit des differentiellen Wirkungsquerschnitts bei $p_{\text{lab}} = 1050$ MeV. Durch einen direkten Vergleich mit den Ergebnissen an ^{12}C konnten wir sehen, daß der Absolutbetrag für beide Kerne in Vorwärtsrichtung etwa gleich ist, und sich bei größeren Streuwinkeln um etwa zwei Größenordnungen unterscheidet, wobei derjenige an ^{12}C der größere ist. Weiterhin haben wir die Abhängigkeit des differentiellen und totalen Wirkungsquerschnitts vom Eingangsimpuls des Pions im Laborsystem untersucht. Hier zeigt ein direkter Vergleich mit den Ergebnissen an Kohlenstoff, daß sich das Maximum des totalen Wirkungsquerschnitts minimal zu kleineren Impulsen verschiebt.

Das letzte Kapitel beschäftigte sich mit den Ergebnissen wenn wir für das Pion die Anfangszustandswechselwirkungen in der Eikonalnäherung mit einbeziehen. Aufgrund des damit verbundenen höheren numerischen Aufwandes haben wir uns auf die π^+-^{12}C Reaktion beschränkt, und dabei speziell auf den $np_{3/2} \to \Lambda s_{1/2}$ Übergang. Im direkten Vergleich mit den Ergebnissen im Fall der ebenen Wellen für das Pion zeigte sich, daß der Wirkungsquerschnitt sich in Vorwärtsrichtung minimal verkleinert, um dann zu größeren Streuwinkeln hin deutlich über dem für das nicht-wechselwirkende Pion zu liegen. Außerdem tritt die Beugungsstruktur weniger ausgeprägt hervor.

Aufgrund des numerischen Aufwandes wurden die Rechnungen bei denen die Endzustandswechselwirkungen der Kaonen betrachtet werden, auf künftige Arbeiten verlegt. Auch bleibt zu überprüfen, ob andere Arten von Austauschdiagrammen, wie etwa t- oder u-Kanal Versionen des vorliegenden Prozesses (im Vergleich zum s-Kanal in Bild 3.5) weitere wesentliche Beiträge zum Wirkungsquerschnitt liefern. Diese könnten dann unter Umständen den Absolutwert desselben beziehungsweise dessen Beugungsstruktur verbessern.

Danksagung

An dieser Stelle möchte ich mich bei allen bedanken, die zum Gelingen der Arbeit beigetragen haben. Somit gilt mein Dank Prof. Dr. Horst Lenske und Prof. Dr. Ulrich Mosel für die Aufnahme im Graduiertenkolleg und für die Aufgabenstellung die dieser Arbeit zugrundeliegt. Beide zeichnen sich auch für Anregungen und Diskussionen verantwortlich, die in diese Arbeit eingeflossen sind.

Ebenso bedanken möchte ich mich bei Prof. Dr. Radhey Shyam, dessen Programm der Ausgangspunkt für meine Arbeit war und dessen Gastfreundschaft mir zwei erlebnisreiche Monate in Kolkata ermöglichte. Die dabei entstandenen Diskussionen und Erklärungen haben mir stets weitergeholfen und bilden somit einen wesentlichen Bestandteil meiner Arbeit. Weiterhin hatte auch seine Frau einen großen Anteil an diesem erfolgreichen Aufenthalt in Indien, sowie die Sekretärin des Saha Institute of Nuclear Physics, die zusammen für einen für mich wissenschaftlich und kulturell erfolgreichen Besuch des Instituts sorgten.

Für weitere Beiträge und Diskussionen danke ich PD Dr. Stefan Leupold, mit dessen Hilfe ich einige Fragen klären konnte. Desweiteren bedanke ich mich bei meinen Mitstreitern Abdul Ataie, Andreas Fedoseew, Patrick Konrad, Tina Leitner für das angenehme Arbeitsklima und die eine oder andere gemütliche Kaffeepause samt Diskussion. Weiterhin danke ich Oliver Buß für das Probelesen der Arbeit und die zahlreichen Kommentare und Hinweise, die dieser Arbeit zu einem ansprechenden textlichen Stil verhalfen.

Spezieller Dank gilt auch unseren Institutsadmins Fabian Eichstädt und Janus Weil, die sich mit Hingabe um die rechentechnische Ausrüstung sowie die Behebung von Hard- und Softwareausfällen kümmerten, und somit dem numerischen Teil dieser Arbeit auf die Sprünge halfen.

Nicht vergessen möchte ich unsere Institutssekretärinnen Elke Jung und Ilka Sproates, die für einen angemessenen administrativen Rahmen sorgten, ohne den ich diese Arbeit nicht hätte schreiben können.

Mein weiterer Dank gilt den Sportfreundinnen und -freunden vom Athletenclub Suhl und TV08 Aßlar, bei denen ich regelmäßig für körperlichen Ausgleich zur geistigen Arbeit sorgen konnte.

Ganz besonders danken möchte ich meinen Eltern und meiner Familie, die mich während meines langen Studiums immer unterstützten und es mir so ermöglichten, meine Ziele zu verwirklichen.